Title
Carrier Transport in Hybrid Organic-Inorganic Thermoelectric Materials

Author
Zaia, Edmond W

Publication Date
2019

Peer reviewed|Thesis/dissertation

Carrier Transport in Hybrid Organic-Inorganic Thermoelectric Materials

By

Edmond W Zaia

A dissertation submitted in partial satisfaction of the
requirements for the degree of
Doctor of Philosophy

in

Chemical Engineering

in the

Graduate Division

of the

University of California, Berkeley

Committee in Charge:

Dr. Jeffrey J. Urban, Co-Chair
Professor Bryan D. McCloskey, Co-Chair
Professor Nitash P. Balsara
Professor Roya Maboudian
Professor Andrew Minor

Summer 2019

Abstract

Carrier Transport in Hybrid Organic-Inorganic Thermoelectric Materials

By

Edmond W Zaia

Doctor of Philosophy in Chemical Engineering

University of California, Berkeley

Dr. Jeffrey J. Urban, Co-Chair
Professor Bryan D. McCloskey, Co-Chair

Thermoelectric devices have the unique ability to interconvert heat and electricity directly. Soft thermoelectric materials, including conjugated polymers and organic-inorganic hybrids, now demonstrate figures of merit approaching those of inorganic materials. These breakthroughs in materials development enable the design of thermoelectric devices that exhibit appropriate efficiencies for commercial use, while simultaneously leveraging the unique processing and mechanical advantages of soft materials. Such technology opens the door to a suite of new thermoelectric applications, including power generation for biomedical implants and the Internet of Things, or wearable heating and cooling devices. However, in order to realize deployment of such technologies, there is a fundamental need for deeper understanding of the complex transport physics underlying thermoelectric transport in soft materials.

The central focus of this dissertation is investigating the fundamental physical phenomena critical to carrier transport in hybrid organic-inorganic thermoelectric material. Due to the complex nature of this class of multiphase material, there remains a problematic lack of consensus in the field regarding transport in hybrid materials. The mechanisms of carrier transport, key physics responsible for high thermoelectric performance, and even how to model transport in these materials are all subjects of debate within the field. Here, I describe the design, synthesis, and characterization of a prototypical PEDOT:PSS-Te hybrid nanomaterial with the goal of performing careful study of the carrier physics and relevant molecular-scale phenomena in this material. A novel technique for patterning alloy nanophases is demonstrated, resulting in well-controlled PEDOT:PSS-Te-$Cu_{1.75}Te$ heterowires. The Te-$Cu_{1.75}Te$ energetics are well aligned to leverage the carrier filtering effects proposed in literature. Using a full suite of experimental, theoretical, and modeling tools, we reveal the key physics responsible for dictating carrier transport and thermoelectric properties in this material, testing each of the major hypothesis in the field. Contrary to popular belief in the field, it is revealed that energy filtering does not play a major role in the carrier transport and high thermoelectric performance of these materials; rather, organic structural

effects at the hard-soft interface and interfacial charge transport emerge as the key phenomena underlying transport.

In a complementary study, I describe a platform approach for the synthesis of new solution-based, air stable *n*-type soft thermoelectrics. Using this approach, a composite perylene diimide-Te nanowire thermoelectric ink is prepared, demonstrating up to 20-fold enhancement over the individual components. The performance of these materials is competitive with the best-in-class for fully solution-processed, air stable *n*-type thermoelectric inks. We find experimental evidence linking reorganization of the perylene diimide molecules on the Te surface to enhanced electrical conductivity in the composite, further emphasizing the importance of structural effects in the organic phase to the overall thermoelectric properties of hybrid materials. Finally, leveraging the best materials from among the work in this dissertation, we demonstrate power generation in an all-ink flexible thermoelectric module with an innovative folded geometry.

The findings in this dissertation provide critical insight into the physics underlying carrier transport and high thermoelectric performance in hybrid organic-inorganic nanomaterials. This work highlights the importance of developing hybrid design strategies capable of leveraging molecular-level effects at the hard-soft interface. In furthering the field's fundamental understanding of this material class, we drive progress towards the realization of flexible thermoelectric modules compatible with applications such as implantable medical devices, wearable technologies, and the Internet of Things.

Table of Contents

List of Figures

List of Tables

Acknowledgements

Graduate school was a challenging and rewarding experience. I consider myself very lucky to have had been able to interact with many incredible scientists and friends, and I would like to take a moment to thank them for their role in this dissertation.

I would first like to thank my advisors, Jeff Urban and Bryan McCloskey, for the support and guidance they provided during my graduate career. Jeff's enthusiasm and readiness to act made him an incredible ally in the pursuit of my graduate science. Additionally, working with the Urban group inserted me into an expansive and collaborative network of brilliant scientists, without which I could not have accomplished the work to follow. Bryan has consistently provided me with patient and thoughtful mentorship through the years, for which I am very grateful.

I am deeply grateful to all the students and post-docs I've worked with through the Molecular Foundry and UC Berkeley communities. In particular, I want to thank Ayash Sahu for helping me find my feet as a researcher new to graduate school and acting as both a mentor and role model. I'd like to thank Maddie Gordon for great ideas, brainstorming, troubleshooting, and keeping lab entertaining for many years. Thanks to the thermoelectrics folks Jason Forster, Boris Russ, Nelson Coates, Jaeyoo Choi, Pengyu Yuan, Peter Yang, Heng Wang, and Woochul Lee for their expertise, collaboration, and friendship. The rest of the Urban Group, including Chih-Hao Hsu, Erin Creel, Fen Qiu, Sohee Jeong, Zhuolei Zhang, and Eun Seon Cho helped create a supportive and hardworking space for good science.

I owe a big thanks to the Molecular Foundry staff, in particular Tracy Mattox, Alyssa Brand, Anne Pham, Suksham Barun, and David Hohm for keeping the incredible facilities in such great shape and logistics running smoothly. Thanks to Carlet Altamirano for making sure everything on the campus side was in proper order, and for her incredible help managing things when they went wrong.

I'm also grateful to all my collaborators for providing critical insight, helpful conversation, and high-quality science: Kedar Hippalgaonkar, Pawan Kumar, Erol Yildirim, and Ruchira Chatterjee

I also want to thank the Chemical Engineering cohort of 2014, especially Marc Martin Casas, Lisa Burdette, Kyle Diederichson, Jaime Lincoff, Pete Dudenas, and Monica Neugebaur, for helping me get through coursework and making grad school a lot more fun.

Finally, a very special thank you to my husband, Grant Graziani, for just so many things over the past 5 years that I can't put them into words here. Suffice it to say that the richness of my life during this time period was immensely impacted by his influence in my life. Additionally, to my sisters, Shara and Shana, and my parents, Abby and William, I am deeply grateful for your continued energy and unerring support in my life.

Chapter 1. Introduction

1.1 Introduction to Soft Thermoelectric Materials

Traditional thermoelectrics applications have been dominated by doped inorganic semiconductors and their attendant solid-state processing methods, restricting accessible geometries and form factors.[1–4] Propelled by the recent development of new classes of soft materials with good thermoelectric properties, including organic semiconductors, polymers, and organic-inorganic composites, there has been a surge of interest in soft thermoelectrics (STEs).[5–7] STEs, including organic and organic-inorganic composite thermoelectrics, can realize flexible and lightweight energy generation or heating-cooling devices with conformal geometries, opening up a suite of new applications for thermoelectric devices.[8–10] Moreover, STEs are uniquely positioned within thermoelectric technologies to leverage inexpensive and scalable solution-based processing techniques (roll-to-roll, inkjet, etc.).[11–15] Utilizing existing printing infrastructure, it is possible to fabricate lightweight, flexible next-generation thermoelectric devices with diverse geometries. This is a particularly exciting area of research due to the global proliferation of low-power electronics, including personal or wearable devices, for which STE technology is well suited.[16–18] Basic operational aspects of thermoelectric and soft thermoelectric devices are illustrated in Figure 1.1.

However intriguing, these emerging classes of STE materials pose a new set of research challenges – relative to inorganic semiconductors, little is known about even very elementary structure-function relationships. In order to capitalize on the advantages promised by STEs, there is a fundamental need for further investigation and understanding of the complex carrier physics and unique material properties present in STE systems. Historically, for room temperature or near-ambient applications, the industry standard thermoelectric material has long been Bi_2Te_3.[2] In the past decade, driven by rapid progress in the field of organic semiconductors, STEs have made large strides in catching up with their inorganic counterparts in terms of thermoelectric performance, particularly for these low-temperature applications.[19–21] Nonetheless, as this research field is relatively young, STE-based thermoelectric devices have not yet realized commercial deployment. Since near-ambient applications are associated with challenging material property requirements, the research community has focused primarily thus far on materials development and optimization.[9,22] Demonstrations of soft thermoelectric energy generators (STEGs) are in the proof-of-principle phase, an area in which there is great opportunity for innovation.

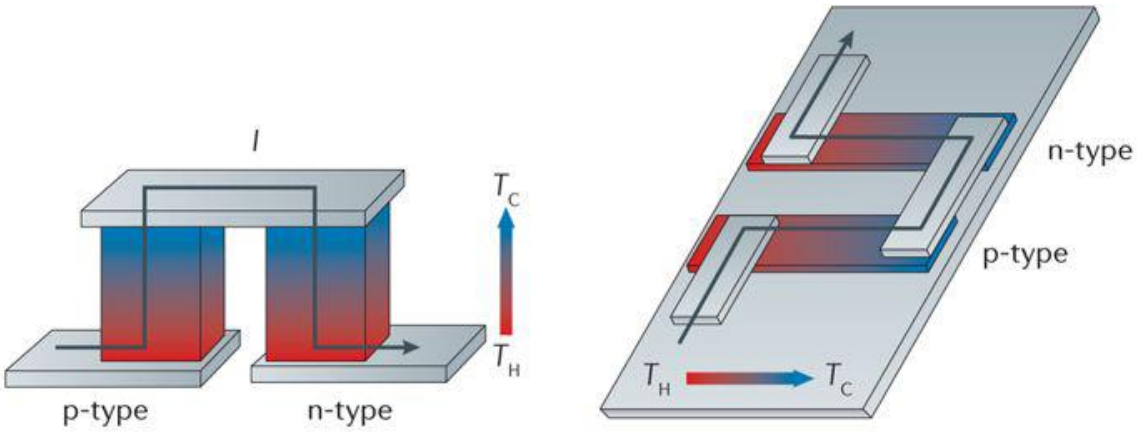

Figure 1.1 Basic operation of a thermoelectric generator (TEG) utilizes the Seebeck effect, in which the application of a thermal gradient induces the movement of carriers in a material and results in the creation of an electrical potential. By connecting *p*-type and *n*-type legs electrically in series and thermally in parallel, an electrical current (represented by the black arrows) can be sourced. Traditional inorganic TEGs (left) typically comprise rigid, pillar-like *pn* legs tiled over a ceramic substrate and require a thermal gradient incident perpendicular to the substrate. Alternatively, STEs (right) are typically patterned in 2D onto a flat substrate using low-cost, scalable printing techniques. For STEs, a thermal gradient can be applied parallel to the substrate, rendering optimization and understanding of in-plane carrier transport key for these materials.[5]

Realizing the full potential of STEs will require that researchers develop a more complete understanding of the energetics of organic molecular systems and how these translate into thermoelectric transport properties. This is not straightforward as the critical factors governing thermoelectric performance in organic systems are distinct from their inorganic counterparts. Even less well conceptually understood are vast numbers of hybrid organic-inorganic thermoelectrics that been developed in an attempt to harness the advantages of both hard and soft material classes. This is not a pejorative observation – many of the poorly understood aspects of hybrid materials are quite attractive as starting points for materials development. For instance, standard effective medium theory would predict that a simple composite of two phases would yield a material with thermoelectric properties intermediate between those of the starting components.[23] Hybrid materials, on the other hand, have been demonstrated to achieve performances exceeding that of either pure component.[24–26] There are a number of hypotheses regarding the physics underlying this remarkable phenomenon, but the structural and energetic complexity of these hybrid materials makes definitive conclusions challenging. Nevertheless, hybrid organic-inorganic thermoelectrics have become a rich area of investigation within STEs.[27–29]

1.2 Application Requirements for Soft Thermoelectrics

Due to their unique processing advantages, soft thermoelectrics enable a diverse new set of applications for thermoelectric devices. However, with new applications come new material requirements and challenges. One obvious challenge, seldom discussed, is material stability. While thermoelectrics require temperature gradients for operation, most organic-based soft thermoelectrics degrade upon prolonged exposure to temperatures above 200°C, restricting the use of this class of materials to low-temperature applications.[30] Often, for polymeric materials, doping

is predicated upon use of small molecules, which are also unstable with respect to temperature or oxygen. For example, property degradation has been observed in organic semiconductors after prolonged exposure to temperatures above 120°C.[31] However, this is far from problematic; mainly it just limits the scope of STE applications to areas where traditional thermoelectrics are non-competitive. For example, the suite of potential low-temperature applications for thermoelectric power generation or spot cooling has expanded dramatically as small-scale and personal electronic devices become increasingly ubiquitous. In particular, researchers have identified implantable medical devices, wearables for personal electronics, and Internet of Things as among the most promising near-term applications for power generation using STEs.[8,16,32] Material requirements for each application differ – implantable medical devices have strict demands for biocompatibility, power generation for personal electronics necessitates high thermoelectric efficiencies for practical utility, and Internet of Things applications are associated with highly variable thermal inputs. As a commonality, large-scale power generation is not required for any of these applications, but lightweight operation and compatibility with nonplanar substrates are paramount. For these applications, large power generation is not required, but lightweight operation and compatibility with nonplanar substrates are paramount. Thermoelectric cooling using flexible devices has also been identified as of great interest to personal comfort applications.[5,33] A common theme among these applications is that a TEG must be paired with devices varying widely in geometry and form factor. While this is not currently possible with commercial TEGs, STEGs represent a key technological advance, opening the door to a new suite of applications. Additionally, while STEGs can be prepared in a variety of ways, it is our view that a crucial element in the road to practical realization of flexible STEGs is the use of low-cost, solution-based processing techniques (including roll-to-roll, inkjet, dispenser, screen, and gravure printing) for both financial and technological reasons. These processes are compatible with existing modern infrastructure and equipment, making them practically appealing from an industrial perspective.

Implantable medical devices, including biological sensors or actuators, have frequently been identified as the nearest-term potential application for STEs, in particular since the power source for such devices can be the body of the user itself.[32,34,35] Life-saving medical implants such as pacemakers or defibrillators require a continuous source of low-grade power. The four key specifications for this class of applications are 1) provide sufficient power for the relevant duty cycle, 2) maintain the required power output without fatigue, 3) reside in a form factor small enough for implantation, and 4) comprise only non-toxic materials.[35] The current best practice in this field is to use batteries to power such devices, the replacement of which can require frequent additional invasive surgical procedures, each of which presents an inherent risk to the patient. Thermoelectric devices provide a key advance here – energy harvesting from body heat obviates the need for external power sources and enables continuous operation. As long as the temperature gradient is maintained, TEGs will not fail to provide power, and further surgical procedures can be avoided. Precedent of such longevity has been well established by the successful implementation of thermoelectric power generation in unmanned space probes over decades of operation. For example, the Voyager probes, launched in 1977, have been powered by thermoelectric generators without any maintenance for over 40 years in their mission to study the outer solar system.[36] Additionally, transitioning towards carbon-based STEG devices greatly enhances the opportunity to create, flexible, bio-compatible devices that can be implanted or worn without risk or discomfort to the user.

To successfully power life-saving medical implants with STEGs, it has been suggested that at least 2°C thermal gradient must be maintained.[37] While wearable TEGs have been demonstrated to achieve up to 10°C ΔT, conservative reports suggest that a 5°C gradient can be maintained for an implanted device in certain locations, typically a few mm below the skin.[37,38] To evaluate the realistic potential for STEGs in this application, we can model the average human body as a 100W source of energy with an internal temperature of 37°C.[39] This energy can be considered a thermal flux through the surface area of the body (roughly 1.5 m^2). For a 5°C thermal gradient, a state-of-the-art STE material ($ZT \sim 1$) can theoretically harness around 20 $\mu W/cm^2$ from an average human body. To power a pacemaker, a power source of roughly 10 μW is required, corresponding to an STEG device with a surface are of ~1 cm^2, a reasonable size for an implanted device. We note that this analysis is a best-case-scenario – realistic device and systems concerns will increase the form factor of such a technology; however, the promise is considerable.

Translating this potential from theory to application involves additional technological challenges. For example, power levels as low as 1 μW may be sufficient for wireless biological sensors, well within the range that can be supplied by an STEG.[40] But in order to translate this energy into a wireless signal, the STEG must be able to supply this power at a minimum potential. Currently, state-of-the-art devices can convert signals ranging from 20-250 mV.[32,41] Assuming the use of STEGs where both the *p*- and *n*-leg materials have Seebeck coefficients with magnitude 100 μV/K, and a temperature gradient of 5°C, a suitable STEG would require between 20-250 p-/n- couples. More traditional converters require minimum potentials around 500 mV, corresponding to 500 couples, an increasingly impractical number of couples to fit into a small implanted device. The large number of couples required to operationalize this technology illustrates the device engineering challenges presented for practical utilization of STEGs in wireless sensors, independent of STE material optimization. The vast majority of work in this field has thus far focused on materials development, but this is not sufficient to surmount issues such as minimum operating potentials on the order of hundreds of milliwatts. With such constraints, the techniques used in materials synthesis and device fabrication become pivotal. Layer-by-layer deposition and solid-state processing techniques quickly become prohibitively expensive and time consuming. Alternatively, promising work has been done in leveraging the automation and scalability associated with solution-based printing to enable fabrication of devices with large numbers of couples. For example, Gordiz *et al.* demonstrate that printing TE legs in a hexagonally close-packed layout can be used to achieve high voltages and power densities (Figure 1.2).[15] Søndergaard *et al.* used roll-to-roll printing to fabricate an STEG with up to 18,000 serially connecting junctions (Figure 1.2).[14] These early results show that solution-based printing techniques have the potential to overcome the challenges of device design for new applications. While these are notable advances, practical device design and engineering remain critical open challenges for the field to address.

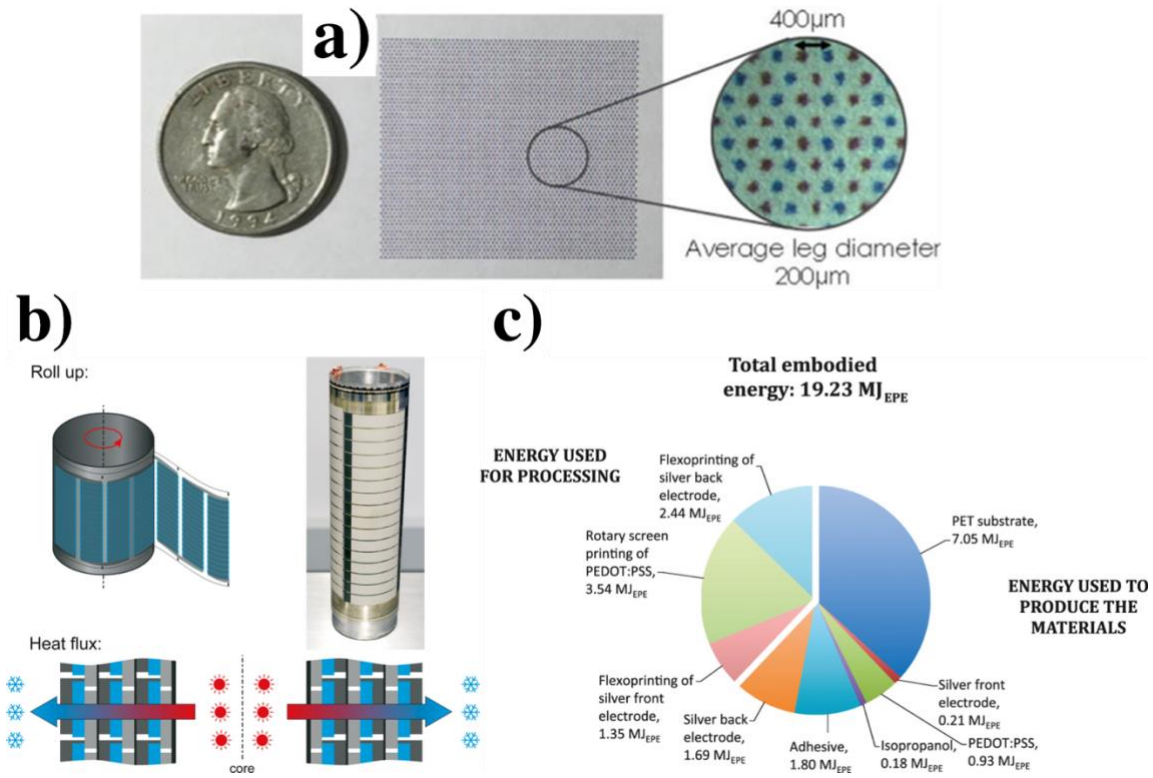

Figure 1.2 Solution-based printing techniques can be used to reliably pattern large numbers of thermoelectric legs with high scalability and low cost. a) Printing thermoelectric inks into a hexagonally close-packed pattern can achieve high voltages and power densities.[15] b) Roll-to-roll fabrication has been demonstrated to produce a conformal cylindrical STEG with 18,000 serially connected thermoelectric junctions.[14] c) The breakdown of energy consumption used to create this cylindrical STEG reveals relatively low processing costs, with the substrate consuming the majority of energy. Reproduced with permission.[14] Copyright 2013, Wiley-VCH.

Beyond implantable medical devices and biological sensors, the number of small, low-power electronic devices available for personal use has been rapidly accelerating. The term 'Internet of Things' (IoT) is being used to refer to this trend, in which everyday objects become interconnected and endowed with sensing, processing, communication, or energy management capabilities.[42,43] The balance of market forecasts predict that this trend will lead to the next boom in the semiconductor industry.[44] Specifically, the current phase has been identified as "early adoption" of IoT technologies. Trends suggest that massive adoption will be reached in the near future, with an unprecedented scale of trillions of connected devices in utilization globally possible as early as 2025.[42,45] Due to the astronomical number of sensor nodes implicated in this paradigm, it is crucial to eliminate reliance on any elements requiring frequent maintenance or replacement, especially batteries. In this challenge, thermoelectric devices present a unique opportunity. One proposed approach to IoT power generation is wireless power transfer.[46] Current state-of-the-art in this field involves the use of magnetically resonant coils.[47,48] Coupling via magnetic resonance is used to maximize energy transfer efficiency and minimize energy dissipated to extraneous non-resonant objects. However, efficiency is low, concerns regarding personal long-term exposure to EMF fields, and scalability of this approach render wireless power transfer increasingly impractical when considering the potential to realize trillions of IoT devices globally. By harvesting waste heat, TEGs can operate without fail or recharging, and they can adequately power small-scale

electronics. For this reason, thermoelectric technologies are being investigated as a main element in IoT power schemes.[16,19,43,44,49] The approach to IoT power generation can be divided into two portions based on power source – wearables, which seek to harness a user's body heat, and non-wearables, which seek to harness waste heat directly from the electronic devices.

Wearables have attracted considerable interest in the STE community, as body heat is an appealing and convenient source of energy that pairs well with personal electronics.[17,38] To date, there has already been a single instance of successful commercialization of a wearable TEG, the Matrix Powerwatch. This product is a smartwatch powered solely by a thermoelectric generator harnessing the user's body heat. Smartwatch technologies typically require power input on the order of 20-30 μW, which could reasonably be produced by an STEG with a surface area on the order of a few cm^2.[50] Beyond smartwatches, a wearable STEG can, in theory, supply sufficient power to operate a number of personal devices, including portable music players, wireless headphones, or wireless GPS units.[17] Again, from our previous analysis, such a technology could theoretically harness up to 20 $\mu W/cm^2$, or up to ~275 mW from a single human body. However, when considering the surface area available for an STEG, this number shrinks considerably. For reference, a smartphone requires roughly 1W for active operation and is thus a poor fit for wearable thermoelectric technology. While the field has thus far has primarily focused on materials development, there are a number of recent reports focusing more on module-level strategies for integration of STE into wearables.[30,51–54] This trend is suggestive of a transition towards addressing device and engineering concerns in the field of STEGs, which represent some of the most critical and unaddressed open questions in the field. Some of the key concerns are not unique to STE and include deterioration of thermoelectric properties or structural failure (delamination, cracking) during typical use of wearable products (bending, folding, etc.). Proper encapsulation is needed to avoid performance attrition and user exposure. The STEG module must experience a consistent thermal gradient to act as a reliable power source, and for this purpose must be able to dissipate unwanted heat – this points to another crucial overlooked materials area of soft heat exchangers. The majority of heat exchanger materials development has been done with hard inorganic materials in mind. In practice, for small gradients, this can be a crucial performance limiter. If an STEG is paired directly with an electronic device, such as in the case of a smartwatch, any resistive heat generated by operation of the device must be efficiently dissipated.

Non-wearable IoT applications are less well studied. STEG technologies are still attractive in this area, mostly because they enable a wide variety of form factors. Conformal thermoelectric devices can be prepared for curved or non-standard surfaces, unlike traditional TEGs. IoT seeks to turn ordinary objects of any shape or geometry into connected electronic devices, requiring the flexibility in form factors provided by STEGs. The primary challenge for these applications is the lack of a dependable and consistent heat source. In order for a TEG to supply power, it must be able to achieve a consistent output voltage as well as consistent power. But since the output voltage is directly correlated with the temperature gradient applied to the TEG, both the maximum power extracted from the TEG as well as the voltage supplied by the device can vary widely. In order to enable thermoelectric power generation for the IoT, creative new system designs must be developed. Initial work on this problem involves the use of dynamic impedance matching and arrays of thermoelectric modules.[18,44,55] Setting TEG modules in parallel has also been suggested to improve device lifetime, as the device will continue to operate even if one element fails.[14] These considerations add significantly to the form factor of such technologies, the implication of which

is that materials development targets will be impacted. While such studies tend to fall more into electrical engineering expertise, the authors believe it is important for even materials development research to be informed by the downstream systems challenges. In particular, the need for consistent input voltages in the 20-500mV range from a mixed TEG array renders it unlikely that many thermoelectric materials identified in the literature with reasonable power factors but Seebeck coefficients under 50 μV/K could practically be applied in such technologies.[56–59]

1.3 Outline and Summary of Core Dissertation Chapters

The goals of this dissertation are as follows:

1. To identify the fundamental physics behind unique carrier transport in hybrid thermoelectric materials
2. To assess the role of the major physical mechanisms proposed in the literature in a prototypical hybrid thermoelectric system
3. To use this knowledge to develop new, high performing *p*- and *n*-type soft thermoelectrics

In Chapter 2, I introduce the fundamentals of thermoelectric materials, with an emphasis on the relevant transport and physical properties. Here, the current understanding of the fundamental physics of carrier transport in hybrid materials is summarized.

In Chapter 3, the current state-of-the-art in soft thermoelectric materials is reviewed. This discussion includes the top performing *p*- and *n*-type soft material systems, as well as an examination of soft thermoelectric devices demonstrated to-date.

Chapter 4 details our original efforts to design, synthesize, and characterize a prototypical hybrid thermoelectric system. This system provides the base for the work of Chapter 5, in which we report the first systematic investigation of the physical mechanisms underlying enhanced carrier transport in hybrid materials.

In Chapter 6, we extend our understanding of carrier physics in soft materials to develop a novel, high performing *n*-type thermoelectric material platform. Careful structural and energetic characterization of this system reveals the importance of structure and ordering of the organic phase in the thermoelectric transport of hybrid materials.

The materials developed in this dissertation achieve some of the highest performance in solution-processable, air-stable soft thermoelectrics to date. We utilize these new *p*- and *n*-type soft materials to fabricate a fully solution-processed flexible thermoelectric device and demonstrate reasonable power generation. This work represents a step towards practical realization of flexible thermoelectric modules for a new host of applications, such as implantable medical devices, Internet of Things, and wearable technologies.

Chapter 2. Fundamentals of Thermoelectric Materials

Adapted from "Progress and Perspective: Soft Thermoelectric Materials for Wearable and Internet ‐ of ‐ Things Applications," EW Zaia, MP Gordon, P Yuan, JJ Urban, *Advanced Electronic Materials,* 2019, Early View (DOI: 10.1002/aelm.201800823) with permission of the authors. *Reproduced with permission of Advanced Electronic Materials*.

The performance of a thermoelectric material is commonly evaluated by the dimensionless figure of merit ZT. This figure of merit encompasses three material properties – the electrical conductivity σ, the Seebeck coefficient or thermopower S, and the thermal conductivity κ. To be precise, ZT can be written as:

$$ZT = \frac{S^2\sigma}{\kappa}T \qquad (2.1)$$

where T is the average temperature. The longstanding benchmark for long-lasting, high performing room temperature thermoelectric materials is Bi_2Te_3, with a ZT ~1.[2] Considerable effort in the field of thermoelectrics is devoted to developing materials with high ZT. In order to achieve this, the material should have high electrical conductivity and Seebeck coefficient but low thermal conductivity. Optimizing these three parameters is quite difficult since they are fundamentally coupled (Figure 2.1). In particular, this has proven a difficult challenge in organic and organic-inorganic composite systems. ZTs in these soft systems have traditionally lagged behind those of their inorganic counterparts. Since thermal conductivity tends to be low in organic semiconducting materials, the field has focused primarily on maximizing the quantity $S^2\sigma$, known as the power factor.[58,60,61]

However, developing strategies to maximize power factors or ZT is nontrivial. In inorganic crystals, structural and energetic periodicity allow for the development of simple transport models, the most widely used of which is the Boltzmann transport equation.[62] Such models provide experimentalists with critical tools for developing and optimizing next-generation thermoelectric materials. However, the structural complexity and heterogeneity present in organic systems presents a barrier to developing similar theoretical or predictive tools. While hopping or mobility edge models do exist for organic systems, their applicability has been restricted to certain property regimes. Organic material systems can exhibit conductivity ranging from insulating to nearly metallic and exhibit a universal but poorly understood $S \propto \sigma^{-1/4}$ empirical trend, suggesting a need for more versatile models. Recently, Kang and Snyder presented the first universal thermoelectric transport model for conducting polymers.[63] This is a significant step for the field, providing experimentalists with tools to understand and tune the role of critical parameters such as morphology and carrier concentration in dictating observed thermoelectric transport trends.[64] Nevertheless, there remain myriad mysteries surrounding carrier dynamics and transport in soft thermoelectrics, both conceptually and practically. In particular, the scattering parameter *s* takes on new meaning within this framework, wherein the classical solid-state description no longer applies. Notably, while nearly all semiconducting polymers exhibit s=3 behavior, the highest performing materials (PEDOT-based derivatives) alone demonstrate s=1 transport. That the highest performing organic polymer system also demonstrates fundamentally distinct transport behavior is an intriguing and unresolved mystery. Further subtleties exist here – the parameter *s*

and the transport coefficient, σ_{E0}, appear to be somehow linked, although the true physical manifestation of either of these parameters is not clear. Kang and Snyder suggest that discovery of more s=1 polymers may yield polymers with greater values of σ_{E0} and therefore higher performing organic thermoelectrics. Indeed, discovery of additional s=1 polymers is a critical step in understanding the physical basis of the model parameters, as well as what makes PEDOT distinct among semiconducting polymeric materials. While the work of Kang and Snyder represents a key breakthrough for the field, it also highlights the opportunities for further investigation in the field of STEs.

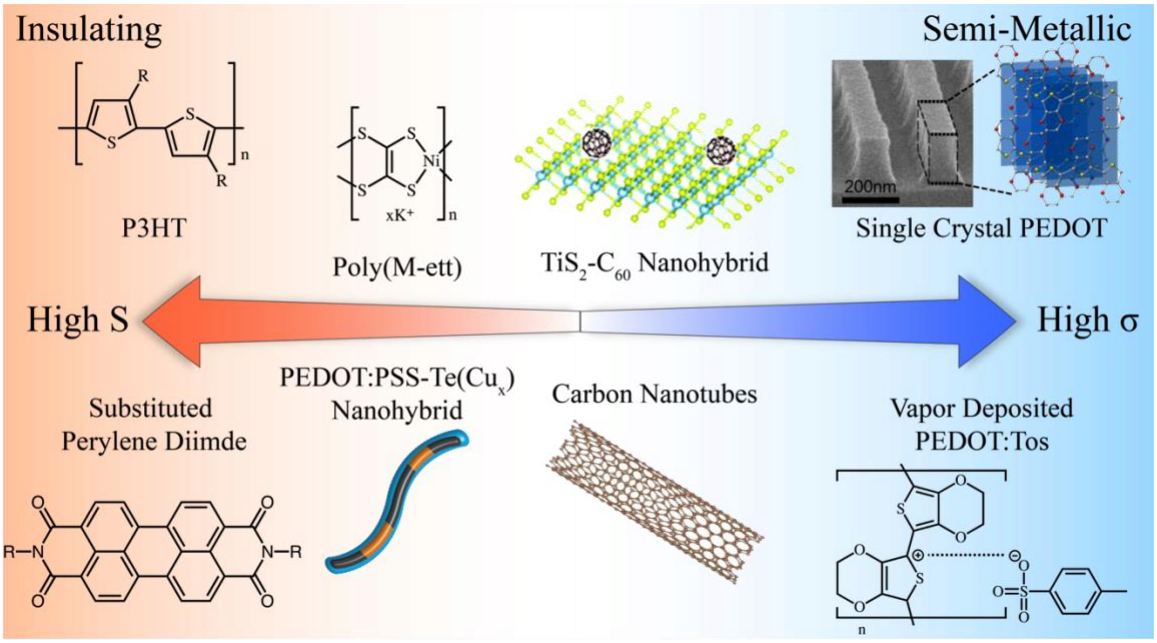

Figure 2.1 Soft materials exhibit a range of thermoelectric properties, from insulating to nearly metallic. High conductivity materials are characterized by high degrees of order and crystallinity, whereas lightly doped, polycrystalline materials demonstrate high Seebeck coefficients. Organic-inorganic hybrids potentially leverage the advantages of multiple materials, allowing for tunability of the thermoelectric properties.[19,25,52,57,65]

2.1 Electrical Conductivity

Electrical conductivity, σ, for a given material can broadly be described as

$$\sigma = ne\mu$$

where n is the charge carrier concentration, e is the elementary charge, and μ is the carrier mobility.

The microscopic details of conduction are, of course, treated differently in organic and inorganic systems. Central to this difference is structure. The strong directional bonding and beautiful translational symmetry inherent to pristine inorganic semiconductors leads to bands with a well-defined Fermi edge whose states primarily contribute to conduction. Alternatively, organic systems are often studied mostly as disordered or polycrystalline materials, featuring structural heterogeneity and weak intermolecular forces. The lack of long-range structural order in organic systems is a contributing factor to localized states falling below the mobility band edge, leading to trap states and hindered conduction.[63] On the other extreme, highly doped organic systems can

demonstrate conductivities rivaling that of metals, though this is difficult to achieve for all but a few systems in practice.[20,66]

The mobility of carriers in organic systems is strongly tied to intermolecular (or interchain for polymers) coupling and film crystallinity.[67–69] The main transport pathway in an organic system is typically along the conductive backbone of the molecule or polymer. However, bonding between molecules tends to be comprised of weaker interactions such as van der Waals bonding, resulting in large intermolecular/interchain energetic barriers.[70] Weak intermolecular interactions can also result in spatial and energetic disorder. The macroscale implication is that carriers can become trapped in localized states at domain boundaries due to the lack of long-range electronic coupling.[5,70] As such, it is observed that mobility is highly sensitive to energetic and structural disorder in organic systems. Because of this, transport in organic films is strongly dependent on processing conditions and filling of trap states and domain boundaries via doping. That is, doping an organic material can result in nonlinear increases in electrical conductivity due to a simultaneous mobility enhancement from trap state filling. In heavily doped organic systems, the opposite trend may be observed, as large carrier concentrations are associated with increased frequency of carrier scattering events, as well as distortion of the molecular scale packing. Needless to say, this broad range of phenomenology is challenging to capture in one transport model.

The charge carrier concentration is defined by the number of charges available to participate in transport. Unlike traditional inorganic semiconducting systems, electrons and holes are not always the predominant charge carrier species in organic systems. Polarons, a type of quasiparticle comprised of a charged species (electron/hole) coupled to a phonon, are often the dominant species of charge carrier in disordered organic systems.[70,71] Polarons, and bipolarons, result from addition or removal of electrons from an organic molecule's conjugated pi orbitals, which then leads to structural distortion in the backbone.[5] The existence of these quasiparticle excitations can cause a decrease in carrier mobility in the system due to the heavier effective mass and increased probability of polarons participating in self-trapping. Polaron formation can be monitored in organic systems via optical absorbance spectroscopy, as polaronic species give rise to unique absorptions distinct from pure electronic excitations. In both organic and inorganic materials, the mobility of carriers tends to decrease as a function of carrier concentration in the heavily doped regime due to an increased frequency of carrier scattering events.

Hybrid systems are complex, with both organic and inorganic transport domains. Conclusive understanding of underlying transport mechanisms and relative contributions of the organic/inorganic phases on the overall material transport remains an active area of investigation. Hybrids feature synergistic effects at the organic-inorganic interface, resulting in even more complex transport physics. At this interface, the discrete molecular orbitals of the organic phase interact directly with the continuum band states of the inorganic phase, resulting in interphase charge transfer and band bending.[72] While many groups have observed enhanced electrical conductivity in hybrid materials, there is still active debate regarding the fundamental physics underlying this enhancement.[24,25,51,73]

One effect that has been implicated in hybrid systems is interfacial charge transfer, or surface doping. Surface transfer doping implies that, at the inorganic-organic interface, some extent of

band bending occurs, causing charge accumulation at the interface. Because of this phenomenon, there is a local doping effect, wherein the carrier concentration is increased in either the organic or inorganic phase.[28] This form of doping reduces the impact of impurity scattering, providing greater carrier mobility at the interface and local regions of enhanced carrier concentration. Such a phenomenon necessitates proper matching of energetic states between the organic and inorganic molecules at the interface. The major point of contention here is related to the relative roles of the organic and inorganic phases. Some groups have suggested that the inorganic phase dominates conductivity in hybrid films.[26,74] More recently, several studies have implicated the organic phase as being the dominant phase in hybrid carrier transport.[73,75] These studies have suggested that the inorganic phase aids in reducing thermal conductivity by scattering phonons, or provides an interfacial doping effect to increase the local carrier concentration in the organic component at the organic-inorganic interface.

A second effect that has recently been implicated as a key factor in hybrid thermoelectric transport is physical templating of the organic phase on an inorganic surface.[73,75] In this effect, the surface of an inorganic nanoparticle acts as a template. Upon deposition of the organic component on this surface, the template encourages highly organized packing of the conductive organic molecule. Since the mobility of carriers in the organic phase is highly sensitive to the morphology and packing, such a templating effect can cause the formation of locally high mobility carrier transport pathways at the organic-inorganic surface.

Despite the progress described here, consensus over the relative importance of these two effects in hybrid systems has been elusive. Attempts at direct observation of these phenomena have met with little success, in particular due to the structural and energetic complexities of hybrid systems. Large AC conductivities, representing current driven by an oscillating electric field, have been observed in hybrid materials with relatively low DC conductivities. Because AC conductivities measurements are sensitive to carrier dynamics within localized domains, whereas DC conductivity measurements probe the aggregate thin film properties, this result is suggestive of critical differences between intra-domain and inter-domain transport within hybrid films.[76] At a fundamental level, the field still lacks a satisfying description of identity and role of dominant charge carriers in hybrid materials. Dense networks of bipolarons have been implicated in the formation of semimetallic states in highly conductive polymers, but this model is difficult to assess experimentally or extend into hybrid systems.[20] Further investigation of the interaction between free carriers and polarons/bipolarons, and the structural and energetic inhomogeneities present at the organic-inorganic interface will be key in furthering the field's understanding of conduction in hybrid materials.

2.2 Seebeck Coefficient / Thermopower

In addition to responding to a voltage bias, charge carriers can also be induced to migrate in a material by the application of a temperature gradient, an effect whose magnitude is characterized by the Seebeck coefficient, or thermopower. The Seebeck coefficient represents the open circuit voltage developed across a material per degree of thermal gradient applied. Physically, this phenomenon occurs as carriers on the hot side of the material will tend to diffuse towards the cold side, creating a gradient in carrier concentration. This gradient is also opposed by drift of carriers due to the internal electric field that develops as a consequence. Thus, the Seebeck coefficient has

a complex dependence on the carrier concentration and energetic landscape of a material. Generally, the Seebeck coefficient in organic materials can be described as

$$S = \frac{1}{\sigma}\left(\frac{k_B}{e}\right)\int\left(\frac{E - E_F}{k_B T}\right)\sigma_E\left(-\frac{\partial f}{\partial E}\right)dE$$

where σ is the electrical conductivity, k_B is the Boltzmann constant, e is the elementary charge, E_F is the Fermi energy, σ_E is the transport function, and *f* is the Fermi function. The form of $\sigma_E(E,T)$ depends on the mechanism of transport, and thus the temperature dependence of S also depends on the transport mechanism. The matter is further complicated by experimental measurements that do not fit with a single transport measurement. That is, $\sigma_E(E,T)$ sensitively depends on a complex mixture of the density of states (DOS), carrier velocity, and relaxation times, all of which have a nonlinear dependence on the energy of the carrier above the transport edge. In Kang and Snyder's recent work, a general form of $\sigma_E(E,T)$ is given:

$$\sigma_E(E,T) = \sigma_{E0}(T)\left(\frac{E - E_t}{k_B T}\right)^s$$

where $\sigma_{E0}(T)$ is a key parameter that arises from Kang and Snyder's work called the transport coefficient, E_t is the transport edge, and *s* is the scattering parameter. Note that $\sigma_E=0$ for all $E<E_t$.[63] One remarkable result from analysis is the emergence of the power law $S\alpha\sigma^{-1/4}$, a universal empirical relation that has previously eluded theoretical description.[64]

The position of the Fermi level within the DOS strongly affects the Seebeck coefficient in a material. By distorting the DOS via nanoconfinement in quantum well structures or band engineering researchers have sought to produce enhanced Seebeck coefficients.[77,78] Alternatively, moving the Fermi level via dedoping can be an effective technique for increasing the Seebeck coefficient, although it also leads to a simultaneous reduction of electrical conductivity. For example, the Seebeck coefficient in the polymer blend poly(3,4-ethylenedioxythiophene):poly(styrenesulfonate) (PEDOT:PSS) can be increased by using solvent treatments to dedope the system via removal of PSS.[51,79,80] Electrochemical dedoping has also been used to analogous effect; electrochemically oxidizing a PEDOT:PSS thin film was shown to tune the thermoelectric properties and achieve a maximum power factor of 25μW/mK^2.[81] Chemical oxidation has been shown to similarly tune the thermoelectric properties in poly(3,4-ethylenedioxythiophene):tosylate (PEDOT:Tos) films. Bubnova *et al*. used chemical oxidation to vary the carrier concentration in PEDOT:Tos from 15 to 40% oxidation, reaching a maximum ZT of 0.25.[19]

Another strategy for increasing the asymmetry of mobile carriers about the Fermi level is energy filtering. This approach seeks to scatter low-energy (cold) carriers without hindering transport of high-energy (hot) carriers. Typically, a moderately sized energetic barrier is introduced for this purpose. In theory, this method reduces the electrical conductivity since some cold carriers are no longer able to participate in conduction, but since ZT is quadratically dependent on S and linearly on σ, this is still a viable technique for enhancing the thermoelectric efficiency of a material. Energy filtering has been implicated in several reports of high thermoelectric performance, especially in hybrid material systems.[24–26] But since direct observation of energy filtering is an

experimental challenge, no study has been able to definitively demonstrate this phenomenon. In fact, several reports have suggested that the role of energy filtering has been overestimated in the thermoelectric literature.[75,82]

2.3 Thermal Conductivity

Thermal conductivity (κ) represents a material's ability to conduct heat. This parameter represents a unique challenge to the thermoelectric community. To achieve high thermoelectric performance, the thermal conductivity of a material must be minimized. This requirement typically conflicts with the need to achieve high electrical conductivities, as the two are often closely coupled and relate to some degree to bond strength and material order. Moreover, among the main three thermoelectric material properties, the accurate measurement of thermal conductivity is the most challenging due to the strong sensitivity of measurement techniques to parasitic heat conduction paths. Generally, the thermal conductivity can be thought of as a combination of thermal conduction via lattice vibration (phonons) and thermal transport via electrons. Significant improvements in the performance of traditional inorganic thermoelectric materials over the past couple decades have largely been the result of nanostructuring. The foundational principle of nanostructured thermoelectrics is to reduce the length-scale of materials to below the phonon mean free path, reducing the thermal conductivity via increased phonon scattering without impeding electronic transport.[1,83,84] Additional approaches include grain boundary engineering and introduction of mesostructure.[85,86] Theoretically, the thermal conductivity can be written as

$$\kappa = \frac{1}{3}\int C_\lambda(\lambda,T)\nu(\lambda)L(\lambda,T)d\lambda$$

where λ is the wavelength, C_λ is the specific heat per unit wavelength, ν is the group velocity, L is the spectra mean-free path, although this description applies more satisfactorily to inorganic than organic systems. According to this prediction, κ can be reduced either by reduction in the product $C_\lambda(\lambda,T)\nu(\lambda)$ through phonon confinement in nanomaterials and superlattices with extremely small dimensions, or by reducing $L(\lambda,T)$ through enhancement of phonon boundary and interface scattering. In order to optimize the thermal conductivity in a given material, theoretical approaches have been developed including molecular dynamics simulations,[87] first-principles calculations,[88] and machine learning, data-driven methods.[89,90] Experimental measurement of phonon transport is more challenging. The most common techniques to measure thermal conductivity include time-domain thermoreflectance (TDTR) and the 3ω-method.[91] Thermal conductivity measurements using Raman spectroscopy[92] and inelastic neutron scattering are also useful in certain instances.[93]

While TDTR and 3ω are the most commonly used techniques to measure thermal conductivity of thermoelectric thin films, both methods most easily measure the out-of-plane thermal conductivity. Since it's well known that STE materials can feature high degrees of anisotropy, greater emphasis must be placed on measurements of in-plane thermal conductivity, especially given that in-plane tends to be the relevant direction of transport for a device. For example, the thermal conductivity of PEDOT:PSS, a polymer blend that exhibits remarkably high thermoelectric performance, has been shown to possess considerable anisotropy in thin films, with the in-plane thermal conductivity up to three times greater than the out-of-plane value.[94] This finding suggests that, if only out-of-plane thermal conductivity is measured, then the reported material ZT may be off by large margin. Indeed, in organic materials, the thermal conductivity is often assumed to be low due to the

presence of organic components, but it is important to note that this is an assumption. Using suspended microdevices, the thermal conductivity of high conductivity PEDOT thin films has recently been reported to be greater than expected.[95] Despite the difficulties of obtaining reliable thermal conductivity measurements in the direction relevant to transport, it is nonetheless an important measurement for the accurate characterization of thermoelectric efficiency.[96]

Hybrid films provide an opportunity to reduce the thermal conductivity via inclusion of nanostructures to enhance phonon scattering. Wang *et al*. recently showed that a hybrid film of PEDOT deposited on top of a periodic superlattice of Bi_2Te_3 nanoparticles reduced the thermal conductivity from 1.52 W/mK (pure PEDOT) to below 0.6 W/mK with the inclusion of 50% Bi_2Te_3 nanoparticles.[73] Using an exfoliation-and-reassembly method, Tian *et al.* demonstrated that a flexible *n*-type TiS_2/hexylamine composite exhibited in-plane thermal conductivity as low as 0.37, which is an order of magnitude smaller than that of single-crystal TiS_2 (4.2 W/mK).[97] In another result, a high performing TiS_2/fullerene composite (ZT~0.3 at 400K) was measured to have thermal conductivity of 0.61-0.96 W/mK.[52] These studies illustrate that rational design of organic-inorganic composite thermoelectrics can provide significant advantage over single-component films.

2.4 Mechanical Properties

Beyond thermoelectric properties, STEGs capitalize on favorable mechanical properties of organic materials. To fabricate conformal geometries, the STEG must function properly under strain without cracking or delamination. Indeed, stress or strain on a thermoelectric module can have strong effects on the electrical and thermal transport properties, and thus the overall thermoelectric efficiency.[98,99] Hokazono *et al*. showed that a STEG made from PEDOT:PSS was able to undergo up to 10,000 repeated bending operations without significant reduction in thermoelectric properties.[30] Similarly, Dong *et al.* performed up to 6,000 bending test on a composite organic-inorganic STEG, which experience little to no loss in thermoelectric performance after up to 5,000 bending cycles.[9] While bending tests are important, it is important to perform additional stress tests for other failure modes, such as in-plane stretching and out-of-plane compression, although such experiments are infrequent as of yet.[100] Stability can also be a critical issue in organic systems due to the risk of photo-induced oxidation, and rigorous stability tests are often missing from STEG demonstration reports. Hokazono *et al*. showed that a pure PEDOT:PSS STEG experienced only 17% decrease in electrical conductivity after 3600 hours of heating to 353K in air.[30] However, stability requirements for commercial applications are stringent, and a given material's stability will be strongly influenced by molecular design and module architecture and thus warrants greater emphasis in the field.

Chapter 3. State-of-the-Art: Soft Thermoelectric Materials Development and Device Demonstration

Adapted from "Progress and Perspective: Soft Thermoelectric Materials for Wearable and Internet ‐ of ‐ Things Applications," EW Zaia, MP Gordon, P Yuan, JJ Urban, *Advanced Electronic Materials*, 2019, Early View (DOI: 10.1002/aelm.201800823) with permission of the authors. *Reproduced with permission of Advanced Electronic Materials*.

3.1 Organic Materials

In recent years, state-of-the-art in single component soft TE materials have rapidly caught up with their inorganic counterparts (Figure 3.1), at least for hole transporting materials. In particular, *p*-type polymers, driven by the emergence of highly conductive PEDOT, have seen explosive improvement in thermoelectric performance, achieving up to ZT=0.2.[19,20,101] Generally, these polymers have a conjugated backbone, often containing thiophene-derivative repeat units. It is these conjugated core motifs that enable charge transport, while side chains are usually responsible for aiding in solution-processability and molecular assembly in the solid state (see Figure 3.1 for several prototypical organic thermoelectric molecules). Such organic materials usually manifest in the solid-state as polycrystalline solids. Because the mobility of carriers in organic domains is known to depend strongly on electronic coupling between molecules, both molecular structure and assembly are critical factors in determining the overall thermoelectric properties of organic materials.[102] This material class is rich with recent work and developments, which several excellent reviews have recently detailed comprehensively.[5–7,103] Here, we will focus instead on gaps and critical challenges remaining within the field. Further, in light of the potential applications for STEGs, we believe it is important to place particular emphasis on solution-processed materials, which are exceptionally attractive in the effort to realize printed thermoelectrics for practical application.

On the other hand, high performing, stable *n*-type STEs remain relatively scarce. Organic molecules typically exhibit large HOMO-LUMO (highest occupied molecular orbital-lowest unoccupied molecular orbital) gaps with shallow LUMOs. Carriers occupying shallow LUMO levels tend to be highly reactive, causing *n*-type doping in such materials to be unstable, and designing molecules that circumvent this issue has proven challenging.[104] Nonetheless, several STEs have recently been reported to have stable *n*-type thermoelectric properties, albeit with performances lagging behind their *p*-type counterparts. State-of-the-art in this material class include poly(metal 1,1,2,2-ethenetetrathiolate) (poly(M-ett)) derivatives – conjugated polymers with metal ions in the backbone.[88] Using Nickel as the central metal ion, Sun *et al.* demonstrated power factors up to 66 $\mu W/mK^2$.[105] A critical drawback to this material class is that the polymers themselves tend to be insoluble, relying on solid-state powder processing. This element makes them unsuitable for solution-based techniques and thus unfavorable from a processing/fabrication standpoint. While utilizing a soluble binder could circumvent this issue, the necessary powder processing increases fabrication complexity and incurs additional associated costs. It is preferable to instead develop solution-processed *n*-type STEs, among which the highest thermoelectric performances have been observed in doped single-walled carbon nanotubes and halogenated benzodifurandione-based oligo (*p*-phenylene vinylene) (BDPPV) derivatives, with power factors of 18 and 28 $\mu W/mK^2$, respectively.[106–108] Also worth noting are perylene diimide derivatives

(PDIs), a family of small molecule *n*-type semiconductors with excellent solution processability capable of being synthesized large scale / low cost, and fullerenes, spheroidal conjugated carbon networks with notably low thermal conductivities.[109,110] The top performing PDI has demonstrated power factors up to 1.4 μW/mK^2 and top performing fullerenes 30 μW/mK^2, as of yet insufficient for practical applications.[109,111–114]

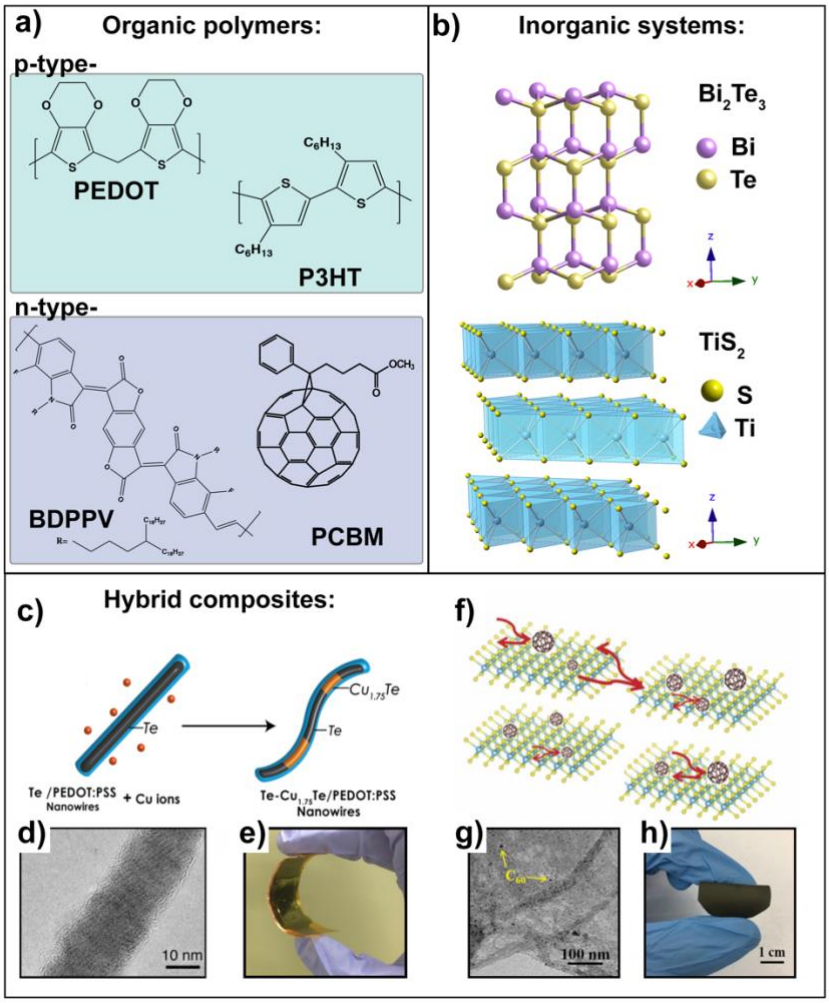

Figure 3.1 Summary of common STE materials. Chemical structures are given for (a) common thermoelectric polymers and b) inorganic thermoelectric semiconductors. High performing hybrid organic-inorganic composites include *p*-type Te-$Cu_{1.75}Te$/PEDOT:PSS nanowires ((c) schematic depiction of synthesis, (d) transmission electron microscopy (TEM) image, and (e) optical image), and *n*-type TiS_2/C_{60} nanosheet/nanoparticle composite ((f) schematic depiction of C_{60} nanoparticle intercalation, (g) TEM image and (h) optical image).

3.2 Organic-Inorganic Composite Thermoelectrics

Drawing on developments in both organic and inorganic semiconductors, the field of hybrid organic-inorganic composite thermoelectrics has seen rapid progress in the past decade. While there is still contentious debate over exactly how hybrid materials are able to outperform their individual components, it is clear that the organic-inorganic interface plays a critical role.[26,115–117]

Thus, ideal hybrid material design includes large interfacial areas and precise control over the interfacial properties, as well as favorable physical interaction between the organic and inorganic phases. Additionally, composites of organic and inorganic materials are not necessarily mechanically flexible. Creative and intelligent design procedures must be employed to leverage the mechanical properties desired from the organic phase while achieving satisfactory thermoelectric performance. Hybrid design strategies will be discussed in the following sections. A large selection of state-of-the-art STE materials are collected, and their thermoelectric properties are shown as a function of electrical conductivity in Figure 3.2. Hybrid materials systems are highlighted as among the highest performing STE materials and are particularly able to contribute high-performance n-type materials, which organic materials alone have difficulty doing.

While STE materials development has seen encouraging and rapid progress in recent years, there is room for the field to advance at a process-level. With a large pool of candidate materials and extensive list of tunable material and film parameters, it is only natural that exhaustive trial-and-error materials discovery efforts are limited in both rate and scope. Data-driven methodologies such as machine learning have been integrated with encouraging results in fields like bioinformatics, but have been slow to spread in materials science, likely due to the complexity and variety of materials data.[118,119] Early efforts have been slowed by challenges such as communicating between data sets with nuanced structural differences, parsing unstructured data, and combining multiple data sources.[90,120–122] Considerable interest in this line of investigation has sparked the launch of multi-agency initiatives such as the Materials Genome Initiative and Materials Project.[123,124] This is an area of active and dynamic research facing substantial challenges.

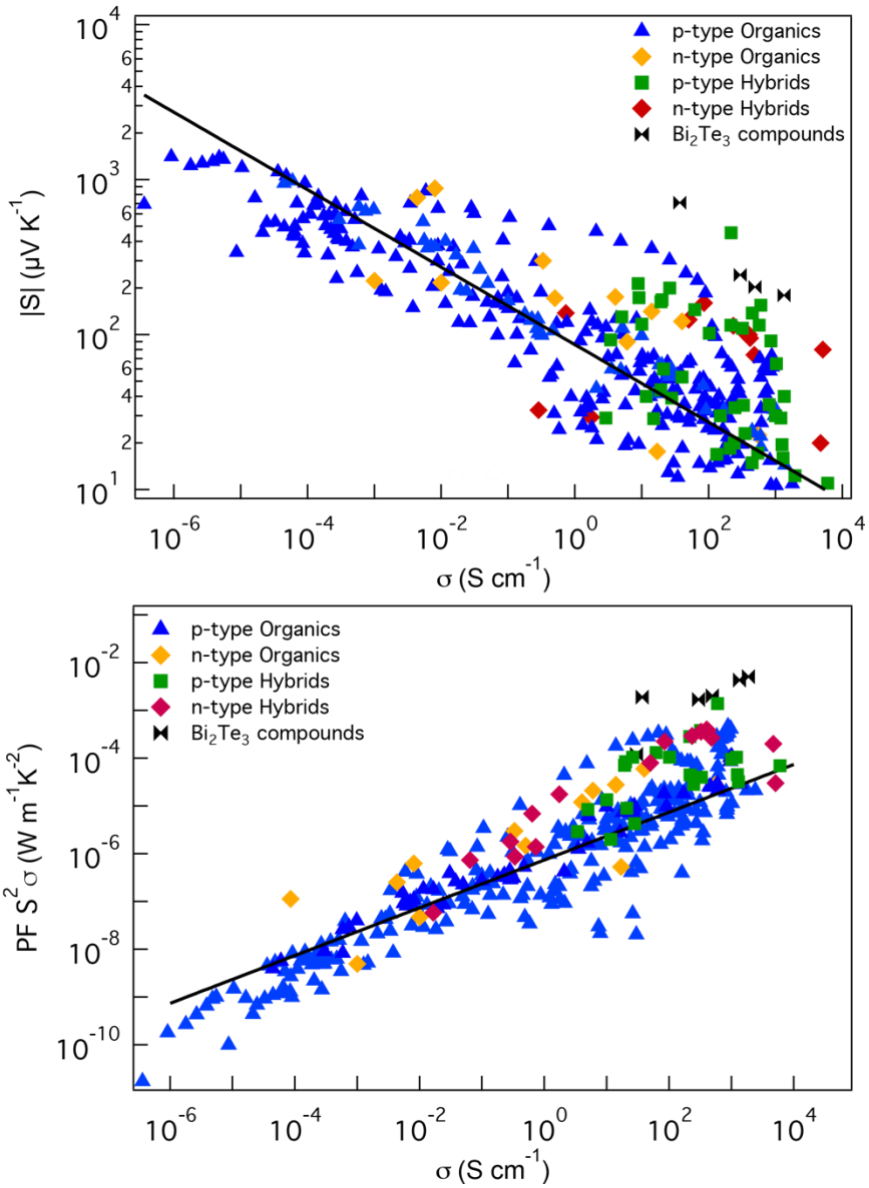

Figure 3.2 Summary of the thermoelectric properties of a wide variety of organic and organic-inorganic STE materials.[5] The Seebeck coefficient (S, top) and power factor (PF, bottom) are plotted as a function of electrical conductivity (σ). The black lines represent the empirical relations $\boldsymbol{S \propto \sigma^{-1/4}}$ (top) and $\boldsymbol{PF \propto \sigma^{1/2}}$ (bottom). Hybrid material systems are highlighted as among the highest performing STEs.[12,24–26,51,52,52,56–60,74,82,116,125–134] High performing Bi_2Te_3 compounds are included for reference as the benchmark room-temperature thermoelectric material.

3.3 p-type Organic-Inorganic Composite Thermoelectrics

There are several ways to design composite materials, the most popular of which is to separately synthesize the inorganic and organic components, and then to physically mix them, either in solution or in the solid state. Often this takes the form of inclusion of inorganic nanoparticles in a polymer matrix. This is an intuitive approach, but by no means the most effective. When mixing distinct components, one has little control over the formation of interfaces and dispersion of

nanoparticles and phase segregation or discontinuity can lead to poor or anomalous and irreproducible transport properties. Additionally, because nanostructures typically require surface ligands to provide stability and solution-processability, interaction between the active materials is softened by inactive surface species. Surface ligands tend to be electronically insulating, detracting from the aggregate performance of the resulting composite. While these composites can demonstrate enhanced thermoelectric performance, the underlying physics is often elusive due to the complex and chaotic nature of the composites. Nonetheless, this approach represents a viable method for preparation of hybrid organic-inorganic composites with enhanced thermoelectric performance. For example, He *et al.* demonstrated high performing hybrid composite comprising Bi_2Te_3 nanowires embedded in a P3HT matrix.[26] The authors observed a fivefold improvement in the Seebeck coefficient, which they attributed to carrier energy scattering. The physical mixture approach can be extended to increasingly complex systems. Choi *et al.* prepared three-component composite thermoelectrics using PEDOT:PSS, single walled carbon nanotubes (SWCNT), and gold nanoparticles, observing very high conductivities.[125] The authors concluded that the gold nanoparticles acted as dopants to the SWCNT in the system, and treated the PEDOT:PSS as mostly an inactive matrix.

Alternatively, *in situ* approaches tend to provide more intimate interphase interactions, with direct control over the interfacial properties. In 2010, See et al. reported a synthesis for PEDOT:PSS-Te nanowires (NWs), where PEDOT:PSS acts as both a structure-directing agent and stabilizing ligand in the formation of the Te NWs. These composites demonstrated surprisingly high electrical conductivity, exceeding either individual component and achieving a ZT~0.1.[24] Using a three-component model and AC impedance studies, it was suggested that, at the nanoscale organic-inorganic interface, there exists a high conductivity interfacial region that is responsible for the enhanced transport observed at the macroscale.[76,115] In addition to enhanced transport at the hard-soft interface, the authors suggest that energy filtering likely plays a role in the composite performance due to the work function matching between PEDOT:PSS and Te. In fact, most reports in this hybrid class of materials implicate one of the following mechanisms in observed high thermoelectric performance: 1) energy filtering, 2) locally enhanced transport at the organic-inorganic interface, and 3) interphase charge transfer/doping. While it is likely all three mechanisms are active to some degree, it is our opinion that the role of energy filtering has been overestimated in this field, in large part due to the difficulty of directly observing these three phenomena or disentangling the complex set of interactions. In principle, to strongly suggest that energy filtering as an operative mechanism requires careful temperature-dependent measurements and materials of high-enough quality such that the relevant scattering lengths exceed material dimensions. In practice, few works have achieved this level of rigor for these families of organic and hybrid materials.

Researchers often cite theoretical values for work functions or HOMO/LUMO levels to predict material combinations that will enable energy filtering. However, these theoretical values are often tabulated for bulk materials; it is well known that nanomaterials exhibit shifts in these energetics. In 2017, Liang *et al.* reported on the role of energy filtering in enhanced thermoelectric performance of a hybrid P3HT-Te nanowire system.[82] In this work, the authors used ultraviolet photoelectron spectroscopy to confirm the relevant work functions instead of using tabulated values. Despite the appropriateness of the work functions and the observed improvement in thermoelectric performance, the authors concluded that energy filtering was not a contributing

factor. More recently, we performed a detailed study of a PEDOT:PSS-Te(Cu_x) hybrid material system, in which energy filtering had been similarly implicated. A full suite of experiment, simulation, and modeling was used to disentangle the complex physics underlying the observed thermoelectric trends. Again, it was concluded that energy filtering, or a modification of the energy dependent scattering in the system, was not responsible for the high thermoelectric performance achieved in these composites. Instead, the key transport properties were dominated by the effects of polymer morphology at the organic-inorganic interface and interfacial charge transfer. That is, it was observed that the organic polymer, in this case PEDOT, self-assembled into a highly ordered structure at the inorganic surface (Figure 3.3). It is well known that the crystallinity and structure of polymeric domains is strongly correlated to the electrical conductivity and carrier mobility of the polymer.[102] This physical templating effect caused the formation of a region of locally enhanced carrier transport at the organic-inorganic interface. While this is in line with the early hypotheses proposed by Coates *et al.*, this was the first theoretical observation of such a templating effect in an organic-inorganic hybrid thermoelectric system.[115] Further, DFT calculations revealed that charge transfer occurred at the PEDOT-Te/PEDOT-$Cu_{1.75}Te$ interfaces, causing a de-dedoping effect in the PEDOT phase. This dedoping was in part responsible for the enhanced Seebeck coefficient observed in this system, which had been previously interpreted as indicative of a modification in the energy-dependence of carrier scattering. Given that this physical templating effect is a key factor in high performing organic-inorganic hybrid thermoelectrics, next-generation materials should be designed with this phenomenon in mind. While pursuit of record-breaking performance is critical in the field of STEs, careful study of the physical mechanisms behind enhanced transport in complex hybrid systems remains a subject in need of further and broader investigation in this field.

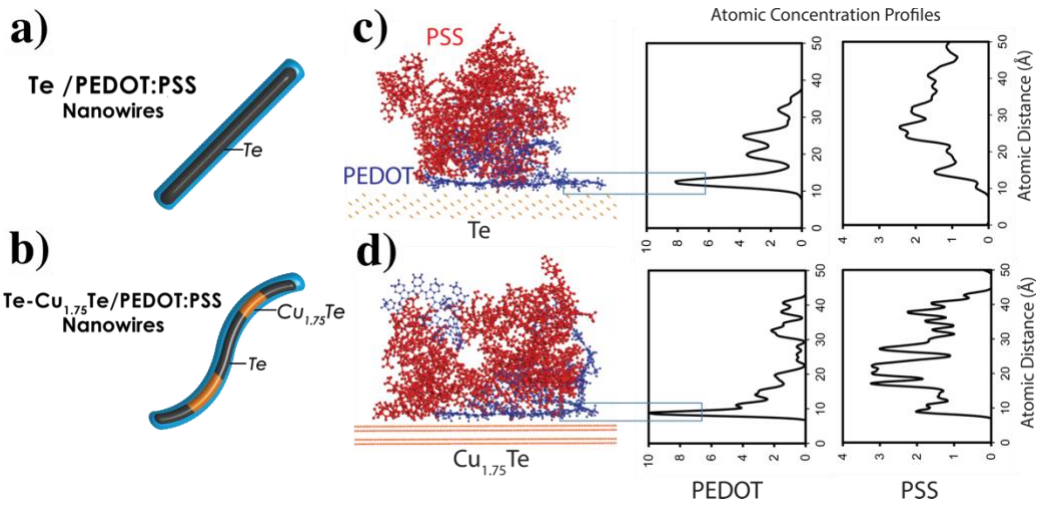

Figure 3.3 Theoretical studies reveal that a physical templating effect of PEDOT on the inorganic Te surface in PEDOT:PSS-Te(Cu_x) nanowires creates regions of high local ordering/alignment of PEDOT molecules at the hard-soft interface.[75] Cartoon depiction are shown for (a) PEDOT:PSS-Te NWs and (b) PEDOT:PSS/Te-$Cu_{1.75}Te$ NWs. Molecular dynamics simulations reveal morphology and alignment of PEDOT (blue) and PSS (red) molecules on the surface of (c) Te and (d) $Cu_{1.75}Te$ surfaces, both accompanied by respective atomic concentration profiles.

Another point of contention in the hybrid thermoelectric literature is the relative contribution of the organic or inorganic phases to the overall transport properties. While many reports treat the inorganic components as active thermoelectric material and the organic as a filler matrix, there is abundant evidence that the organic component plays an active role in carrier transport. For example, by applying the Snyder model, our recent work provides evidence that the high performance in the PEDOT-Te(Cu_x) system is driven primarily by thermoelectric transport in the organic phase. The thermoelectric trends in this system are only fit by a scattering parameter s=1, a signature of transport in PEDOT domains. Careful controls were used to show that transport in the Te domain in the absence of PEDOT did not adhere to the same s=1 fit. The implication here is that the contribution of the inorganic phase is largely as a template for the organic component and for its role in the interfacial dedoping of PEDOT. In the case of PEDOT, this result is ultimately not too surprising; single crystal PEDOT has been reported to achieve up to a remarkable 8800 S/cm, and so highly ordered PEDOT channels can be expected to dominate carrier transport in semiconductor composite systems.[65]

In fact, PEDOT has been such a critical element in recent STE progress that almost all top performing hybrid systems utilize PEDOT as the organic component. One element that is shared between current state-of-the-art materials is careful control over the organic-inorganic interface. The PEDOT-Te nanowire system, created *in situ* and therefore with very intimate bonding between the hard and soft phases, has been reported to reach power factors as high as 280 $\mu W/mK^2$ using sulfuric acid post-treatment.[51] Ju *et al.* prepared a composite of exfoliated nanosheets of SnSe and PEDOT:PSS, exhibiting a power factor of 380 $\mu W/mK^2$ (ZT~0.32 at room temperature).[126] More recently, Wang *et al.* demonstrated remarkably high performance in a flexible PEDOT-Bi_2Te_3 nanoparticle system, achieving a power factor up to ~1350 $\mu W/mK^2$, corresponding to ZT~0.58 at room temperature.[73] For reference, prototypical Bi_2Te_3 materials demonstrate power factors around 2000-4000 $\mu W/mK^2$.[135,136] In this work, nanoparticles of Bi_2Te_3 are periodically and carefully deposited on a substrate in a regular pattern (Figure 3.4). A continuous phase of conducting PEDOT is formed directly onto these nanoparticles using vapor polymerization. Here, the authors suggest that the organic PEDOT phase is responsible for the high conductivity of the films, whereas the monodispersed Bi_2Te_3 particles provide phononic scattering modes that reduce the thermal conductivity and enhance the overall thermoelectric figure of merit. In addition to the periodic nanoparticle dispersion, this technique benefits from vapor polymerization of PEDOT directly onto the nanoparticle surface; vapor polymerization has been shown to form PEDOT films with a high degree of crystalline ordering and circumvents the need for insulating PSS moieties. However, vapor techniques are costly to scale up and tend to be much more expensive from a fabrication standpoint than solution-based techniques, restricting the practical application of such an approach.

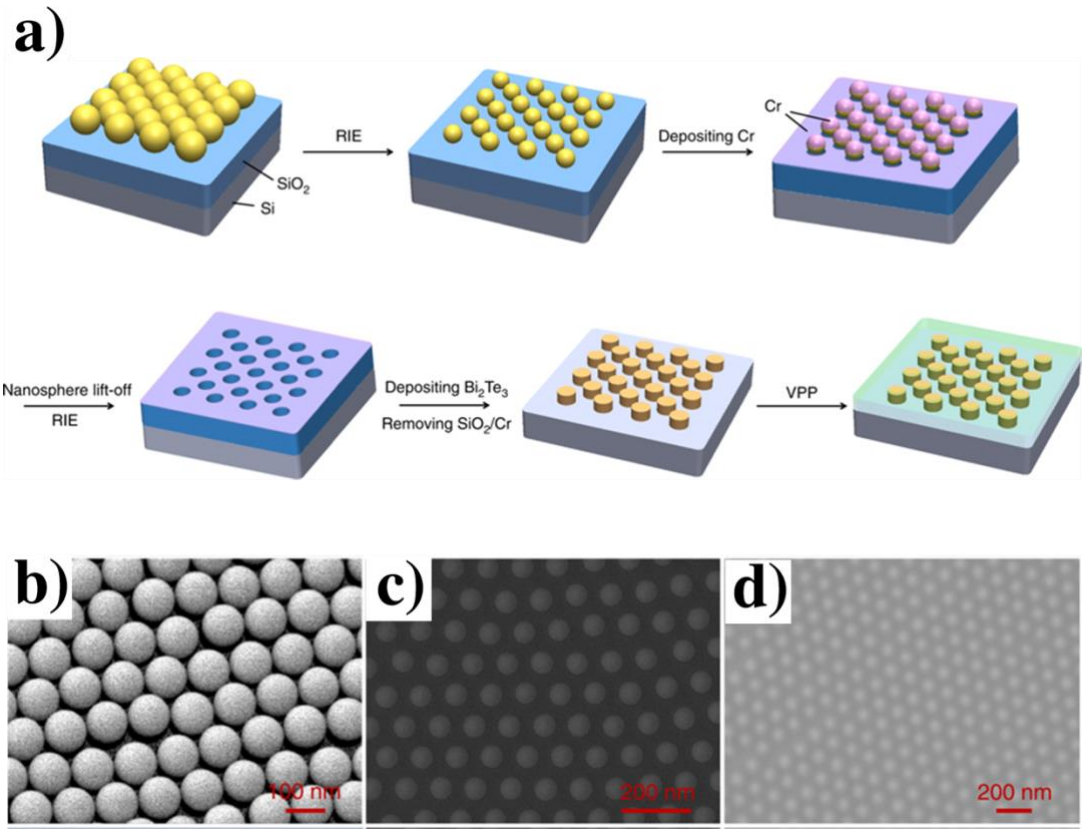

Figure 3.4 High thermoelectric performance is achieved in a PEDOT-Bi_2Te_3 nanoparticle composite via deposition of a periodic array of Bi_2Te_3 to disrupt phonon transport.[73] (a) Schematic diagram of synthetic method. Scanning electron microscopy (SEM) images are depicted for b) closely packed polystyrene nanoparticles used to create the periodic pattern, c) Bi_2Te_3 nanoparticles deposited using this pattern, and d) PEDOT-Bi_2Te_3 hybrid films after vapor deposition of PEDOT. All panels reproduced with permission.[73] Copyright 2018, Springer Nature.

3.4 n-type Organic-Inorganic Composite Thermoelectrics

The impressive progress in hybrid STE materials discussed thus far has focused on *p*-type systems. There has also been progress in *n*-type hybrid thermoelectrics, but these instances are far scarcer, as can be seen in Figure 3.2. The fundamental reasons for this were stated earlier and developing high-performing n-type materials remains a fundamental challenge to the field of STE, perhaps requiring synthesis of new derivatized polymers or new classes of hybrid materials. Currently, the top performers in this category tend to rely on *n*-type Bi_2Te_3 materials. For example, Zhang *et al.* used a layer-by-layer deposition technique to achieve a power factor of 80 $\mu W/mK^2$ in *n*-type PEDOT-Bi_2Te_3 films.[127] Combining *n*-type Bi_2Te_3 with carbon nanotubes, An *et al.* were able to prepare flexible thermoelectric films with a power factor of 225 $\mu W/mK^2$.[116] Recently, Wang *et al.* reported an approach to creating composites of C60 fullerenes with TiS_2 to rival the performance of single crystal TiS_2, achieving a power factor of ~ 400 $\mu W/mK^2$ and ZT=0.3 at 400K, significantly exceeding other state-of-the-art in solution printable *n*-type materials.[52] While the TiS_2 was synthesized in the solid-state, the composite was solubilized, enabling solution printing of the hybrid material onto flexible substrates (Figure 3.1f). Further, the authors prepared a flexible thermoelectric device (using a PEDOT:PSS/SWCNT ink as the *p*-leg), generating up to

350 nW of power at a 20K temperature gradient. While these materials are able to leverage solution-based printing techniques, the synthetic requirements still represent an issue practically, as the TiS_2 synthesis involves 4 days of continuous heating between 450-650°C, followed by solid-state processing and ball milling.[137] Nonetheless, this represents a remarkable step forward in *n*-type hybrid material development. Further work on this material system will likely be fruitful in advancing state-of-the-art and expanding the number of feasible *n*-type hybrid material systems.

3.5 Demonstrated Thermoelectric Devices

Typical thermoelectric modules are composed of alternating *p*- and *n*-type legs connected electrically in series and thermally in parallel. While unileg devices are possible, by utilizing both *p*- and *n*-legs, and by connecting many legs in series, it is possible to produce large output voltages across the device. As previously discussed, this device voltage is an important consideration for pairing a TEG with a compatible technology. However, many other considerations are relevant for the effective design of functional TEGs. Beyond the choice of high-performing materials, considerations such as leg geometry, fill factor, and electrical impedance matching all contribute to optimizing power generation from a TEG. Due to decades of development, design strategies for rigid, inorganic-based thermoelectric modules are well established. On the other hand, design of STEG modules presents challenges quite distinct from the current best practices. Solution-based techniques, specifically roll-to-roll and other printing methodologies, typically result in structures with micron-scale thickness, deposited onto a substrate. In most approaches, this translates to precise 2-dimensional control over leg width and length, but a lack of control over leg thicknesses. The STEG field is currently in early development stages, with focus on proof-of-principal demonstrations.[9,30,51,138–142] Many of these reports include power generation measurements performed on 2D planar modules. However, to probe the practical performance of new materials in STEG modules, it is important to design more realistic module architectures. State-of-the-art involves creative strategies to convert printed 2D arrays into functional 3D architectures (Figure 3.5). Often, leveraging the unique mechanical advantages offered by STEGs, these 3D architectures involve rolling, folding, or stacking of 2D printed arrays of thin film legs.[138] Corrugated architectures have been fabricated using thermal and mechanical techniques as well.[143] Proof-of-concept demonstrations have been promising, but it will be crucial to ensure that such devices are robust against mechanical failures, including cracking and delamination.

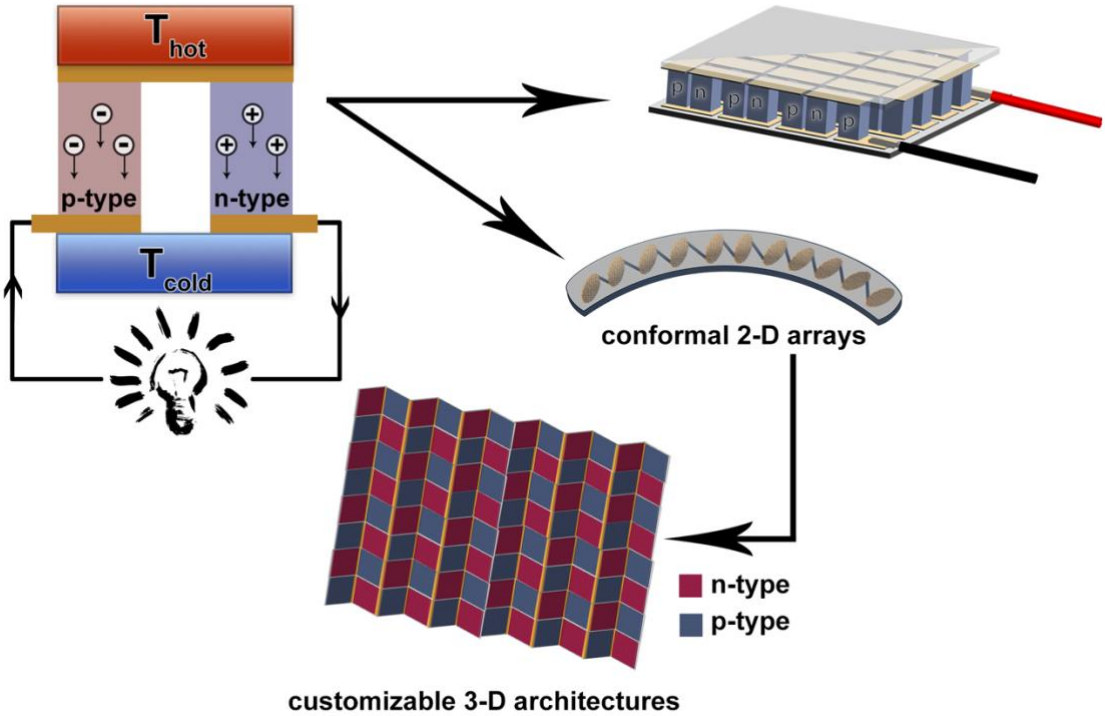

Figure 3.5 Transitioning to soft thermoelectric materials necessitates new strategies for thermoelectric module design relative to traditional inorganic thermoelectric devices. While traditional inorganic thermoelectric devices are constructed in rigid wafer geometries, STEs leverage inexpensive solution-based processing techniques, enabling the reliable patterning of 2D arrays of thermoelectric legs. These 2D arrays can be transformed into flexible and lightweight 3D architectures with a variety of geometries relevant for wearable and IoT applications.

Since the development and demonstration of STEG modules is relatively new, it is difficult to compare across reports. Every design is different, and maximum power generation depends on factors such as number of p-n couples, applied thermal gradient, and average measurement temperature. Some groups report power generation in units of energy, whereas some report in terms of energy per unit area. With printed STEGs, cross-sectional areas can be quite small, which can cause inflated results and confusion. We urge readers to be aware of these factors when evaluating the performance of STEGs in the literature. Additionally, only few reports as of yet include an assessment of device weight or power density per unit mass. As the field progresses towards more realistic devices, the weight of a device will become increasingly relevant. Table 3.1 provides a brief summary of some of the key STEG demonstrations in the current literature. Note that this table is not intended to be comprehensive, but to highlight several key results and to illustrate the heterogeneity of experimental conditions, as well as the variety of solution-based processing methods, being explored in the field.

In order to fabricate flexible thermoelectric devices, researchers have utilized strategies including all-organic devices[105,140], active organic-inorganic hybrid composites[9,51,52,139], and organic-inorganic composites where the organic component acts as an inactive binder element.[13,141,142] Initial demonstrations resulted in flexible STEGs capable of producing nanowatt level power. Top

performing organic-based STEGs typically produce on the order of 100s of nW/cm^2 to ~1 μW/cm^2. Successful STEGs have been fabricated using carbon nanotube[53,144–146] and PEDOT-based materials[19,30,140,147], but the highest performances in this class of materials have been achieved using the organometallic poly(M-ett) polymers discussed in section 4.1.[105] However, as previously mentioned, these particular polymers are typically insoluble and require solid-state processing unless solubilized with an additional binder element, rendering them less than appealing candidates for integration into large scale manufacturing processes.

There have also been several reports of organic-inorganic hybrid STEG devices. Most of these reports feature PEDOT-based materials, and the power generation achieved is on the order of 10s-100s of nW.[9,51,139] In a particularly promising result, Kim *et al.* produced flexible TEGs capable of generating remarkable power densities using a combination of screen printing and lift-off techniques (Figure 3.6).[141,142] In this approach, a thermoelectric paste is made using traditional inorganic alloys as the active materials (i.e. Bi_2Te_3/Sb_2Te_3 or $Bi_{0.3}Sb_{1.7}Te_3$/$Bi_2Se_{0.3}Te_{2.7}$) and organic binder materials for processability.[13,54] Such a paste can be made compatible with printing techniques, enabling the fabrication of flexible devices compatible with wearable or IoT applications. These designs resulted in outstanding power densities of ~3-5 mW/cm^2 using a 50K temperature gradient and 8 *pn* couples, indicating that this approach has strong merit for future work. However, the continued need for more expensive solid-state processing and use of toxic or rare elements limits the use of such devices in biological or personal-use applications.

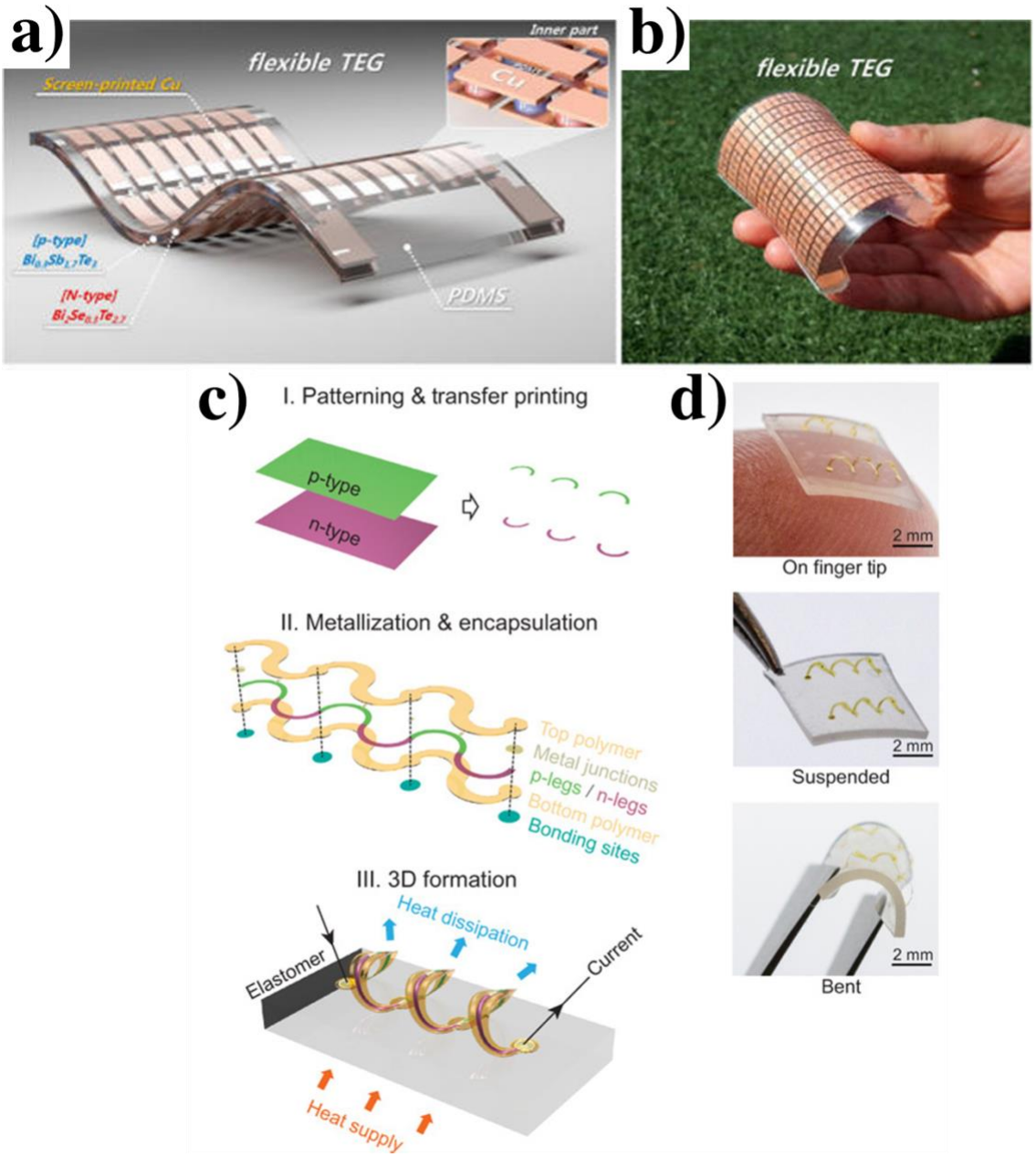

Figure 3.6 Innovative approaches to soft thermoelectric device design are being developed to fabricate flexible and lightweight thermoelectric devices compatible with wearable and IoT applications. (a) Rendering and (b) optical image of a high performing flexible thermoelectric module fabricated using a combination of screen printing and lift off techniques with a composite paste of inorganic alloy and organic binder.[141] (c) Schematic describing the process of fabricating interconnected arrays of 3D helical thermoelectric coils. The thermoelectric legs are first patterned in 2D using printing techniques, then transformed into a functional 3D array. (d) Optical images show lightweight and flexible mechanical properties of the resulting device.[100] Reproduced with permission.[141] Copyright 2016, American Chemical Society.

In another promising result, Wang *et al.* used exfoliated TiS_2 nanosheets, combined with C_{60} fullerene nanoparticles, to prepare a flexible STEG using solution-printing (discussed in section

4.2.2).[52] While TiS_2 is synthesized in the solid-state, the composite becomes solution-processable and therefore amenable to printing techniques.[137] Under a temperature gradient of 20K and using a simple SWCNT/PEDOT composite as the *p*-leg, the authors achieved up to 350 nW power generation using only 2 *pn* couples.

Table 3.1 Summary of key reports in recent literature demonstrating power generation in STEG devices. A number of solution-based fabrication and processing methods are utilized. The heterogeneity in experimental conditions is highlighted in the various values for ΔT applied during the power generation measurements, as well as the number of *pn* couples used in device design. *No effective device area was given, so the maximum power density is reported rather than maximum power output. **Note that fabrication of this device utilized solid-state processing (compressed pellets of polymer), allowing for the realization of significantly more power output. This approach does not leverage solution-based processing and likely does not achieve a mechanically flexible device but has been included as a reference point for high performing organic TEGs.

Type	Fabrication Methods	*p*-type Material	*n*-type Material	ΔT (K)	No. of Couples	Max Power Output	Ref
Organic	Ink Coating of Fabric	PEDOT:PSS	none	75	5	12 nW	[140]
Organic	Ink Printing	PEDOT:PSS	none	100	5	334 nW	[30]
Organic	Compressed Pellet**	poly[Cu_x(Cu-ett)]	poly[Na_x(Ni-ett)]	82	35	750,000 nW	[105]
Hybrid	Vacuum Filtration	PEDOT-Te NWs	Bi2Te3 NW	60	6	23 nW	[139]
Hybrid	Spin Coating	PEDOT:PSS	PEDOT:PSS-ITO	30	8	1.75 nW	[9]
Hybrid	Ink Printing	PEDOT:PSS-Te NWs	none	10	10	10 nW	[51]
Hybrid	Screen Printing; Laser Multi-scanning	$Bi_{0.5}Sb_{1.5}Te_3$	$Bi_2Te_{2.7}Se_{0.3}$	26	72	6320 uW/cm2*	[13]
Hybrid	Screen Printing	Sb_2Te_3	Bi_2Te_3	50	8	3800 uW/cm2*	[142]
Hybrid	Ink Printing	PEDOT:PSS-SWNT	TiS_2-C_{60}	20	2	335 nW	[52]

Chapter 4. Enhanced Power Factors in PEDOT:PSS Hybrid Thermoelectrics

Adapted from "Carrier Scattering at Alloy Nanointerfaces Enhances Power Factor in PEDOT:PSS Hybrid Thermoelectrics," EW Zaia, A Sahu, P Zhou, MP Gordon, JD Forster, S Aloni, YS Liu, J Guo, JJ Urban, *Nano Letters*, 2016, 16.5, 3352–3359 (DOI: 10.1021/acs.nanolett.6b01009) with permission of the authors. *Reproduced with permission of Nano Letters*.

4.1 Abstract

This work demonstrates the first method for controlled growth of heterostructures within hybrid organic/inorganic nanocomposite thermoelectrics. Using a facile, aqueous technique, semimetal-alloy nanointerfaces are patterned within a hybrid thermoelectric system consisting of tellurium (Te) nanowires and the conducting polymer poly(3,4-ethylenedioxythiophene): poly(styrene-sulfonate) (PEDOT:PSS). Specifically, this method is used to grow nanoscale islands of $Cu_{1.75}Te$ alloy subphases within hybrid PEDOT:PSS-Te nanowires. This technique is shown to provide tunability of thermoelectric and electronic properties, providing up to 22% enhancement of the system's power factor in the low-doping regime. This work provides an exciting platform for rational design of multiphase nanocomposites and highlights the potential for engineering novel hybrid thermoelectrics via introduction of interfaces with controlled structural and energetic properties. Additionally, this material platform represents an ideal prototype to systematically examine the physics underlying enhanced carrier transport in hybrid materials and the role of carrier filtering; such an investigation is detailed in Chapter 5.

4.2 Introduction

Hybrid solution-processed thermoelectric devices are uniquely poised among renewable energy technologies as they offer the opportunity to directly convert waste heat to electricity while simultaneously leveraging the advantages of inexpensive roll-to-roll fabrication and conformal geometries to maximize heat capture[1–4]. To date, application of traditional inorganic thermoelectric devices has been restricted to niche markets by high costs and low efficiencies[5]. Solution-processed hybrid materials offer a promising route to develop new, low cost thermoelectric devices by avoiding high-energy processing methods, but as of yet still require efficiency gains to become commercially feasible[1,6–8]. For a given temperature T, the efficiency of a thermoelectric device is typically characterized using a dimensionless figure of merit, $ZT=S^2\sigma T/\kappa$, which encompasses three material properties: the Seebeck coefficient or thermopower S, electrical conductivity σ, and thermal conductivity κ. Despite the fact that ZT has no theoretical limit, device performance has proven difficult to enhance due to the anti-correlation of S and σ in both inorganic and organic material systems; improving one parameter often comes at the expense of the other[9].

Classical approaches to optimizing the power factor ($S^2\sigma$) have typically involved optimizing semiconductor doping to balance S and σ[9]. However, only a few materials have bypassed ZT=1 using this approach, even at the lab-scale[9–11]. Thus, in recent years, great research emphasis has been placed on using the unique tools of materials science to introduce alternative approaches to enhancing the power factor, such as resonant states, minimizing bipolar effects, and modifying the

energy-dependence of carrier scattering[12,13]. This latter strategy leverages a phenomenon known as carrier filtering. In this mechanism, a tall energetic barrier is established in either the conduction or valence band (for n- or p-type conductors respectively) which selectively scatters low-energy charge carriers, causing asymmetry in the distribution of mobile charge carriers around the energy level of the potential barrier[14–16]. Since the Seebeck coefficient of the system is directly related to the asymmetry of the carrier distribution about the Fermi energy, careful alignment of this potential barrier near the Fermi level can provide systematic improvement in thermoelectric performance[5,17]. Alternatively, introduction of energy-independent scattering mechanisms has been shown to drastically impact electrical conductivity while leaving Seebeck coefficient largely unaffected[18]. Successful examples of controlling the energy-dependence of scattering events are few in number and typically involve careful engineering of carrier transport paths within the system[19–21]. In these cases, the system experiences a modest decrease in overall conductivity while realizing large gains in Seebeck coefficient. Since ZT is quadratically dependent on Seebeck coefficient and only linearly dependent on electrical conductivity, an overall enhancement in the power factor $S^2\sigma$ can be realized. However, many of these studies involve complex and poorly characterized structures or carrier transport paths with very specialized interfacial interactions, rendering it difficult to extend the results into other systems.

In this work, we present a novel and versatile colloidal technique for the patterning of alloy subphases with known energetics within solution-processable hybrid nanocomposites. To our knowledge, this is the first example of controlled growth of alloy subphases within hybrid nanocomposites. This is an appealing concept – allowing for controlled nanoscale doping or subpatterning within the growing class of complex organic/inorganic hybrid materials enables rational design of materials with three or more distinct subphases. However, the challenges are manifold: at the most basic level it is entropically more difficult to reliably structure three different materials classes than it is two, or one. Mitigation of these challenges is assisted by the choice of a favorable base material system. Beneficial criteria include (1) a well-defined nanostructure, which allows for isolation of any structural changes due to subphase growth, (2) a single crystalline primary phase so as to form predictable and reproducible interfaces upon initial subphase growth, and (3) facile solution-based synthesis. Our model system for this alloy patterning study is a well-characterized hybrid nanocomposite system composed of tellurium nanowires (Te NW) coated with conducting polymer poly(3,4-ethylenedioxythiophene): poly(styrene sulfonate) (PEDOT:PSS). We have previously reported aqueous synthesis of the PEDOT:PSS-Te NW resulting in well-defined, single crystalline Te nanowire cores coated with a layer of PEDOT:PSS (~150 meV work function offset)[22]. This material demonstrates high thermoelectric performance (ZT~ 0.1 at room temperature), in part because the PEDOT:PSS-Te nanocomposite unexpectedly achieves greater electrical conductivity than either pure component while maintaining the inherently low thermal conductivity of the native polymer (~0.2 $Wm^{-1}K^{-1}$)[22–24]. Significant effort has gone into characterization of the carrier dynamics in this system, as well as optimization of the power factor (up to 100 $\mu Wm^{-1}K^{-2}$)[18,23,25]. In this work, we induce the controlled patterning of varying amounts of Te-metallic alloy subphases within the existing nanostructure and characterize the resulting change in thermoelectric and electronic properties. Due to the facile, robust nature of the material synthesis, we are able to produce large volumes of material in a single batch, enabling statistical analysis of properties as a result of differing extents of subphase patterning while avoiding batch-to-batch variation. In theory, such a material system should have energetics

appropriate for energy dependent scattering, although further investigation is needed to draw any conclusions on this effect (see Chapter 5).

In order to effectively leverage carrier filtering effects, a high degree of interfacial area must be established with an appropriately sized energy barrier across the interface. This barrier should be high enough to scatter low energy carriers, but low enough to maintain a high carrier concentration and electrical conductivity, typically in the range of 1 – 10 k_BT, where k_B is the Boltzmann constant[14,19]. One established strategy for the formation and control of these barriers is the growth of metal-metal or metal-insulator heterostructures in existing materials[26,27]. First, two-dimensional (2D) quantum wells and superlattices were studied and shown to have significant potential for ZT enhancement. However, these systems are limited by strict requirements for epitaxy, scalability, and cost. One-dimensional (1D) nanowires are advantageous because they feature relaxed epitaxy and physics can be directly interrogated on a single nanowire basis. A host of well-explored vapor-phase deposition techniques exist for precise patterning of one-dimensional (1D) nanostructures[28–32]. For example, scientists have carefully grown 1D superlattices using molecular beam epitaxy[31,32]. These structures provide an important proof of principle for precise tuning of energetic and optical properties in 1D systems but are limited by high costs and lack of scalability. Alternatively, inclusion of nanoparticles in a matrix of thermoelectric material has been successfully used to improve thermoelectric performance, but this route suffers from insufficient control over the resulting interfaces and nanoparticle dispersion[33–37]. Instead, what is required is engineering of target materials with well-defined interfaces and energetics. Recent advancements in colloidal approaches have opened the door for controlled formation of versatile 1D heterostructures or superlattices with low cost solution-based techniques[38–41]. While this route has been successfully utilized with purely inorganic materials, we are the first to adapt it to rationally designed nanopatterned hybrid materials, with implications for not only thermoelectric applications, but also light-emitting diodes, photovoltaics, and other optoelectronic devices[40,42,43]. By leveraging interfacial control within patterned colloidal nanostructures, we utilize alloy subphase growth within the PEDOT:PSS-Te NW system to attempt to tune the energy dependence of carrier scatting.

For the identity of the subphase, copper was selected based on its high ionic mobility and modest energetic mismatch with Te (~300 meV offset in work functions between Te and Cu or ~150 meV offset between Te and $Cu_{1.75}Te$, a commonly observed alloy)[44–46]. This work function mismatch corresponds to the generation of an energy barrier of roughly 12 k_BT for the pure components, or 6 k_BT for the Te-alloy system. This model system is well suited to robustly demonstrate the effects of energetic barriers on carrier transport, although the barrier is tall enough that we expect some "hot" carriers to be scattered along with the majority of "cold" carriers. Using a simple aqueous technique, we demonstrate formation of $Cu_{1.75}Te$ alloy subphases with precise conversion within PEDOT:PSS-Te NWs (Figure 4.1a). The synthesis closely follows established methods to fabricate PEDOT:PSS-Te NWs with aspect ratios of 36 ± 4.0, consistent with previous studies[23]. After growth of the wires and prior to any cleaning steps, the reaction mixture is divided and aliquots of aqueous copper ions are injected to produce nanowires with varying amounts of copper loading, PEDOT:PSS-Te(Cu_x). Regardless of the copper precursor used, identical structures and material properties are obtained. The reactants are then stirred at room temperature for one hour. The nanowires are subsequently cleaned, and devices are prepared for characterization following established methods. Here, copper-loading ladders were performed with multiple samples

prepared at each of twelve copper loading levels. These samples range from undoped to lightly doped to fully exchanged nanowires. The extent of copper doping was measured using Inductively Coupled Plasma-Optical Emission Spectroscopy (ICP-OES) and confirmed with Energy Dispersive X-ray Spectroscopy (EDS), and the concentrations of organic and inorganic components in each sample was quantified using Thermogravimetric Analysis (TGA). Throughout this chapter, error bars represent the variation in measurements between samples. Any x or y error bars not visible are captured within the data points. Full experimental details are provided in the Supporting Information section.

4.3 Results and Discussion

Leveraging robust, large-scale PEDOT:PSS-Te NW synthesis, our method of colloidal subphase nanopatterning permits fabrication of PEDOT:PSS-Te(Cu_x) NWs with a variety of Cu loading extents from the same synthetic batch. This removes the need to perform a separate reaction to tune any given parameter of interest and isolates the system from unnecessary degrees of freedom. With this technique, we establish a precise baseline to isolate the effects of Cu doping on the carrier transport in the system. Since we are introducing foreign atoms into an existing lattice, it is first critical to understand how these atoms might distort the tellurium crystal structure and if Cu-Te alloys, metallic Cu nanodomains, or simply defects are formed. Hence, it is necessary to perform structural characterization of the resulting NWs. High-resolution transmission electron microscopy (HR-TEM) images of both PEDOT:PSS-Te and PEDOT:PSS-Te(Cu_x) NWs before and after subphase growth are shown in Figure 4.1. Since TEM samples only a countable few nanowires, scanning-electron micrographs are included in the Supporting Information to depict larger-scale organization. The nanowires are relatively monodisperse in size with an average length of 540 ± 50 nm and diameter of 15 ± 1.2 nm. The as-prepared PEDOT:PSS-Te NWs are rigid and primarily single crystalline, consistent with previous reports[22,47]. Interestingly, the TEM images reveal that the growth of alloy subphases is accompanied by a morphological transition from rigid rods to curved rods. Other groups have found this same phenomenon in similar systems, and it has been suggested that the curving of the nanowires is a signature of an increase in general material flexibility, presumably associated with a decrease in the elastic modulus of the nanowires[47]. We disagree with this hypothesis and propose that rod curvature is actually a result of structurally misaligned but highly crystalline semimetal or alloy domains at grain boundaries. HR-TEM images reveal a high degree of crystallinity at these bent regions instead of amorphous domains that would be expected to have enhanced flexibility. Instead, grain boundaries between misaligned crystal lattices exist at these bent regions, as seen in Figure 4.1e. STEM-EDS experiments revealed that Cu is concentrated within the bent regions, whereas Te is present throughout the full nanowire (Figure 4.8, in this chapter's Supporting Information section), implying that the bent regions of the nanowires are composed of Cu-Te alloy. Further, TEM analysis reveals that the kink angle in the PEDOT:PSS-Te(Cu_x) nanowires is widely distributed between 100 and 160 degrees. Mechanistically, this suggests that, during the transition from PEDOT:PSS-Te to polycrystalline PEDOT:PSS-Te(Cu_x) NWs, highly mobile Cu ions penetrate the Te lattice, likely at defect sites or grain boundaries, and nucleate an alloy crystallite from within the existing Te core. As additional Cu ions penetrate the nanowire, the alloy crystal grows and incorporates Te atoms already present. The growth of this new crystalline phase occurs at an angle relative to the original Te nanowire orientation (labeled θ in Figure 4.1e), causing the wire to kink in the process. In other words, structurally mismatched interfaces at grain boundaries cause kinks in the previously straight nanowires. Rather than an increase in mechanical flexibility, these angled domains are

responsible for the rod curvature, suggesting that mechanical flexibility would not be much altered from the original PEDOT:PSS-Te NWs. While the angle of the kink is related to both the lattice plane of $Cu_{1.75}Te$ growth and the Te facet at which the alloy nucleates, the heterogeneity of angles observed in the nanowires implies no strong orientational preference for growth of the alloy nanocrystals. However, due to the polycrystallinity of the alloy subphases and random distribution of crystalline orientations observed in these domains, more in-depth TEM studies are required to conclusively confirm or reject this hypothesis.

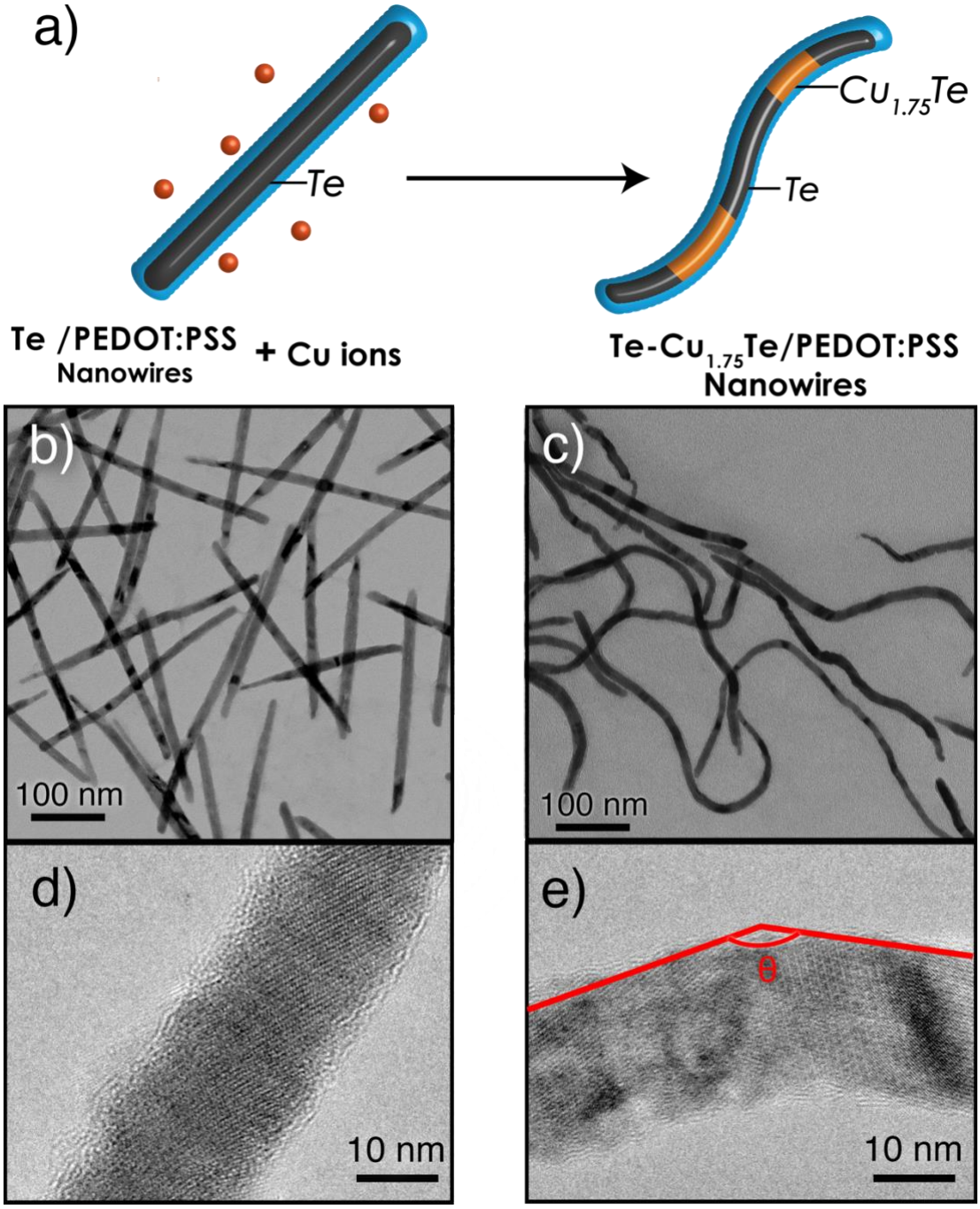

Figure 4.1 TEM images of nanowires with alloy subphases. (a) Cartoon depiction of Cu incorporation and nucleation of alloy phases within PEDOT:PSS-Te NWs. (b) The original

PEDOT:PSS-Te NWs are straight and rigid. (c) PEDOT:PSS-Te(Cu_x) NWs exhibit morphological transition to bent wires. (d) High-resolution TEM shows PEDOT:PSS-Te NWs before conversion are single crystalline. (e) PEDOT:PSS-Te(Cu_x) NWs appear polycrystalline and grain boundaries are observed at angled portions of 'bent' wires. The interface between two crystal domains results in angles (θ) ranging from 100 to 160 degrees, which defines the curvature of the 'bent' wires.

The extent of subphase growth can be carefully controlled by the addition of precise amounts of copper ions. Twelve samples were prepared with varying alloying extents, capturing the full spectrum from minor subphase growth to complete conversion of the Te core to a Cu-Te alloy. X-Ray Diffraction (XRD) spectra of these samples are shown in Figure 4.2. As expected, the as-prepared PEDOT:PSS-Te NW can easily be indexed to metallic Te^0 (International Center for Diffraction Data (ICDD) – PDF-4 #04-016-1605). After Cu addition, the majority subphase formed is $Cu_{1.75}Te$ (ICDD – PDF-4 # 04-007-0008), a copper-deficient analog to Cu_2Te, which has been observed as the thermodynamically-favored structure in several similar systems[47,48]. Surprisingly, the XRD patterns indicate the growth of the $Cu_{1.75}Te$ alloy phase even when very small amounts of Cu have been added to the system. In this low Cu loading regime, XRD patterns also depict the primary peak for CuO (ICDD – PDF-4 #04-014-5856), implying that a small amount of oxide impurities is present, which is unsurprising considering the reaction and film deposition are both carried out in air. No XRD peaks are observed for CuTe, the favored alloy at low copper loading in a bulk Cu-Te binary system. These results are corroborated by Cu $L_{2,3}$-edge X-ray absorption spectroscopy (XAS) using a synchrotron radiation source, which shows $2p^{3/2}$ characteristic transitions of both Cu^{+1} and Cu^{+2} species for samples even in the low copper-loading regime (Figure 4.12). These XAS spectra are consistent with previous reports of materials composed primarily of Cu^{+1} species (such as $Cu_{1.75}Te$) with a small amount of Cu^{+2} oxide impurities (CuO) due to the much larger absorption cross-section for Cu^{+2} than for Cu^{+1} species[49]. The preference for $Cu_{1.75}Te$ over CuTe subphases indicates a departure from bulk phase behavior, which is likely the result of strain fields caused by the presence of copper alloy nanoregimes between two segments of Te. Robinson *et al*. showed that the complex strain fields in one-dimensional colloidal nanocrystals can be leveraged to form periodic superlattice structures during growth of Ag_2S subphases within existing CdS nanorods[38]. A critical result was the formation of Ag-rich, locally stable Ag_2S islands in the high Ag loading regime. This phase segregation is driven by positive interfacial energies between the two materials and maintained by epitaxial strain. Alternatively, in systems where epitaxial strain does not play much of a role, Ostwald ripening causes the heterostructures to spontaneously convert to single-metal domains over time[50]. Here, the presence of stable localized $Cu_{1.75}Te$ subphases suggests that (1) there exists a positive interfacial energy between the Te and $Cu_{1.75}Te$ nanoregimes and (2) epitaxial strain and the geometric constraint of a 1D system is significant enough to cause stability against ripening and phase-mixing.

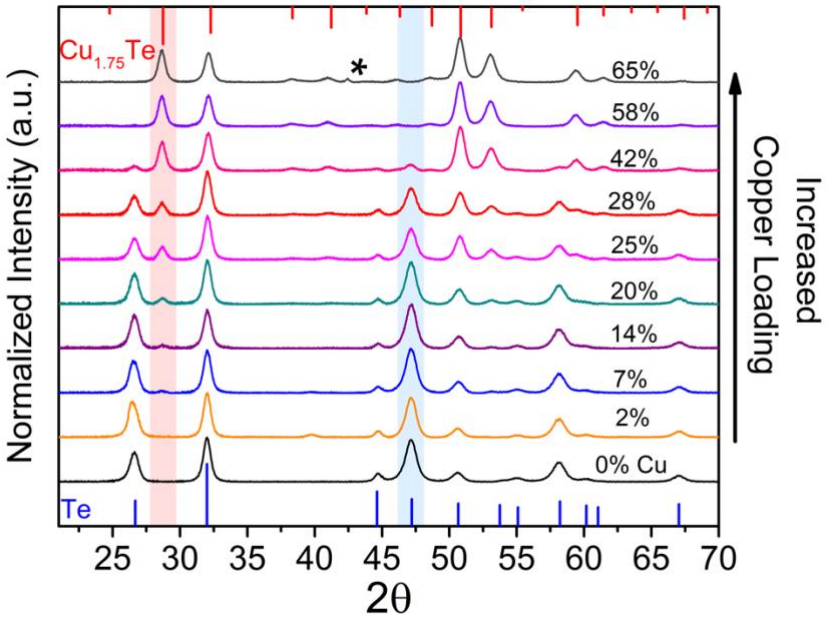

Figure 4.2 XRD spectra are shown for the PEDOT:PSS-Te(Cu_x) NWs. The reference lines given at the bottom of the figure correspond to Tellurium (ICDD - PDF-4 #04-016-1605) and match excellently with the PEDOT:PSS-Te (0% Cu) NWs. The reference spectrum for $Cu_{1.75}Te$ (ICDD - PDF-4 # 04-007-0008), shown at the top of the figure, matches the high copper-loading samples, indicating complete conversion to the alloy phase beyond 65 mol% Cu. The blue and red shaded regions respectively emphasize the disappearance of Te peaks and appearance of $Cu_{1.75}Te$ peak as copper loading is increased. The peak marked with an asterisk on the top spectrum does not match either starting material or product, but instead indicates the presence of Cu_2O impurities.

In the high copper loading regime, the XRD peak intensities corresponding to the $Cu_{1.75}Te$ structure increase relative to the Te peaks, indicative of higher conversion of Te to the alloy subphase. Also notable is that $CuTeO_3$ (ICDD PDF-4 #04-001-8705) and Cu_2O (ICDD PDF-4 #04-002-0905) are formed as minor products in the presence of large amounts of copper. The peak in Figure 4.2 marked with an asterisk corresponds with the major peak from a reference Cu_2O spectrum, and additional peaks for both impurity species are convolved with existing peaks in the $Cu_{1.75}Te$ spectrum. XPS spectra also support this claim and indicate the growth of characteristic Te^{+4} $3d^{5/2}$ peaks for samples above 40 mol % Cu (Figure 4.11 in the Supporting Information). The data also suggest that metallic copper domains exist in samples with high copper loadings, but quantification is difficult due to the convolution of Cu^0 and $Cu_{1.75}Te$ XRD and XPS peaks. Above 65 mol% Cu, no Te peaks are measurable, indicating complete conversion to PEDOT:PSS-$Cu_{1.75}Te$ NWs.

Given the coexistence of several Te and Cu oxidation states in the fully converted nanowires, the reaction mechanism is of particular interest. Originally, metallic tellurium nanowires are formed in a mild reducing environment (ascorbic acid) with a thin coating of PEDOT:PSS. Upon addition of the Cu precursor, highly mobile Cu^{+2} ions are reduced by the ascorbic acid to form some Cu^{+1} and some metallic Cu ions, which diffuse through the organic layer. Cu ions travel easily through the thin (~2 nm) PEDOT:PSS layer, as PEDOT:PSS forms an ion-transporting polymer layer with

high H^+ mobility[22]. Other studies have proposed that Cu ions induce the following surface reaction on the Te core: $3Te \rightarrow Te^{+4} + 2Te^{-2}$ [47]. Also likely is direct redox coupling by $2Cu + Te \rightarrow 2Cu^{+1} + Te^{-2}$. Cu^{+1} ions then react with Te^{-2} to form a stable, copper deficient $Cu_{1.75}Te$ alloy phase localized within the Te core. Additionally, since the reaction is carried out under air, some oxygen is expected to diffuse into the nanostructure. In the presence of large enough amounts of copper, Te^{+4} reacts with Cu ions and available oxygen to form detectable amounts of $CuTeO_3$ and unreacted Cu^{+1} ions form Cu_2O.

The thermoelectric and electronic properties of the hybrid system are shown in Figure 4.3. Most notably, at low copper loadings, an increase in the Seebeck coefficient is observed, which coincides with a modest drop in electrical conductivity. After optimization of PEDOT:PSS loading (details provided in the Supporting Information), a 22% increase in the maximum power factor of the system, up to 84 μW/mK^2, was realized. This is an unexpected result; standard effective medium theory predicts that the Seebeck coefficient of the composite will be intermediate between that of the endpoint materials (~190 μV/K for PEDOT:PSS-Te and ~10 μV/K for PEDOT:PSS-$Cu_{1.75}Te$ at room temperature)[47]. Instead, we measure enhancement of the Seebeck coefficient up to 220 μV/K in the composite, representing a 16% increase over the Seebeck coefficient of the unalloyed hybrid even before optimization of PEDOT:PSS loading. This trend was confirmed with four separate experiments to ensure reproducibility and demonstrate that this hybrid material robustly exceeds mean field predictions. This trend is possibly caused by a modification of the energy dependence of scattering due to the formation of an additional carrier scattering mechanism upon subphase formation. However, more deliberate study of the carrier physics in this system is necessary to make any further conclusions (see Chapter 5).

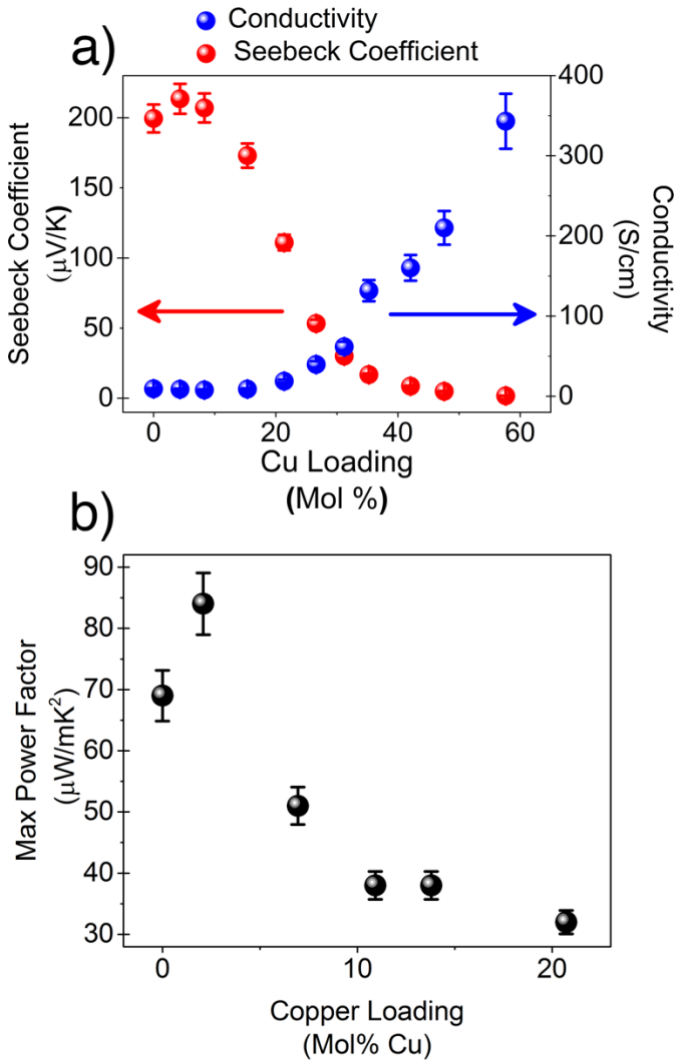

Figure 4.3 Electronic and thermoelectric properties of the PEDOT:PSS-Te(Cu_x) NW as a function of copper loading. (a) Non-monotonic trends in both Seebeck coefficient and electrical conductivity suggest the energy dependence of carrier scattering has been modified by growth of semimetal-alloy nanointerfaces. (b) Up to 22% improvement in the power factor of the system is realized upon initial subphase growth. Note that power factors are reported after optimization of PEDOT:PSS content, whereas the Seebeck coefficient and conductivity are reported before this optimization.

It is important to note that the net Seebeck coefficient and electrical conductivity values are measured from the nanowire mesh, so carrier transport at the interface between nanowires plays a significant role. However, in this study all thin films prepared have consistent close-packed nanowires mesh geometries, so that observed changes in electrical and thermoelectric properties are due solely to additional carrier dynamics induced by subphase growth. Additionally, it is known that PEDOT:PSS, as a blend of two ionomers, can interact strongly with additional ions. It is necessary to probe the interaction between PEDOT:PSS and Cu ions to ensure that it is, in fact, heterostructure formation that is responsible for the thermoelectric performance enhancement. For this purpose, PEDOT:PSS films were doped with varying amounts of copper, and the thermoelectric performance was characterized (full details in the Supporting Information

section). Figure 4.14 demonstrates that the Cu ions negatively impact transport in PEDOT:PSS, resulting in a decrease in Seebeck coefficient and power factor at all copper loadings. We conclude that the observed changes in electrical and thermoelectric properties of the presented hybrid system are dominated by the effect of heterostructure growth.

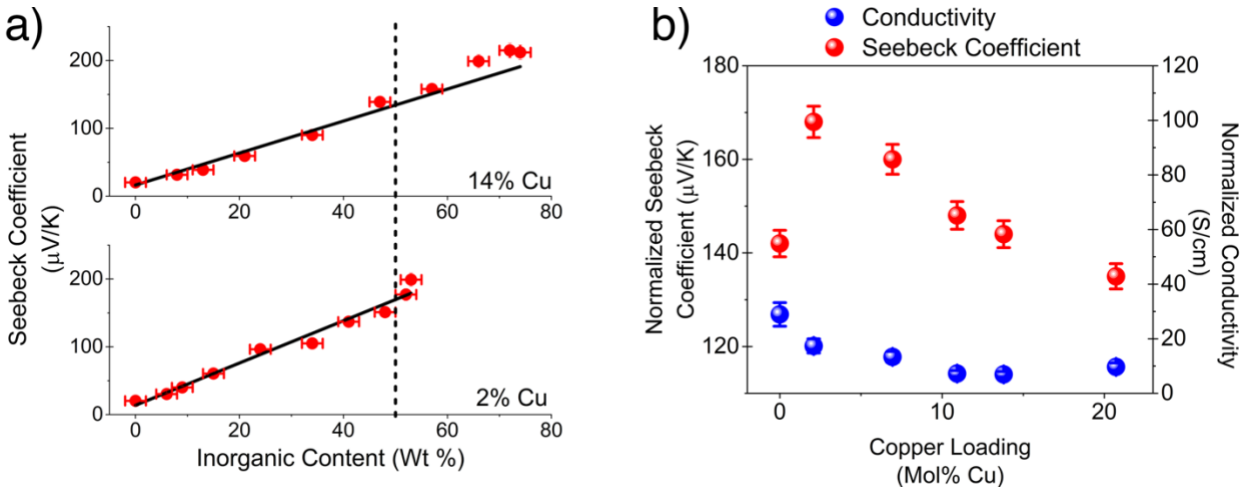

Figure 4.4 Normalization procedure for comparing Seebeck coefficient values across hybrid samples. (a) The Seebeck coefficients of two PEDOT:PSS-Te(Cu_x) NW systems, each with different Cu loading, vary as a function of inorganic content. A linear fit was performed on each to interpolate the data. The dotted line represents 50 wt% inorganic content for each system. The point where the dotted line intersects with the linear fit was taken to be the normalized Seebeck coefficient for each system at 50% inorganic-50% organic content. (b) Seebeck coefficients normalized to 50 wt% inorganic content demonstrate the same Seebeck coefficient enhancement seen in Figure 4.3, ruling out incorporation of more inorganic material as the mechanism underlying this trend.

The low-doping Seebeck coefficient enhancement was reproduced across five synthetic batches (each with typically 8-12 doping levels, 3 samples per doping level) using two different copper precursors. However, it was noticed that the samples measured in Figure 4.3 had an additional uncontrolled degree of freedom. Each sample had a slightly different amount of PEDOT:PSS polymer in the NW coating as measured by TGA. This effect can potentially lead to trivially enhanced thermopower in samples with larger amounts of the high-Seebeck coefficient component (Te) and less of the low-Seebeck coefficient component (PEDOT:PSS). To remove this compositional effect and isolate the effect of subphase growth on the performance of the samples, a normalization procedure was used. In this procedure, samples were prepared at each of six different extents of subphase growth. Each of these six were split into twelve sub-batches, and each sub-batch was diluted with a different amount of PEDOT:PSS. The Seebeck coefficient and electrical conductivity of each were measured at each point along this PEDOT:PSS ladder. By interpolation, the normalized thermoelectric performance of each sample at 50 wt% PEDOT:PSS – 50 wt% inorganic content was calculated. Two representative PEDOT:PSS ladders for Seebeck coefficient are shown in Figure 4.4 with the extracted normalized values indicated by the dotted line. After normalization of all data, it is clear that the trend depicted in Figure 4.3 is recovered, indicating that the performance enhancement is indeed a result of controlled subphase patterning within the hybrid NWs.

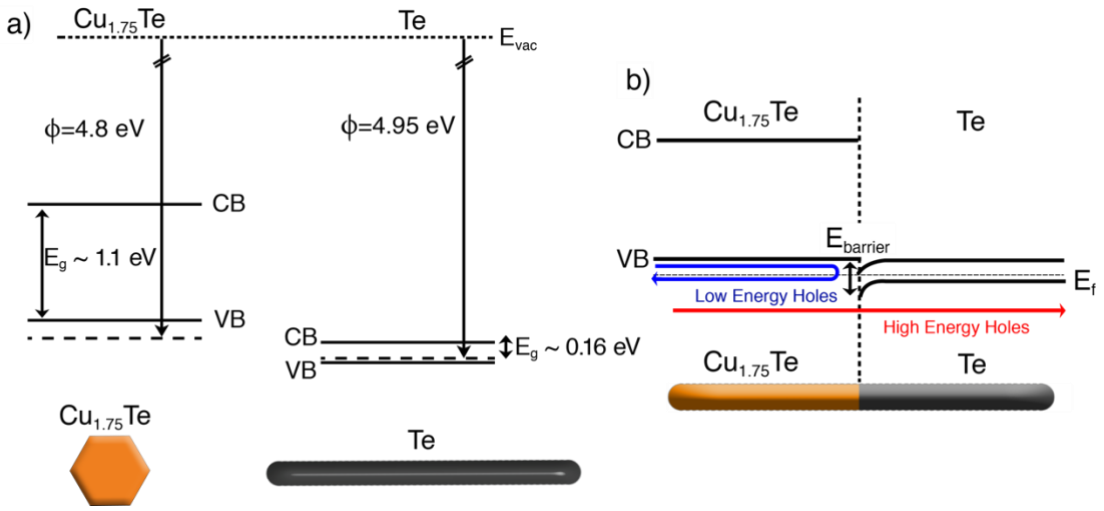

Figure 4.5 Band structure in Te-$Cu_{1.75}Te$ nanocomposites illustrates potential mechanism of energy-dependent scattering events. (a) Band structure of Te and $Cu_{1.75}Te$ before contact. (b) Equilibrium band alignment in Te-$Cu_{1.75}Te$ nanocomposites. Bending of the valence bands at the interface introduces an energetic barrier that preferentially scatters low energy holes. All work functions, and band gaps are bulk values[45,46,55]. Note that while this was our original hypothesis for the mechanism behind enhanced thermoelectric properties in this material system, later investigation revealed that the role of energy dependent scattering is minimal compared to other structural and energetic effects in the system (see Chapter 5).

4.4 Conclusions

In conclusion, controlled patterning of Cu-Te alloy subphases are demonstrated in hybrid PEDOT:PSS-Te NWs, representing the first alloy patterning of hybrid thermoelectric materials to our knowledge. This technique represents a new knob for hybrid materials design — fine-tuning the energy landscape for carriers — and has been used here in an attempt to modulate carrier scattering through regulated formation of alloy-semimetal interfaces. Specifically, polycrystalline $Cu_{1.75}Te$ domains were observed, causing a simultaneous morphological transition from straight to bent nanowires via growth of structurally misaligned crystal domains. A full range of alloy phase patterning is demonstrated, from minor subphase formation to complete conversion of the nanowires. After optimization of PEDOT:PSS loading, up to 22% enhancement of the power factor is observed. Note that, in complex hybrid systems, the power factor can be additionally enhanced via optimization of many parameters, in this case including nanowire aspect ratio, doping or dedoping of the PEDOT:PSS layer, and doping of the semimetal nanowire core.[18,22,51] The work reported here demonstrates power factor enhancement in a relevant, high-performing hybrid material system using a unique synthetic technique. However, it does not include these additional layers of optimization, so it is expected that the power factors reported here could be further improved using these well-known techniques. Moreover, while we apply this technique to our model PEDOT:PSS-Te system, the approach is highly general and can easily be adapted to realize power factor enhancements in other high-performing material systems. In the future, we hope to explore other metal-Te alloy phases to systematically probe the effect of energetic and structural matching across interfaces on carrier scattering and dynamics. This technique provides an exciting

new platform for rational design of solution-processable thermoelectrics, enabling investigation of how interfacial properties affect carrier dynamics in complex systems. This is a topic of fundamental importance, especially for nanostructured solid-state devices such as thermoelectrics, photovoltaics, or optoelectronics, in which carrier scattering mechanisms have huge implications for device performance. Moreover, this material system provides an ideal platform for systematic investigation of the physical mechanism underlying enhanced thermoelectric transport in hybrid organic-inorganic materials, which we pursue further in Chapter 5.

4.5 Experimental

4.5.1 Materials Synthesis

L-ascorbic acid ($C_6H_8O_6$), sodium tellurite (Na_2TeO_3), copper(II) nitrate hemipentahydrate ($Cu(NO_3)_2 \bullet 2.5H_2O$) , and copper(I) chloride ($CuCl_2$) were purchased from Sigma Aldrich. Poly (3,4-ethylenedioxythiophene):poly(styrene sulfonate) (PEDOT:PSS - Clevios PH1000) was purchased from Heraeus. Acetone (J.T.Baker®), dichloromethane (CH_2Cl_2 – BDH®), isopropyl alcohol (C_3H_8O – ACS Grade), and nitric acid (HNO_3 – BDH®) were purchased from VWR International. All chemicals were used as delivered without further purification.

Large-scale synthesis of PEDOT:PSS-tellurium nanowires (PEDOT:PSS-Te NW) was performed by dissolving 56.8 mmol L-ascorbic acid in 450 mL of ultrapure water (deionized >18 MΩ-cm) in a round bottom flask. 10 mL of PEDOT:PSS was filtered through a 0.45 μm PVDF syringe filter into the flask and stirred vigorously for 5 minutes. 3.2 mmol sodium tellurite was separately dissolved in 50 mL deionized water and then injected into the stirring reaction flask (~510 mL total solution). The reaction was heated to 90°C and held at that temperature for 20 hours with continuous stirring.

After the reaction was complete, the mixture was cooled to room temperature and divided evenly into twelve flasks (sub-batches). To each flask was added a different amount of copper(II) nitrate hemipentahydrate to achieve targeted doping concentrations using a stock 10 mg/mL aqueous solution. Copper(I) chloride was tested as an alternative copper source and demonstrated identical behavior. The copper precursor was added in one to four cycles depending on the amount of copper required. Between each addition, each flask was stirred for 1 hour to allow for copper diffusion and subphase growth. Then, an additional 1 mL of PEDOT:PSS was added to each flask to restabilize the NW. Purification was performed by centrifuging the nanowire (NW) solutions at 9000 rpm for 45 minutes, then pouring off the supernatant and resuspending in ultrapure water. This procedure was performed 3 times, and NWs were finally resuspended in 2-4 mL water per sub-batch and stored for further use.

Dropcast films (typically 3-5 μm in thickness) on square glass substrates (9.5mm x 9.5mm - Thin Film Devices) were used for electrical/thermoelectric measurements, temperature dependent conductivity, X-ray diffraction, and X-ray photoelectron spectroscopy studies. The glass substrates were cleaned before use – typically the substrates were sonicated in water, acetone, and isopropanol for 15 minutes each, followed by nitrogen drying and UV-ozone treatment for at least 10 minutes. The substrates were placed on a large aluminum block acting as a thermal reservoir at 80°C, and 75 μL of NW solution (at concentrations varying between 20-50 mg/mL) were drop cast onto the substrates. Films were dried in this manner for 20-30 min.

4.5.2 Electrical and Thermoelectric Measurements

Gold contacts (100nm) were patterned onto each of the four corners of the dropcast films via thermal evaporation using a shadow mask to pattern the contacts. Both the shadow mask and resulting test devices are shown in Figure 4.6. Sheet resistance of each film was measured using Keithley 2400 Sourcemeters in 4-wire van-der-Pauw configuration. Film thickness was measured by scratching the film and measuring the step height with a Veeco Dektak 150 profilometer. Electrical conductivity was extracted from the sheet resistance and thickness measurements. Seebeck coefficient (thermopower) was measured using a homemade probe setup. Two Peltier devices (Ferrotec) were placed ~4mm apart and a single current was passed through them in opposite polarities. This caused one device to heat and the other to cool approximately the same amount relative to room temperature. The sample was placed across these two devices such that a thermal gradient was established (thermal paste was used to ensure thermal contact – Wakefield Thermal S3 Solutions), and the resulting open circuit voltage was measured using an Agilent 34401 multimeter. The temperature gradient was measured using two T-type thermocouples mounted in micromanipulators. The magnitude of the temperature gradient is directly correlated to the amount of current driven through the Peltier devices. Typically, five different gradients were established (allowed to equilibrate for 200 sec between temperature changes), with 10 voltage measurements taken and averaged at each ΔT. All samples exhibited linear variation of open circuit voltage with ΔT ; this trend was used to extract Seebeck coefficient values. Data for both electrical conductivity and Seebeck coefficient were acquired using homemade Labview programs. Ohmic contacts were confirmed before all room temperature and temperature dependent conductivity studies - a representative I-V curve is shown in Figure 4.15.

4.5.3 Characterization

Scanning electron microscopy (SEM), energy dispersive x-ray spectroscopy (EDS), transmission electron microscopy (TEM), X-ray diffraction (XRD), thermo-gravimetric analysis (TGA), inductively coupled plasma optical emission spectroscopy (ICP-OES), x-ray photoelectron spectroscopy (XPS), and x-ray absorption spectroscopy (XAS) with a synchrotron radiation source were used to characterize the size, shape, structure, composition, and optical properties of the nanowires.

Scanning Electron Microscopy and Energy Dispersive X-Ray Spectroscopy: SEM images were recorded and EDAX analyses were performed on a Zeiss Gemini Ultra-55 Analytical Field Emission Scanning Electron Microscope using beam energy of 5 kV for imaging and 17 kV for elemental analysis and an In-Lens detector. Representative SEM images and EDAX spectrum are given in Figure 4.7.

Transmission Electron Microscopy: TEM images were recorded using a Zeiss Libra TEM and JEOL 2100-F Field-Emission Analytical TEM at 120 and 200 kV respectively. TEM samples were prepared by placing a TEM grid (400-mesh Cu or Ni on holey carbon – Ted Pella 01824) on a filter paper taped flat to a large aluminum block at 140°C. A single drop of dilute nanowire solution was deposited onto the grid and the water was allowed to evaporate for 5 min. EDS mapping was carried out on the JEOL microscope under STEM mode (Figure 4.8).

X-Ray Diffraction: A Bruker AXS D8 Discover GADDS XRD micro-diffractometer was utilized to collect wide-angle spectra using a Co-Kα source at 0.179 nm wavelength. Figure 4.9 shows representative spectra for a PEDOT:PSS-Te NW sample with no Cu and one after full conversion to PEDOT:PSS-$Cu_{1.75}$Te NW.

Thermogravimetric Analysis: A TA Instruments Q5000IR TGA was used to quantify organic-inorganic composition of each sample. 7-10 mg of each sample was ramped to 600°C at a scan rate of 10°C/min and held there for 45 min to ensure complete decomposition and removal of any PEDOT:PSS. The weight lost was assumed to be the organic content of the hybrid, and the remaining weight was taken to be the inorganic content. Figure 4.10 depicts a typical TGA scan.

Inductively Coupled Plasma Optical Emission Spectroscopy: Varian ICP-OES 720 Series was used for elemental analysis of all samples. After purification of each NW sample, a small amount (1-5 mg) was digested using concentrated nitric acid for 72 hours. Samples were then diluted to 2 wt% nitric acid and run, along with 6 standards each for Cu and Te. For compositional quantification, multiple readings were taken at each of three different characteristic emission wavelengths and averaged. This allows for high accuracy determination of relative amounts of Cu and Te in each sample. Table S1 shows data from typical ICP elemental analysis.

X-Ray Photoelectron Spectroscopy: XPS was used to identify present Cu and Te valence states in samples of varying Cu loading. A PHI 5400 X-ray Photoelectron Spectroscopy (XPS) System with a conventional Al Kα source operated at 350 W was used for this purpose. Pass energy of 20 eV was used for narrow scan spectra, corresponding to an energy resolution of ~700 meV. Figure 4.11 depicts representative XPS spectra of PEDOT:PSS-Te nanowires and PEDOT:PSS-Te(Cu_x) nanowires with high Cu loading, with the inset emphasizing the growth of Te^{+4} peaks in the high Cu loading regime.

X-Ray Absorption Spectroscopy with Synchrotron Radiation Source: XAS was also used to probe the oxidation states of Cu present in samples with varying Cu loading. For this analysis, 3rd generation synchrotron radiation was utilized at Beamline 8.0.1 of the Advanced Light Source (ALS) in Berkeley, CA. This undulator Beamline provides intensive soft x-rays monochromated by three spherical gratings. Cu L-edge XAS was used in this study, probing the excitation of Cu 2p electrons to empty 3d-derived states. Cu XAS was collected in Total Electron Yield (TEY) and Total Fluorescence Yield (TFY) mode simultaneously. The energy resolution at the Cu L-edge is about 0.2 eV. All the spectra were calibrated via measurement of Cu-foil before and after each experiment. Experimentation was performed under Ultra High Vacuum (UHV) environment at most $3*10^{-9}$ torr. Figure 4.12 shows CU XAS for several samples with different Cu loading.

4.5.4 PEDOT-PSS-Copper Interaction

To probe the interaction between Cu ions and PEDOT:PSS, thin film devices were fabricated with PEDOT:PSS doped with varying amounts of Cu ions and no Te present. Five dispersions of PEDOT:PSS were prepared as usual, and varying amounts of copper nitrate hemipentahydrate were added. After 30 min of stirring, thin film devices were fabricated, and electrical and thermoelectric properties were characterized via the methods detailed above. The results are shown in Figure 4.14. At low copper loading, a modest increase in electrical conductivity is observed (up to 5.4 S/cm), but this is associated with a drop in Seebeck coefficient, and no power factor

enhancement is observed. In the hybrid system, the opposite trend is observed; at low copper loading, the Seebeck coefficient is enhanced at the cost of a modest drop in electrical conductivity. Additionally, at high copper loading, both electrical and thermoelectric properties worsen, which is again a trend not observed in the hybrid system. We conclude that the changes in electrical and thermoelectric properties observed in the hybrid system are dominated by heterostructure growth, and not by interactions between Cu ions and PEDOT:PSS.

4.5.5 Error Analysis

All error bars, unless otherwise specified, are sample standard deviations, representing the variation in measurements across replicates.

4.6 Acknowledgements

We gratefully acknowledge support through the Department of Energy BES-LBL Thermoelectrics Program. This work was performed at the Molecular Foundry and Advanced Light Source, Lawrence Berkeley National Laboratory, and was supported by the Office of Science, Office of Basic Energy Sciences, Scientific User Facilities Division of the U.S. Department of Energy under Contract No. DE-AC02-05CH11231.

4.7 Supporting Information

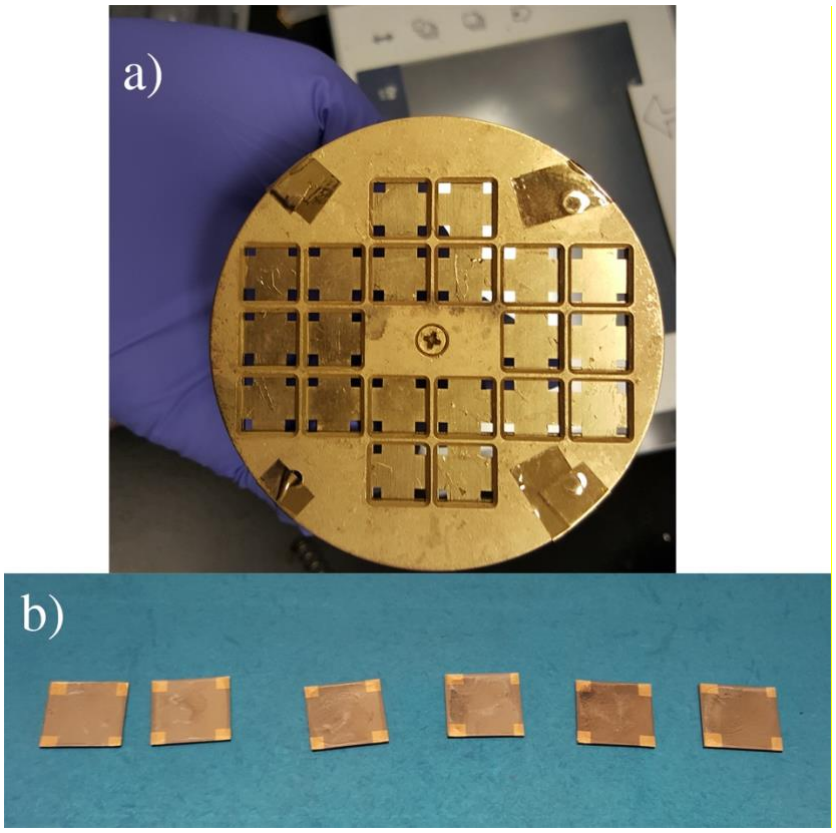

Figure 4.6 (a) Shadow mask used during thermal evaporation to deposit corner contacts of 100nm Au on each testing device. (b) Test devices prepared for four-point probe electrical conductivity and Seebeck characterization. Each test device measures 9.5mm x 9.5mm.

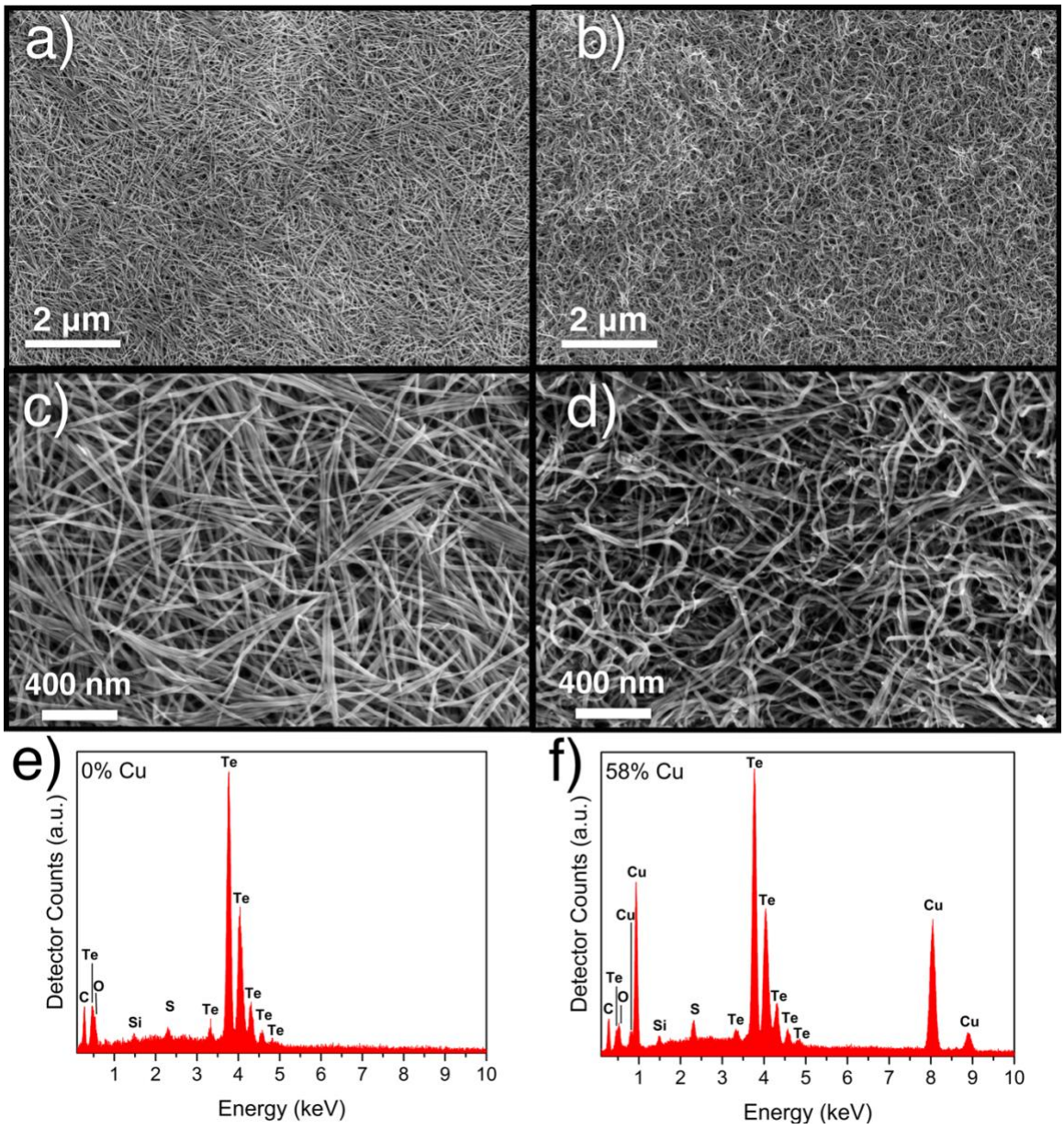

Figure 4.7 SEM and EDS spectra. Low magnification SEM images (10kx) of (a) PEDOT:PSS-Te NWs (0% Cu) and (b) PEDOT:PSS-$Cu_{1.75}Te$ (58 mol% Cu) NWs depict long range morphology of dropcast films. High magnification SEM images (40kx) illustrate the transition from (c) rigid (0% Cu) to (d) bent nanowires (58% Cu). EDS spectra for (e) 0% Cu and (f) 58% Cu nanowire films confirm growth of Cu-rich subphases.

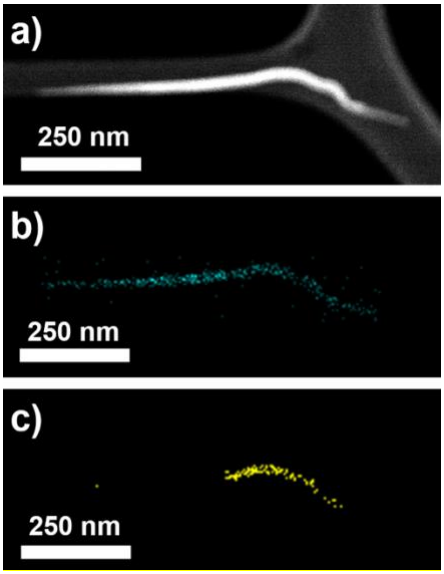

Figure 4.8 STEM-EDS mapping of a representative PEDOT:PSS-Te(Cux) NW. (a) HAADF image (b) Te elemental map shows Te present throughout the wire. (c) Cu elemental map indicates concentration in the kinked wire regions.

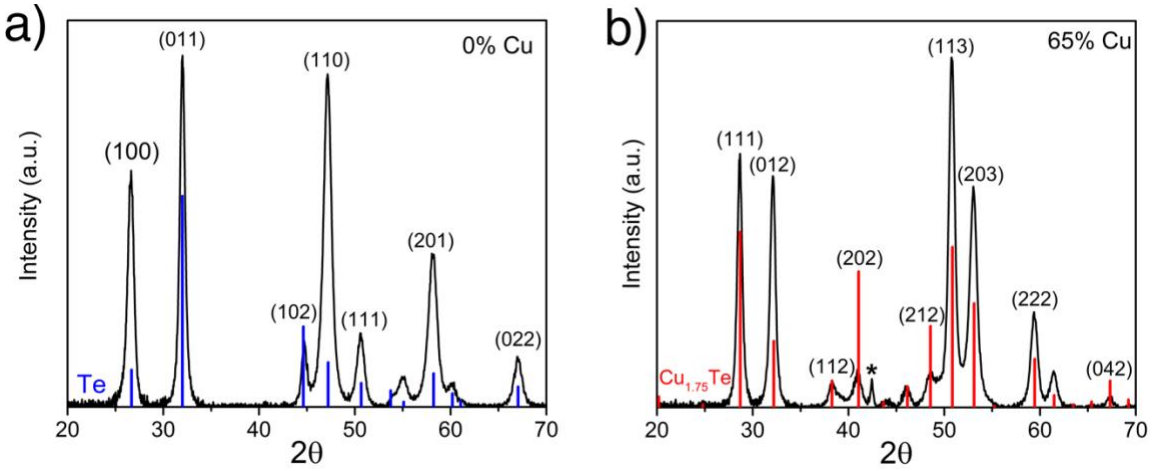

Figure 4.9 Representative XRD spectra for no Cu and high Cu loading samples. (a) PEDOT:PSS-Te film (0% Cu) can be indexed to metallic Te (ICDD PDF-4 #04-016-1605). (b) High Cu loading samples can be indexed to $Cu_{1.75}Te$ (ICDD PDF-4 # 04-007-0008). Minor products include CuO (ICDD – PDF-4 #04-014-5856), Cu_2O (ICDD PDF-4 #04-001-8705) and $CuTeO_3$ (ICDD PDF-4 #04-001-8705).

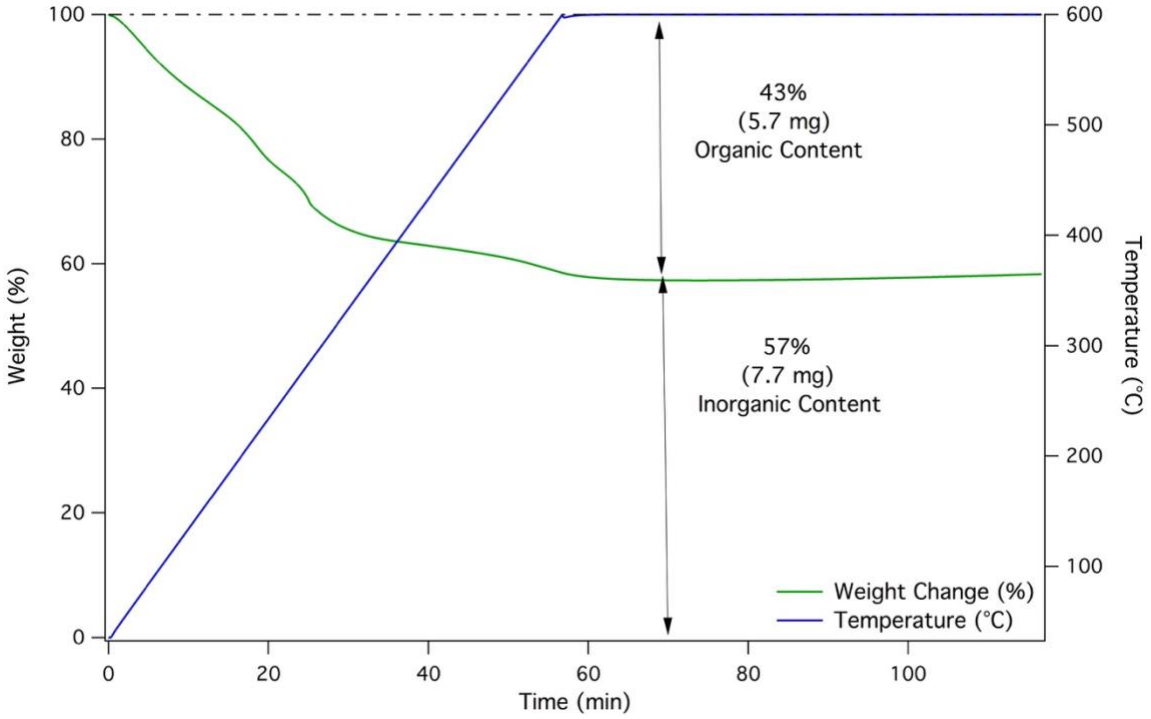

Figure 4.10 Representative TGA data depicting the decomposition of PEDOT:PSS during a heat ramp to 600°C. The plateau in weight change indicates that all the organic content has been removed, and the inorganic phase is left behind.

Table 4.1 ICP analysis. Three readings are taken per element and the average is used to calculate the ratio of Cu to Te in each PEDOT:PSS-Te(Cu_x) sample. In this case, ICP analysis indicates 58 mol% Cu loading. Note, here the units of ppm are equivalent to mg/L.

	Cu (ppm)	**S (ppm)**	**Te (ppm)**
1	40.7 (@ 213 nm)	0.208 (@ 181 nm)	59.4 (@ 182 nm)
2	38.9 (@ 324 nm)	0.174 (@ 182 nm)	58.0 (@ 214 nm)
3	39.0 (@ 327 nm)	0.268 (@ 183 nm)	57.6 (@ 239 nm)
Average	**39.5 ± 0.9**	**0.217 ± 0.04**	**58.3 ± 0.4**

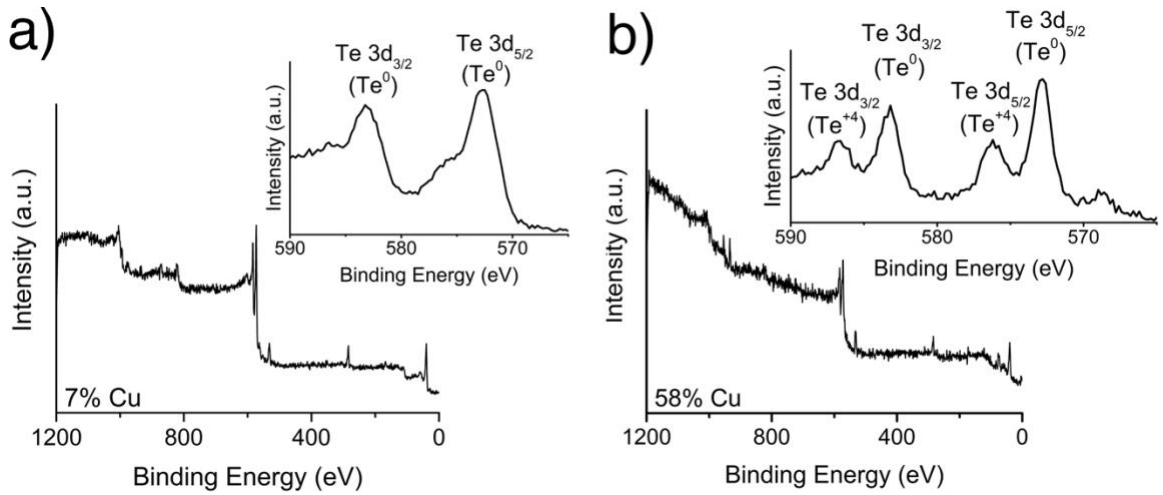

Figure 4.11 XPS spectra of PEDOT:PSS-Te(Cu_x) NWs with low and high copper loading. Each inset magnifies the region featuring a characteristic Te 3d emission. (a) Samples with low copper loading feature peaks representative of metallic Te^0. (b) Samples with high copper loading also show growth of Te^{+4} species. This further supports the hypothesis that oxides such as $CuTeO_3$ form in the limit of full conversion to $Cu_{1.75}Te$ nanowires.

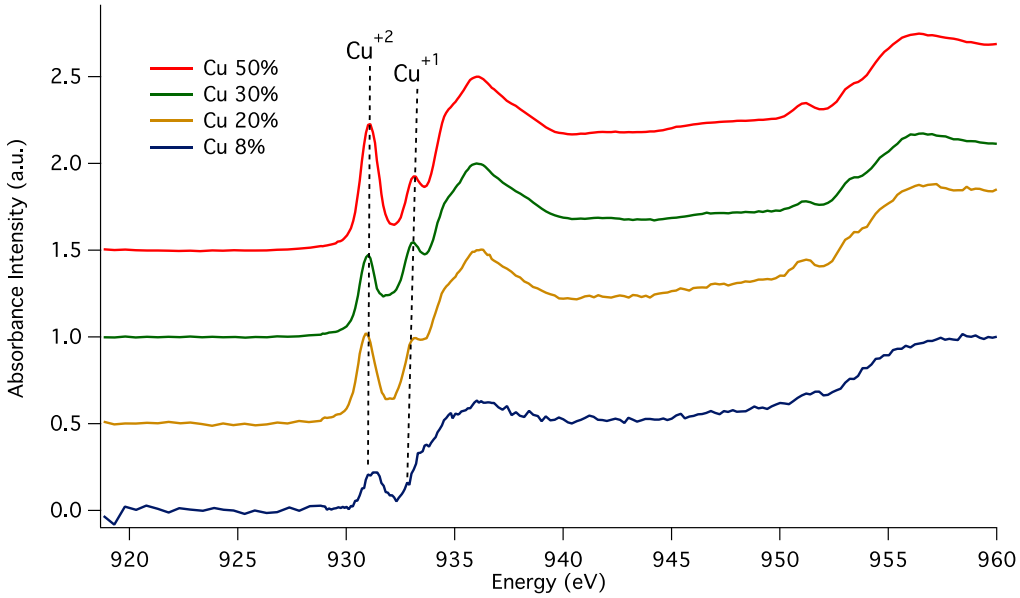

Figure 4.12 Cu $L_{2,3}$-edge XAS from a synchrotron radiation source for PEDOT:PSS-Te(Cu_x) samples of varying Cu loading depicts characteristic $2p^{3/2}$ transitions for both Cu^{+2} and Cu^{+1} species. Despite the relative size of the peaks, these spectra are consistent with previously reported spectra for materials with primarily Cu^{+1} species and only small amounts of Cu^{+2} as an impurity, due to the much larger absorption cross-section for Cu^{+2} compared to that of Cu^{+1} species. The growth of the Cu^{+1} peak as copper loading increases is consistent with growth of $Cu_{1.75}Te$ subphases. Cu^{+2} species are present as impurities at all levels of copper loading, in the form of CuO oxides. Spectra are offset vertically for ease of comparison.

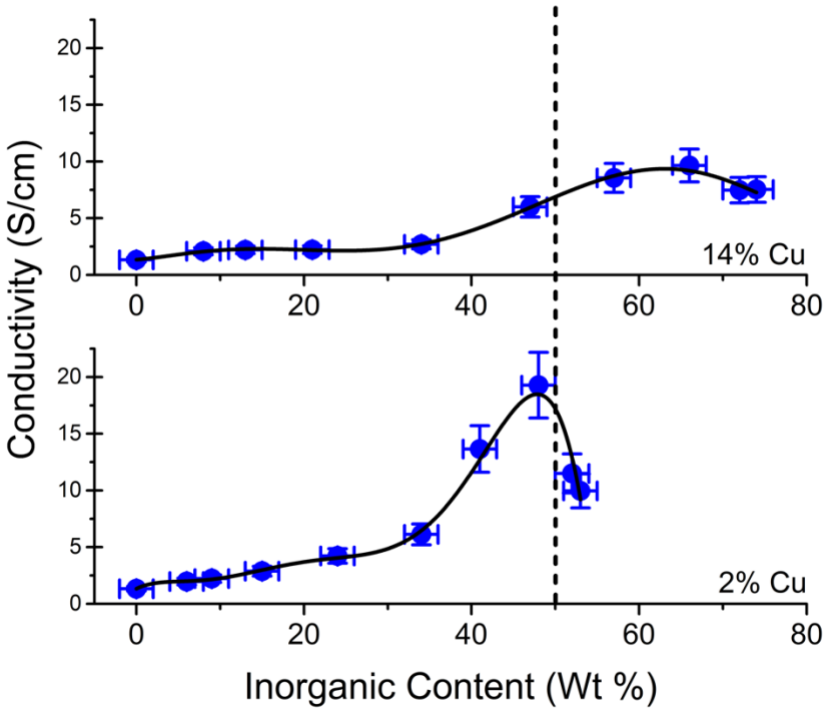

Figure 4.13 Normalization of electrical conductivity for samples with different extents of subphase growth. A sixth order polynomial fit was used purely for close interpolation of the data. The dotted line represents 50 wt% inorganic content for each system. The point where the dotted line intersects with the polynomial fit was taken to be the normalized electrical conductivity for each system at 50% inorganic-50% organic content.

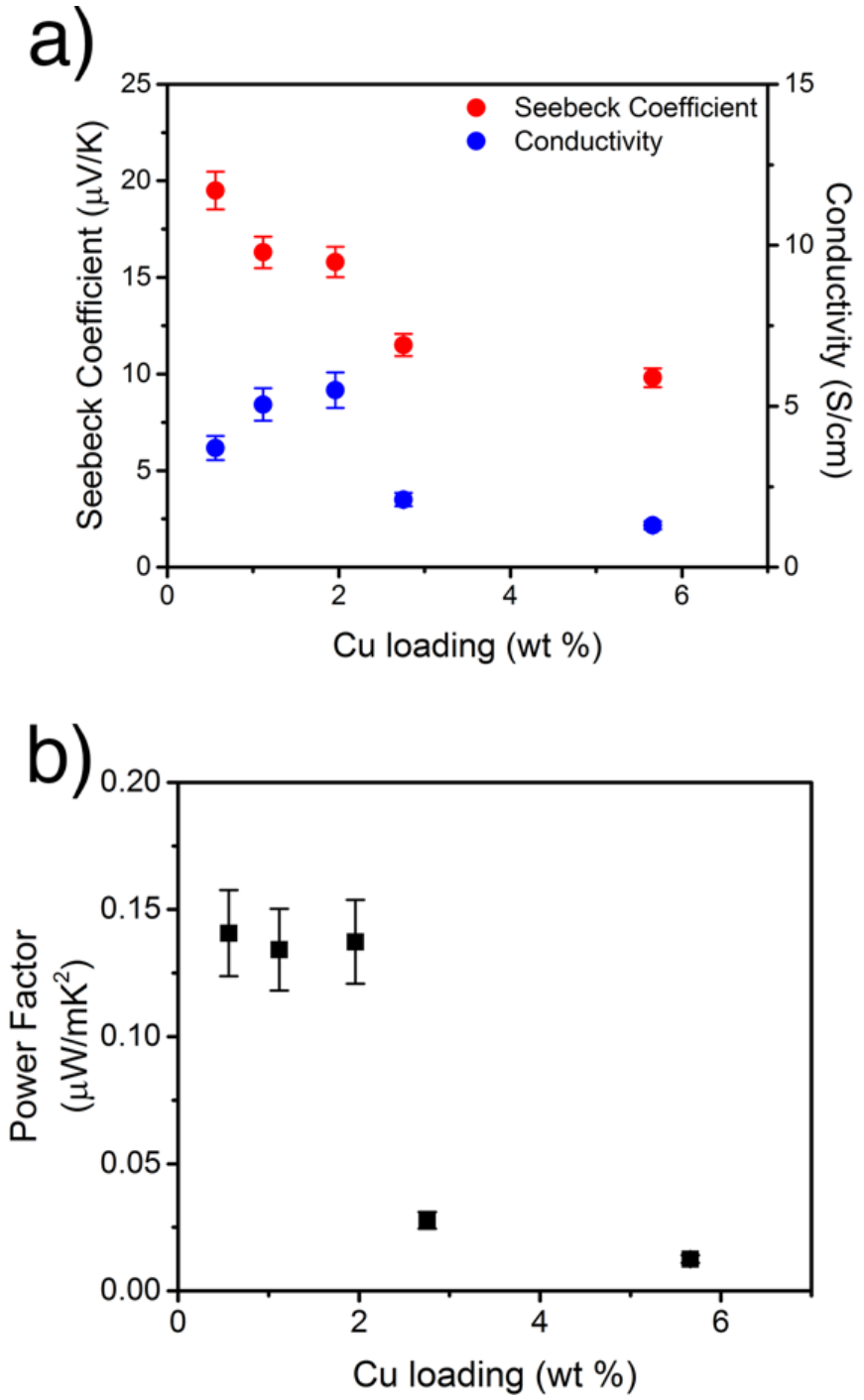

Figure 4.14 Electrical and thermoelectric characterization of PEDOT:PSS films doped with Cu in the absence of Te. (a) The Seebeck coefficient is negatively affected at all Cu loading levels, while the electrical conductivity is modestly improved in the presence of small amounts of copper ions, a trend that is not observed in the PEDOT:PSS-Te(Cu_x) system. (b) No power factor enhancement is observed. Note that, above 6 wt% Cu loading, the PEDOT:PSS becomes highly viscous and film formation is no longer possible.

Chapter 5. Polymer morphology and interfacial charge transfer dominate over energy-dependent scattering in organic-inorganic thermoelectrics

Adapted from "Polymer morphology and interfacial charge transfer dominate over energy-dependent scattering in organic-inorganic thermoelectrics," P Kumar[#], EW Zaia[#], E Yildirim, DVM Repaka, SW Yang, JJ Urban[*], K Hippalgaonkar[*], *Nature Communications,* 2018, 9.1, 5347 (DOI: 10.1038/s41467-018-07435-z) with permission of the authors. *Reproduced with permission of Nature Communications*. Note that additional supplementary information (excluded from this dissertation for readability) can be found with the original published material.

5.1 Abstract

Hybrid (organic-inorganic) materials have emerged as a promising class of thermoelectric materials, achieving power factors ($S^2\sigma$) exceeding those of either constituent. The mechanism of this enhancement is still under debate and pinpointing the underlying physics has proven difficult. In this work, we combine transport measurements with theoretical simulations and first principles calculations on a prototypical PEDOT:PSS-Te(Cu_x) nanowire hybrid material system to understand the effect of templating and charge redistribution on the thermoelectric performance. Further, we apply the recently developed Kang-Snyder charge transport model to show that scattering of holes in the hybrid system, defined by the energy-dependent scattering parameter, remains the same as in the host polymer matrix; performance is instead dictated by polymer morphology manifested in an energy-independent transport coefficient. We build upon this language to explain thermoelectric behavior in a variety of PEDOT and P3HT based hybrids acting as a guide for future work in multiphase materials.

5.2 Introduction

New, emerging classes of organic semiconductors, polymers, and organic-inorganic composite materials have penetrated into areas of optoelectronics previously dominated by inorganic materials. Organic light emitting diodes have reached wide commercial availability, and organic-inorganic hybrid photovoltaics have shown an unparalleled rate of efficiency improvement.[148,149] Such solution-processable materials avoid the need for energy-intensive fabrication steps and instead utilize inexpensive, scalable, roll-to-roll techniques.[150] In particular, progress in this area has been driven by the development of materials based on poly(3,4-ethylenedioxythiophene), (PEDOT).[19,20] PEDOT-based materials have demonstrated remarkably high conductivities, outperforming all other conductive polymer classes and driving tremendous interest in the use of soft materials in flexible electronics and thermoelectrics.[151–153] Soft thermoelectric materials can realize flexible energy generation or heating-cooling devices with conformal geometries, enabling a new portfolio of applications for thermoelectric technologies.[150] Of particular interest are hybrid soft nanomaterials – an emerging material class that combines organic and inorganic components to yield fundamentally new properties.[24,25,29,154]

In hybrid systems, recent studies have focused on the use of strategies such as interfacial transport, structural/morphological effects, and modifications to the energy dependence of carrier scattering to improve electronic and thermoelectric performance.[115,155,156] However, it has proven difficult to establish the fundamental physics driving these performance enhancements. The most challenging of the proposed design strategies to evaluate is the role of energy dependent scattering, a phenomenon frequently and contentiously implicated in high performing thermoelectric materials.[82,157] More generally, advanced design of high performing soft thermoelectric materials has been stymied by the fact that transport in these systems is complex and resists description by a unified transport model. Development of next generation soft hybrid materials and modules requires improved understanding of the carrier transport physics in complex multiphase systems.

Kang and Snyder recently proposed a generalized charge transport model (henceforth referred to as Kang-Snyder Model) for conducting polymers, which marks a significant advance in the theoretical tools available to the soft thermoelectrics field.[63,64] In this model, the thermoelectric transport of conducting polymers has been modeled using energy independent parameter, σ_{E0} and energy dependent parameter '*s*' over a large range of conductivity. In addition, vital to the theory developed is the energy-dependent scattering parameter *s*, which distinguishes the majority of conducting polymers (s = 3) from the class of PEDOT-based materials (s = 1). However, these two parameters are difficult to uniquely measure. Additionally, this first report did not cover hybrid organic-inorganic materials, which creates an important gap in the relevant material classes that requires further investigation.

Here, we apply this Kang-Snyder framework to a set of hybrid thermoelectric materials to identify the physics responsible for favorable thermoelectric transport in these systems. We begin with a model system of tellurium nanowires coated with PEDOT:PSS. This system was chosen due to its high thermoelectric performance (ZT ~ 0.1 at room temperature), facile solution-based synthesis, and well-defined single crystalline inorganic phase.[24,25,115] Further, we have previously shown that this material can be easily converted to tellurium-alloy heterowires.[25] For example, using copper as the alloying material results in PEDOT:PSS-Te-$Cu_{1.75}$Te heteronanowires. It has been observed that formation of small amounts of alloy subphases yields improvement in the thermoelectric performance of these materials. However, whether the observed transport properties are dictated by the organic phase, inorganic phase, or interfacial properties is an open question. Here, we use a full suite of experiments, transport modeling, molecular dynamics, and first principles calculations to describe the exact nature of the organic-inorganic interactions. We also show that the Kang-Snyder framework can be applied effectively to hybrid systems, extending the theoretical tools available to experimentalists. In this way, we seek to fill an important gap in knowledge in this body of literature and inform the direction of future experimental work.

5.3 Results and Discussion

5.3.1 Synthesis and Structure

Synthesis of tellurium nanowires coated in PEDOT:PSS (PEDOT:PSS-Te NWs) and conversion to Te-$Cu_{1.75}$Te heterostructures (PEDOT:PSS-Te(Cu_x) NWs) were performed as previously reported (Details in Methods).[24,25] The synthesis of the tellurium nanowires is performed in the presence of PEDOT:PSS, which has been posited to act both as a stabilizing ligand and as a structure-directing agent (Figure 5.1a).[24,115] Te-$Cu_{1.75}$Te heterowires have a curved appearance as

a result of alloy domains appearing at ‘kinked’ portions of the wires. Representative high-resolution transmission electron micrographs (HR-TEM) of the Te and $Cu_{1.75}Te$ domains (Figure 5.1c,d) show the highly crystalline inorganic phases and the different local morphologies. Note that the additional copper loading increases the total number of ‘kinked’ portions (Figure 5.1b), while each ‘kinked’ portion is stoichiometrically stable and close to the $Cu_{1.75}Te$ phase.

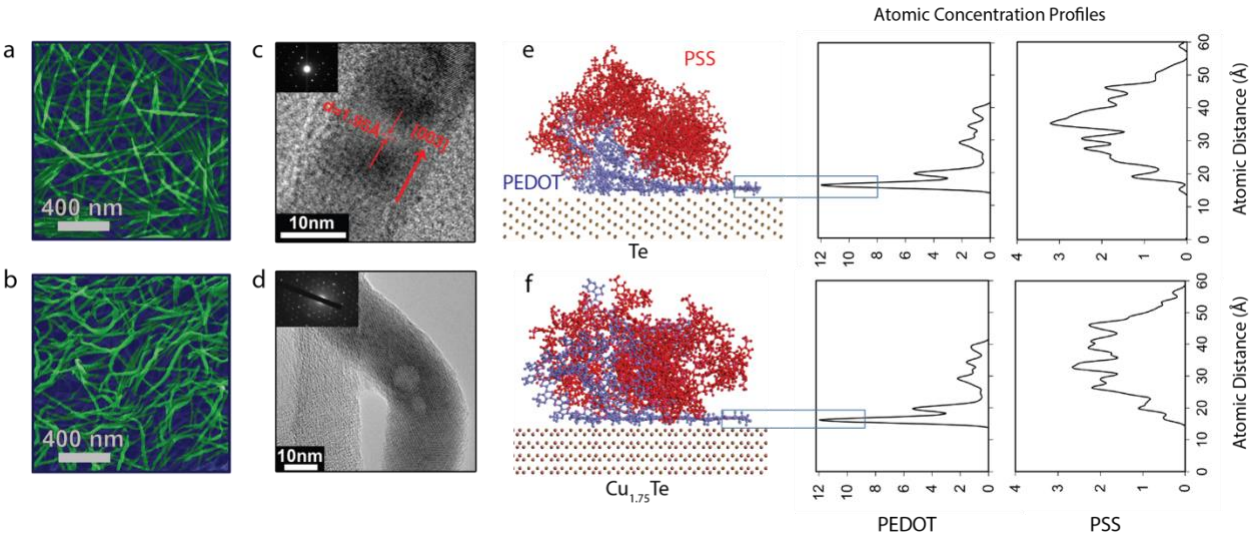

Figure 5.1 Morphology of hybrids and alignment of PEDOT:PSS at the inorganic interface (a,b) False-color scanning electron microscope (SEM) images of (a) PEDOT:PSS-Te and (b) PEDOT:PSS-$Cu_{1.75}Te$ films illustrate the overall morphology of the hybrid films – inorganic nanowires in a PEDOT:PSS matrix. The green color shows the surface nanowires and blue illustrates the 3D plane underneath, where the PEDOT:PSS polymer matrix is transparent (and hence invisible) in the SEM. (c,d) Representative high-resolution transmission electron microscopy (HR-TEM) images of (c) straight Te domains and (d) kinked $Cu_{1.75}Te$ alloy domains confirm the identity and crystallinity of these two phases. The insets show selected area electron diffraction (SAED) patterns consistent with the identified crystal structures. (e,f) MD simulations elucidate the polymer morphology and alignment at the organic-inorganic interface. Here, the final polymer structures are depicted after simulated annealing of five chains of $EDOT_{18}$ and SS_{36} on (e) Te and (f) $Cu_{1.75}Te$ surfaces, both accompanied by respective atomic concentration profiles. The polymer concentration profiles are tracked using the atomic concentration of S in either PEDOT or PSS. There is a high concentration of S atoms in PEDOT observed at 3-5 Å from the nanowire surfaces, suggestive of highly ordered and aligned PEDOT chains at the organic-inorganic interface. Similar structures and concentration profiles were observed for both Te nanowires (NW) and $Cu_{1.75}Te$ heteronanowires, however unlike the Te surface, though alignment occurs, self-assembly of chains is reduced on the kinked $Cu_{1.75}Te$ surface.

5.3.2 Morphology and Interactions

To probe the organic-inorganic interactions involved in carrier transport in this material system, we perform extensive Molecular Dynamics (MD) simulations and Density Functional Theory (DFT) calculations. Specifically, MD simulations uncover detailed information about adhesion and polymer morphology/structural changes in the vicinity of the Te nanowire and $Cu_{1.75}Te$ hetero-nanowire surfaces. These analyses strongly suggest that structural templating effects occur during synthesis. Templating effects have been widely hypothesized to occur in such processes, but direct evidence has been lacking so far.[115] As a complement to our structural analyses, DFT is used to investigate the electronic effects that arise at the organic-inorganic interface. In particular, we estimate the amount of charge transfer between the organic and inorganic phases and probe the evolution of the electronic Density of States (DOS).

5.3.3 Molecular dynamics (MD) simulations of the organic-inorganic interface

The MD simulations (details in Methods and Supplementary Note 1) reveal self-alignment of PEDOT chains at the organic-inorganic interface for both Te and $Cu_{1.75}Te$ NW surfaces. This self-alignment is only observed for the PEDOT chains in the vicinity of Te and the $Cu_{1.75}Te$ surfaces, while the PSS remains unaligned. This phenomenon is clearly distinguished by comparing the structures and concentration profiles before and after simulated annealing (Figure 5.1e-f). Further annealing simulations on PEDOT:PSS, pristine PEDOT and pristine PSS suggest that only first few layers of PEDOT moieties tend to align in a planar orientation on the inorganic surfaces (detailed discussion in Supplementary Note 1, see also Supplementary Figures 5.1-5.2). $Te/Cu_{1.75}Te$ nanowires are coated with ~2nm thin PEDOT layer, which also corresponds to only a few layers. It is also determined that the self-assembly and percolation of PEDOT chains are reduced on the kinked $Cu_{1.75}Te$ surface.

To investigate the driving force for PEDOT alignment (and lack thereof for PSS) on the inorganic surface, the interfacial PEDOT-inorganic and PSS-inorganic interaction energies were calculated and compared. Two cells were equilibrated with six π-stacked PEDOT and three PSS oligomers. In one of the cells, PEDOT chains are placed at the organic-inorganic interface; in the other, PSS chains. The polymer-Te interaction energy is determined to be -423 kcal/mol for PEDOT layers on the Te NW surface and -192 kcal/mol for the PSS oligomer on the Te NW surface. This result indicates a thermodynamic driving force for self-assembly of PEDOT over PSS on the nanowire surface, consistent with the structures observed in the MD simulations described previously. The interaction of the same systems with a $Cu_{1.75}Te$ NW is about two times stronger calculated as -792 and -388 kcal/mol for PEDOT layers on the NW surface and PSS layers on the NW surface respectively.

Simulated annealing reveal that PEDOT chains tend to align in a planar configuration on both Te and $Cu_{1.75}Te$ surfaces, although self-assembly is observed on the Te surface and not the $Cu_{1.75}Te$. We attribute this phenomenon to stronger interaction between PEDOT and the $Cu_{1.75}Te$ surface, resulting in reduced movement of the PEDOT chains on the $Cu_{1.75}Te$ surface.

5.3.4 Density functional theory calculations probe interactions at the interface

To complement our understanding of polymer templating on the inorganic NW surfaces, Density Functional Theory (DFT) was used to calculate adsorption energies of PEDOT/PSS on these surfaces. Here, we consider a charged polaronic PEDOT hexamer $(EDOT_6)^{+2}$ and deprotonated PSS oligomer $(SS_6)^{-2}$ in a planar configuration close to the inorganic surface, as is predicted from MD simulations (Supplementary Note 2). At the Te NW-organic interface, adsorption energies of -0.42 eV and -0.31 eV per monomer were obtained for charged PEDOT and PSS, respectively, consistent with MD results that the Te surface is primarily occupied by adsorbed, aligned PEDOT. On the other hand, the PEDOT-$Cu_{1.75}Te$ adsorption energy is -0.56 eV, indicating an even stronger interaction.

Since MD and DFT both demonstrate the importance of the PEDOT-inorganic interaction at the interface in this system, further calculations were performed to determine the density of states and charge density difference at this interface. Figure 5.2a depicts the calculated charge density difference between $(EDOT_6)^{+2}$ and the Te surface, where a decrease in the electron density is represented in blue and electron density enrichment in red. Furthermore, using these charge density differences, charge transfer rates were extracted, yielding important insight into the electronic effects occurring at the organic-inorganic interface.

The maximum charge transfer rates from the inorganic surface to the first layer of (neutral) PEDOT chains on the surface were determined to be -0.078 and -0.144 for Te and $Cu_{1.75}Te$, respectively. Charge transfer rates are higher for the charged $(EDOT_6)^{+2}$ bipolaron, calculated to be -0.186 and -0.239 for Te and $Cu_{1.75}Te$, respectively. Note that a negative quantity here represents electron transfer from the inorganic surface to the organic PEDOT chains (i.e. hole transfer from the organic PEDOT chain to the inorganic surface). In every case, this charge transfer provides a de-doping effect of holes in the p-type PEDOT chains, which plays a key role in understanding the thermoelectric trends in these hybrid systems (Table 5.1). This de-doping effect is stronger for the doped PEDOT bipolaron compared to pristine PEDOT chains and also stronger for PEDOT on the $Cu_{1.75}Te$ surface compared to PEDOT on the Te surface. The charge transfer and de-doping effect is only observed for the first two layer of PEDOT chains and vanished for higher distances.

Table 5.1 Interfacial charge transfer calculations. De-doping level of neutral and doped PEDOT hexamer by Te and $Cu_{1.75}Te$ surfaces for the optimized structures.

	De-doping effect* (electron/cm^3)
Neutral $PEDOT_6$ on Te	-6.19×10^{20} for 3.6 Å (-1.27×10^{20} for 8 Å) (none > 15 Å)
$PEDOT_6^{+2}$ on Te	-1.56×10^{21}
Neutral $PEDOT_6$ on $Cu_{1.75}Te$	-1.14×10^{21}
$PEDOT_6^{+2}$ on $Cu_{1.75}Te$	-2.05×10^{21}

*PEDOT monomer volume 1.26×10^{-22} cm^3

As for the nature of the bonding between the organic and inorganic components, the weak charge density difference and atomic distances between organic and inorganic constituents, calculated to be between 3.6-4.0 Å, are analogous to other material systems that exhibit physical adsorption.[158] This conclusion is further corroborated by the Density of States (DOS) calculated for PEDOT, the Te surface, and the hybrid structure (Figure 5.2), which depicts a trivial change in DOS distribution between the individual and hybrid structures. Interestingly, there is indeed an intra-chain charge density difference within the PEDOT chain at a field isovalue of 0.005 electron/Å^3 (details in Methods). This result suggests electron density transfer from the PEDOT π orbitals to the σ orbitals, consistent with electron repulsion also known as a pillow effect [13,17,21,22], which occurs

when an organic molecule approaches a metal surface (Figure 5.2a-c).[82,115,159,160] Here, Pauli repulsion between the electron cloud of the nanowire surface and the PEDOT chain causes redistribution of electrons by repelling the electron cloud of the softer molecule (Supplementary Figure 5.8). As a result, the C-C bond distance between $(EDOT_6)^{+2}$ monomers is reduced from 1.42 to 1.40 Å when in proximity to the Te surface, characteristic of a benzoid to quinoid chain conformation change.[161] This conformational switch is also consistent with prior Terahertz spectroscopy studies that indicate charge-trapping near the polymer-Te nanowire surface.[76,162]

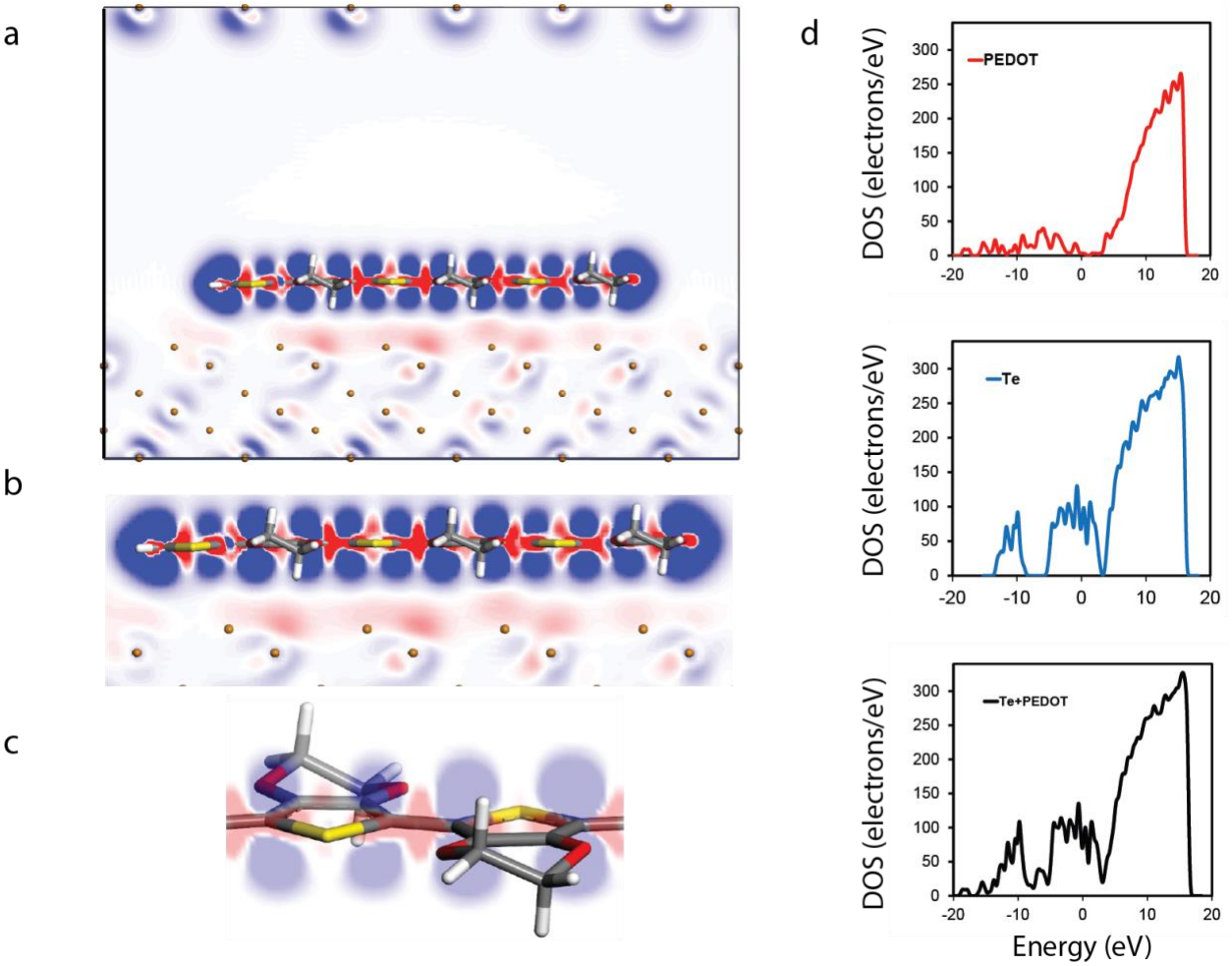

Figure 5.2 DFT calculations reveal electronic effects at the organic-inorganic interface. *a)* Charge density redistribution within polaronic PEDOT hexamer $(EDOT_6)^{2+}$ on the Te surface, as calculated by the difference in total charge density with NW surface charge density and hexamer charge density as subsets b) Electron transfer from Te surface to PEDOT chains monitored by increase of charge density (red) at the interface and decrease of charge density (blue) at the Te phase c) Detailed visual illustrating an increase of charge density (red) within PEDOT monomer bonds and σ-orbitals of PEDOT carbon atoms and a concomitant decrease (blue) observed for the π-orbitals of PEDOT carbon atoms on Te NW surface d) Density of States (DOS) calculated individually for PEDOT and Te compared with Te-PEDOT hybrid. The DOS of the hybrid is not renormalized due to minimal charge transfer across the interface.

Combined with the MD results, the DFT calculations strongly suggest that the interaction between the PEDOT and Te/$Cu_{1.75}$Te surface is a templating effect; charge transfer does occur at this interface, but no chemical bonding takes place between the organic and inorganic phases.

Hence, we expect that thermoelectric behavior in p-type PEDOT-Te hybrids is dominated by transport through the organic PEDOT matrix. This conclusion runs contrary to previous reports that have instead emphasized the role of the inorganic phase or *change in the* energy-dependent carrier scattering at interfaces as key drivers of the thermoelectric properties of hybrid materials.[59,155,156] Additionally, our results depict that the organic-inorganic interface in such hybrid systems is rich in aligned and extended PEDOT chains in addition to intra-chain charge redistribution. We conclude that alignment of PEDOT molecules at the organic-inorganic interface and charge transfer at the interface both play key roles in the high thermoelectric performance observed in the PEDOT:PSS-Te hybrid system, building upon earlier hypotheses proposing increased electrical conductivity at the interface.[24]

5.3.5 Seebeck and electrical conductivity analysis

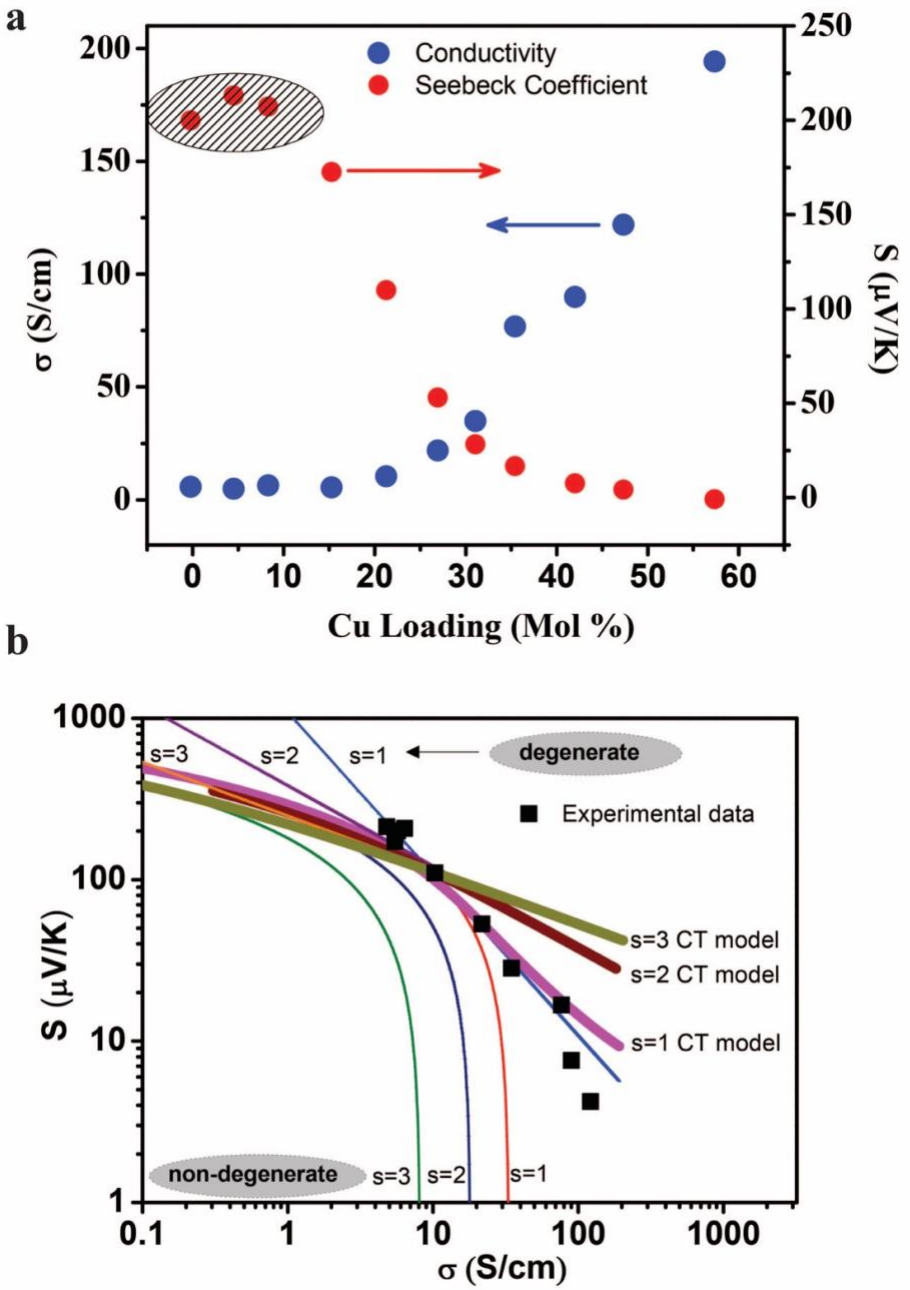

Figure 5.3 Kang-Snyder transport model applied to the PEDOT:PSS-Te(Cu_x) hybrid system. (a) Electrical conductivity and Seebeck coefficient at room temperature of the PEDOT:PSS-Te(Cu_x) NW hybrid system as a function of copper loading.[25] (b) The Kang-Snyder charge transport model with different energy-dependent scattering exponent, s, as described in the main text is shown. Our experimental data lie on the s = 1 curve, similar to pure PEDOT.

5.3.6 Thermoelectric properties and modelling using Kang-Snyder model.

Armed with structural and morphological insight, we now correlate our measurements of thermoelectric transport with the observed and simulated structures. Figure 5.3a depicts the electrical conductivity and Seebeck coefficient of the PEDOT:PSS-CuTe hybrid system as a function of copper loading. In the absence of a robust transport model for hybrid systems, researchers have previously had to rely on mean field theories. One commonly used model for multicomponent hybrids/composites is effective medium theory, which predicts that the Seebeck coefficient of the composite must lie between that of the individual materials (~190 μV/K for PEDOT:PSS-Te and ~10 μV/K for PEDOT:PSS-$Cu_{1.75}Te$ at room temperature).[162] Effective medium theory, therefore, fails to capture the observed enhancement of the Seebeck coefficient at low (~5%) Cu loading. This deviation had originally been speculated to be due to a change in the energy-dependence of carrier scattering upon introduction of Cu. Also, while the Cu loading in the composite is being varied, the overall inorganic content (Te and Cu) is controlled (typically 60-80%).[25,115]

The recently published Kang-Snyder model provides an opportunity to clarify this conundrum. Kang and Snyder showed that this framework handles pure polymeric systems well (including PEDOT); this makes the PEDOT:PSS-CuTe system a suitable candidate, since the PEDOT domains are known to be pivotal for charge transport in these hybrid materials. Further, PEDOT:PSS-CuTe is an excellent test case, since the effects of energy dependent scattering, (de-)doping, and morphology intermingle in a complex fashion. Given that the model independently treats the energy-dependent scattering (through the parameter *s*), doping (through the reduced chemical potential η), and energy-independent transport parameter $\sigma_{E_0}(T)$, such an analysis can provide insight that is both critical and previously inaccessible. According to this model, energy dependent conductivity, $\sigma_E(E,T)$ can be written as:

$$\sigma_E(E,T) = \sigma_{E_0}(T)\left(\frac{E-E_t}{k_BT}\right)^s \qquad (5.1)$$

such that the total conductivity is given by:

$$\sigma = \int_0^\infty \sigma_E(E,T)\left(-\frac{\partial f}{\partial E}\right)dE \qquad (5.2)$$

Using σ_E from Eq. 5.1 and integration by parts, the total conductivity can be written as:

$$\sigma = \sigma_{E_0}(T) \times sF_{s-1}(\eta)$$

where F is Fermi integral and $\eta = \frac{E_F-E_t}{k_BT}$ is reduced chemical potential and E_t is the transport energy, below which there is no contribution to the conductivity even at finite temperature.. The corresponding Seebeck coefficient can be written as:

$$S = \frac{k_B}{e}\left[\frac{(s+1)F_s(\eta)}{sF_{s-1}(\eta)} - \eta\right] \qquad (5.3)$$

The η value was determined by using experimental Seebeck coefficient in Eq. 5.3 for a particular value of *s*. When applying the model for pure polymers, Kang and Snyder observed that traditional semiconducting polymers (e.g. polyacetalyene) follow $s = 3$ dependence, whereas PEDOT-based

systems exhibit s = 1 dependence. In hybrid systems, it can therefore be presumed that, if transport in the polymer phase dominates the overall material properties, the energy dependence of transport (i.e. s) will remain the same as for the pure polymer matrix. If, on the other hand, transport in the hybrid material is modified by a change in the energy dependence of carrier scattering, it would be expected that s would also change. Therefore, to validate the hypothesis that the Seebeck enhancement observed in the PEDOT:PSS-Te(Cu_x) system is due to altered energy dependence of scattering, it is necessary that a change in the parameter s is observed upon introduction of Cu.

For this goal, the Seebeck coefficient of the PEDOT:PSS-Te(Cu_x) hybrid system is plotted as a function of the conductivity (Figure 5.3b) and fit to the Kang-Snyder Charge Transport model.[63] We observe that the experimental data lie on the s= 1 CT model curve (Figure 5.3b) with $\sigma_{E_0}(T) = 5.47\ S/cm$. Thus, the s dependence is unchanged between the pure PEDOT:PSS and its hybrid. Note, however, that while the Kang-Snyder model captures large trends in the S vs sigma curve, small changes such as electron filtering cannot be isolated. Hence, in order to understand the non-monotonic trend in the Seebeck and conductivity, we study in detail the effect of (de-)doping and templating on the hybrid system (Table 5.2). Combining our experimental and theoretical results, we conclude that the complex thermoelectric trends of these hybrid films are dictated by the interaction of several effects. First, as suggested by extensive MD simulations, upon the formation of PEDOT:PSS-Te NWs, there is a templating effect for PEDOT moieties on the inorganic surface. This phenomenon results in an increase of hole mobility in the interfacial polymer, increasing the electrical conductivity of the PEDOT:PSS-Te composite relative to the pristine polymer. This templating effect is weakened by the addition of Cu, which disrupts the inorganic surfaces and produces "kinked" inorganic morphologies. Secondly, detailed DFT calculations are indicative of charge transfer between the organic and inorganic phases, resulting in a de-doping effect of the *p*-type PEDOT chains (Table 5.1). In the low Cu loading regime, this de-doping effect is relatively strong, and contributes directly to the increased Seebeck coefficient and moderately decreased electronic conductivity observed here. This is contrary to previous hypotheses that a change in the energy dependence of carrier scattering is solely responsible for the non-monotonic thermoelectric trends observed in this range.

Upon further addition of Cu, a third effect emerges; Cu loading above 10% is associated with an increase in η, with only a nominal change in the σ_{E_0} value (Table 5.3). This trend indicates that the addition of Cu introduces carriers into the film and modifies the transport through a doping channel. Previous reports on this material system have suggested that positively charged Cu ions, in addition to reacting with the inorganic phase, also remain in the PEDOT phase as ionic species. These remaining Cu ions likely interact with the PEDOT chains to increase the carrier concentration in the organic phase. This effect dominates at high Cu loading, which is associated with a strong increase in the reduced chemical potential. Note that s=2 and s=3 do not fit the experimental data for any value of the transport coefficient, $\sigma_{E_0}(T)$ (Figure 5.3b is plotted on log-log scale). While, for a fixed σ_{E_0}, η is modulated by charge redistribution between the organic and inorganic phases and doping from Cu ions, only a change in morphology (templating, or kinked surfaces) can change σ_{E_0}.

Table 5.2 Summary of physical phenomena contributing to thermoelectric trends. Summary of the effects and interplay between templating, de-doping at the inorganic-organic interface and Copper loading, considering first PEDOT:PSS-Te and second PEDOT:PSS-$Cu_{1.75}Te$, and description of their respective roles on thermoelectric charge transport.

	Templating effect	De-doping due to charge transfer at organic-inorganic interface (CT)	Cu loading	Total Conductivity and Seebeck coefficient	Discussion
PEDOT:PSS	X	X	X	X	X
PEDOT:PSS-Te	$\mu(\uparrow)$ (strong)	$n_{de-doping}(\downarrow)$ $S_{de-doping}(\uparrow)$ (strong)	X	$\sigma(\uparrow) = n_{de-doping}(\downarrow) \times \mu(\uparrow)$ $S(\uparrow) \propto \frac{1}{n_{de-doping}(\downarrow)}$	Conductivity increases due to templating; Seebeck increases due to charge transfer induced de-doping – higher than PEDOT:PSS
PEDOT:PSS-$Cu_{1.75}Te$ (low Cu loading)	$\mu(\downarrow)$ (weak)	$n_{de-doping}(\downarrow)$ $S_{de-doping}(\uparrow)$ (strong)	$n_{doping}(\uparrow)$ $S_{doping}(\downarrow)$ (weak)	$\sigma(\downarrow) = \mu(\downarrow) \times \{n_{de-doping}(\downarrow)+n_{doping}(\uparrow)\}$ $S(\uparrow) \propto \frac{1}{\{n_{de-doping}(\downarrow)+n_{doping}(\uparrow)\}}$	Conductivity decreases due to further drop in templating; Seebeck increases due to stronger de-doping
PEDOT:PSS-$Cu_{1.75}Te$ (High Cu loading)	$\mu(\downarrow)$ (strong)	$n_{de-doping}(\downarrow)$ $S_{de-doping}(\uparrow)$ (weak)	$n_{doping}(\uparrow)$ $S_{doping}(\downarrow)$ (strong)	$\sigma(\uparrow) = \mu(\downarrow) \times \{n_{de-doping}(\downarrow)+n_{doping}(\uparrow)\}$ $S(\downarrow) \propto \frac{1}{\{n_{de-doping}(\downarrow)+n_{doping}(\uparrow)\}}$	Conductivity increases due to strong Cu+ induced doping; Seebeck decreases due to stronger Cu+ induced doping

Table 5.3 Transport parameters and doping values for different Copper loading.

PEDOT:PSS-Cu-Te	σ_{E0} (S/cm)	η
0%	5.47	1.62
10%	1.78	1.28
50 %	1.52	14.59

5.3.7 Validation of Kang-Snyder model for other PEDOT and P3HT based hybrid films

In order to determine if this is generally true for PEDOT:PSS based films, we applied the Kang-Snyder model to different systems (Figure 5.4a). Half-closed circles (olive) symbols show Seebeck and conductivity data on PEDOT:PSS films that are doped using an electrochemical transistor configuration.[81] Here, PEDOT:PSS is tuned by changing its oxidation state (de-doping) to obtain the optimal power factor, with presumably no change to the PEDOT morphology. Electrochemically doped PEDOS-C6 (a derivative of PEDOT) also exhibits Seebeck and conductivity data (purple close triangles) that lie on the s=1 curve with same $\sigma_{E_0}(T)$ value.[163] Open square (pink) symbols represent the Seebeck coefficient as a function of conductivity for PEDOT:Tosylate (Tos) system,[19] where the insulating PSS polyanions are replaced by the small anion Tos, which improves inter-chain π-π interaction of PEDOT chains. The PEDOT:Tos

Seebeck and conductivity data also lie on the s= 1 curve, albeit with a larger value of $\sigma_{E_0}(T)$. This is expected due to better alignment of PEDOT chains evidenced by Grazing Incidence Wide-Angle X-ray Scattering (GIWAXS) where the PEDOT:Tos contains well-ordered crystallite grains surrounded by some amorphous PEDOT:PSS regions. This is distinctly improved from the electrochemically doped PEDOT samples described above. $\sigma_{E_0}(T)$ value is further improved in the PEDOT:Tos-Pyridine+triblock copolymer system by controlling the oxidation rate as well as crystallization of oxidized PEDOT which further reduces film defects.[21]

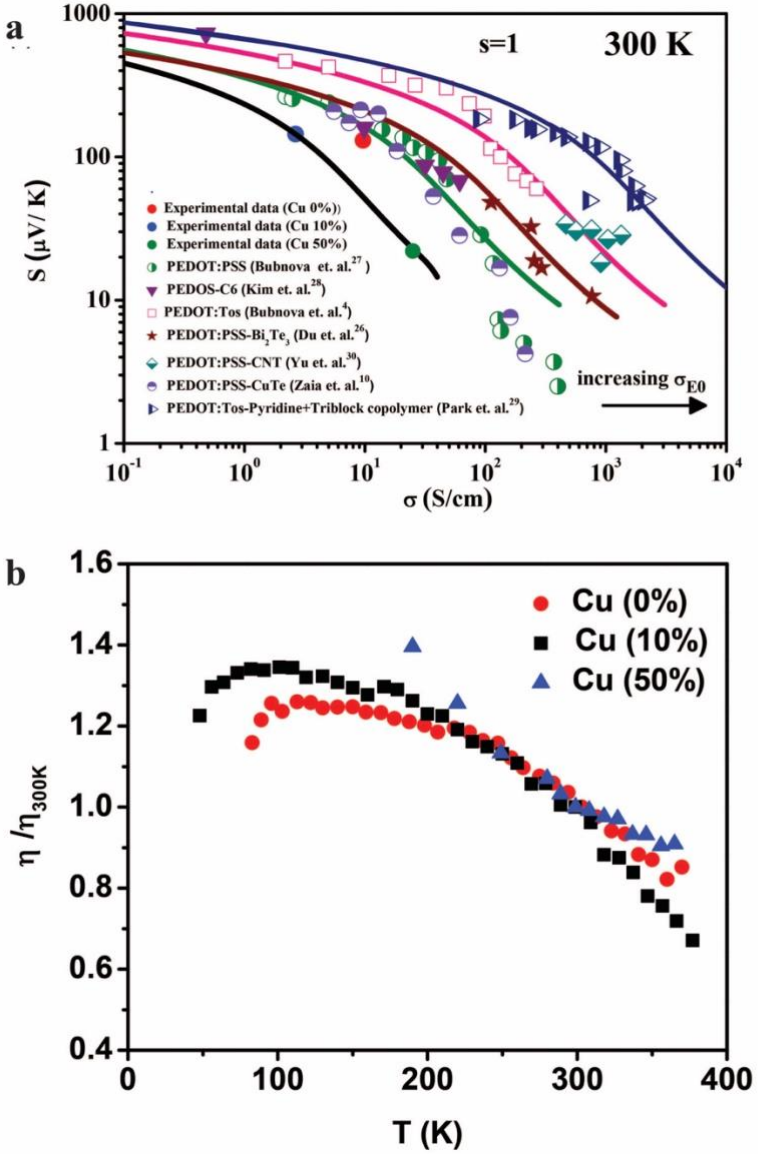

Figure 5.4 Kang-Snyder transport model applied to various PEDOT based composites. (a) Experimental data of Seebeck (S) vs conductivity (σ) for PEDOT:PSS (half closed green triangles)[81], PEDOS-C6 (closed triangles)[163], PEDOT:Tos (open squares)[19], PEDOT:PSS-Bi_2Te_3(closed triangles)[59], PEDOT:PSS-CNT[57](half closed spades), PEDOT:PSS-Te(Cu_x) NW hybrid system (half closed circles)[25] and PEDOT:Tos-Pyridine (half closed triangles)[21] modelled with s=1(solid lines). It is seen that irrespective of the dopant counter-ion used, all hybrid PEDOT-based systems lies on s=1 curve with different σ_{E_0} transport coefficient values, indicating that

energy-dependent scattering is not changing in these organic-inorganic hybrid films. (b) Reduced chemical potential , $\eta = (E_F - E_t/k_BT)$ of the PEDOT:PSS-Te(Cu_x) system plotted as a function of temperature for 0% (red closed circle), 10% (black closed squares) and 50 % Cu (closed blue triangles) samples, respectively. In line with expectations from the Kang-Snyder model, the reduced chemical potential only changes <30% over a large temperature range in the samples and the change does not depend upon the Cu loading. The data is normalized with respect to the doping level at 300K (η_{300K}).

Table 5.4 Transport parameters for PEDOT and P3HT based pure polymer and hybrid films.

Material	**σ_{E0} (S/cm)**
PEDOT:PSS-C6	8.5
PEDOT:PSS (electrochemical)	8.5
PEDOT:Tos	61
PEDOT:Tos+Pyridine	260
PEDOT:PSS-Bi_2Te_3	14
P3HT:Bi_2Te_3	0.003
P3HT:MCNT	0.2, 0.001
P3HT:SWCNT	0.001

Interestingly, in comparison with pure organic derivatives of PEDOT, PEDOT-based hybrid films (half closed circles, closed stars and half closed shades in Figure 5.4a)[25,57,59] also follow the *s*= 1 curve, with either the same value of $\sigma_{E_0}(T)$ as the pure polymer or higher (Table 5.4). For a second batch of PEDOT:PSS-CuTe samples, 0% Cu loading (closed red circle), the Seebeck and conductivity data lies on the same *s*=1 curve as for Zaia et. al.[25] Here, we observe that as the Cu loading increases to 10%, the Seebeck is enhanced and the conductivity decreases (closed blue circle). This lower value of $\sigma_{E_0}(T)$ is consistent with curvature arising from 'kinked' $Cu_{1.75}Te$ phase formation within the heteronanowires (Figure 5.1d) as well as reduced movement of the PEDOT on the $Cu_{1.75}Te$. The associated Seebeck increase is due to a de-doping effect, as η is observed to decrease slightly when Cu loading is increased from 0 to 10%. With further loading of Cu, the Seebeck decreases and the conductivity increases (further details about the de-doping and doping can be found in Supplementary Note 4). In this regime, there is presumably little change in the PEDOT morphology at the organic-inorganic interface, and the increased conductivity and reduced Seebeck are a result of a doping effect associated with additional copper loading. Hence, both 10% and 50% Cu loading samples lie on the *s*=1 curve with same $\sigma_{E_0}(T)$ values (Figure 5.4a). Coupled with other PEDOT-based hybrids (Figure 5.4a), we can conclude generally that the energy-dependence of carrier scattering is independent of the type of doping, or indeed the inorganic constituent, contrary to many reports in the literature. This result provides key evidence that carrier transport in hybrid films occurs predominantly through PEDOT itself (to corroborate this, we also performed experiments on Te NWs in an insulating polymer matrix). Counter-ions and inorganic constituents impact transport mainly via the transport parameter, $\sigma_{E_0}(T)$, which can be attributed to morphological/templating effects in the PEDOT phase. The increase in $\sigma_{E_0}(T)$ in hybrid materials can be qualitatively understood as enhancing the effective mobility of the itinerant carriers within the PEDOT polymer matrix. It is interesting, albeit counter-intuitive, that this can occur as a result of introducing numerous new potential scattering interfaces in the material via addition of inorganic components or secondary phases.

However, that introduction of inorganic species can provide templating effects in polymers which lead to structural or behavioural modifications is well-known.

To gain deeper insight into the transport coefficient, $\sigma_{E_0}(T)$, we performed temperature dependent Seebeck and conductivity measurements on these hybrid films. The reduced chemical potential with respect to room temperature value, η/η_{300K}, does not change significantly with lowering temperature as shown in Figure 5.4b (24%, 35% and 40% for 0, 10 and 50 % Cu loading respectively from room temperature value). The temperature dependence of $\sigma_{E_0}(T)$ can be written as $\sigma_{E0} \propto \exp(-\frac{W_\gamma}{k_B T})^\gamma$ where W_γ is akin to a hopping energy; while W_γ shows a small enhancement with initial Cu loading (W_γ =0.57 eV for 0% Cu & 0.69 eV for 10 %), it decreases for 50 % Cu loaded sample (0.28eV).

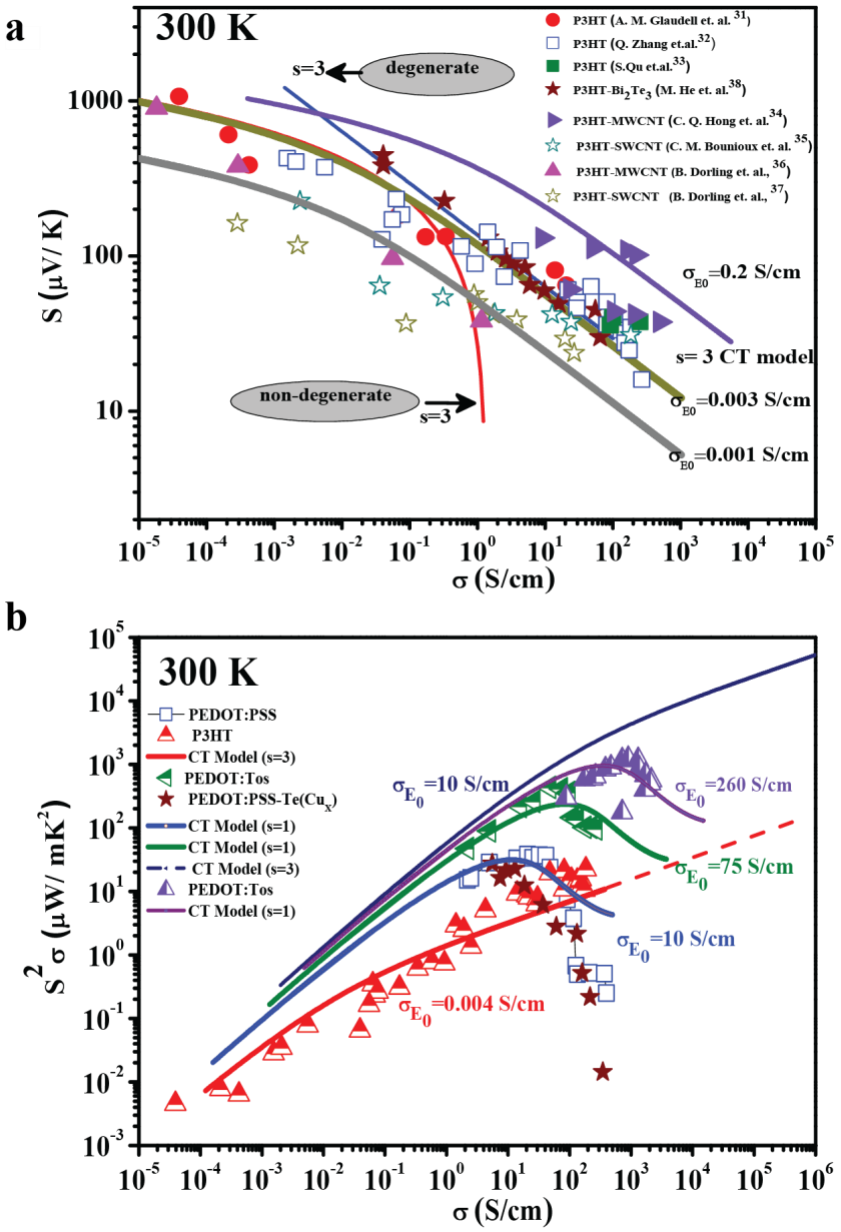

Figure 5.5 Kang-Snyder model applied to various P3HT-inorganic composites. (a) The electrical conductivity vs Seebeck coefficient data of F_4TCNQ doped P3HT (closed circles)[164], $Fe((CF_3SO_2)_2N)_3$ doped P3HT (open squares)[165], highly aligned P3HT with trichlorobenzene (closed squares)[166], P3HT:MWCNT (closed triangles)[167,168], P3HT:SWCNT (open star)[60,169] and P3HT:Bi_2Te_3 (closed stars)[170] hybrid systems. It is seen that experimental data lies on s= 3 curve, again consistently identical for the hybrid and the pure polymeric systems. (b) Comparison of power factor of PEDOT (s=1) and P3HT (s=3) based hybrids. Targeting higher $\sigma_{E_0} \sim 10$ S/cm in a s=3 polymer can push power factors of hybrid materials towards values comparable to inorganic thermoelectric materials.

In order to test if our hypothesis that charge conduction in hybrid systems occurs mainly through the polymer matrix, we also consider hybrid films constituted from a different (i.e. non-PEDOT) well-established conducting polymer as a matrix, P3HT. We compared, in a similar fashion as above, F_4TCNQ vapor-doped P3HT samples[164] (closed circles), $Fe((CF_3SO_2)_2N)_3$ doped P3HT (open squares)[165], highly aligned P3HT with trichlorobenzene (closed squares)[166], to P3HT:Bi_2Te_3 (closed stars)[170], P3HT:SWCNT (open star) and P3HT:MWCNT (closed triangles) hybrid systems from literature[60,167–169] and used the Kang-Snyder model (Figure 5.5a). These P3HT-based systems lie on the s=3 curve with same $\sigma_{E_0}(T)$ (Table 5.4). In the case of P3HT:SWCNT(MWCNT) hybrid systems, while the sparse literature data available lies on the s=3 curve with different value of σ_{E_0}, some do indeed deviate for higher values of conductivity. There is a possibility of strong π-π interactions between CNTs and P3HT, which has been hypothesized to cause deviations from the s=3 curve[171] and is indeed an exciting future avenue for exploration. The conclusion, in the case of P3HT:Bi_2Te_3, is identical to that for the PEDOT based films wherein the energy dependence of the scattering in the hybrid films is similar to that of pristine polymeric films. Figure 5.5b shows power factor ($S^2\sigma$) for the PEDOT and P3HT based systems. While for PEDOT based hybrids, the power factor shows an optimum for different $\sigma_{E_0}(T)$ values, it increases continuously for P3HT based hybrids. The value of power factor is hypothesized to be lower in P3HT based systems because of a low value of σ_{E_0} due to side alkyl side-chains; although alkyl chains help to make these solution processable, it degrades the alignment and orientation of the P3HT polymer chains[172,173]. Hypothetically, if a P3HT-based hybrid film with σ_{E_0} approaching 10 S/cm is manufactured, the power factor would be as high as 10 mW/mK^2. Therefore, it is clear that, so far, the key to high thermoelectric performance in these complex hybrid systems has been the advantage gained by physical interfacial interactions and exploiting polymeric templating effects capable of enhancing carrier transport in the organic phase, rather than modifying the energy dependence of scattering.

5.4 Conclusions

In conclusion, by combining experiment, first principles calculations, and molecular dynamics, we show that the high thermoelectric performance achieved in PEDOT:PSS-CuTe nanowires is driven primarily by thermoelectric transport in the organic phase. Contrary to previous understanding, this transport is enhanced due to a physical templating effect at the organic-inorganic interface accompanied by charge transfer induced de-doping at the interface, rather than cooperative interfacial transport or modification of the energy dependence of scattering. Significantly, we apply the Kang-Snyder charge transfer model to a wide variety of organic-inorganic hybrids and demonstrate that it provides an effective framework to describe composite materials. Pairing our experimental data with results from literature, we demonstrate that the key to high performing hybrid materials lies in the energy-independent transport coefficient, $\sigma_{E_0}(T)$. This provides a general result suggesting that the role of energy dependent scattering in hybrid materials has been systematically overestimated. Instead, transport in most hybrid systems can be understood within the context of the individual components, with enhancements arising from physical interactions such as templating. In summary, this work lays out a clear framework for development of next generation soft thermoelectrics: leverage upon stronger energy dependent scattering (s=3) polymers, enhance chemical interactions between inorganic and organic constituents, and create architectures and templates emphasizing interfacial design capable of high-conductivity domains

in the organic phase that enhance mobility of charge carries. These are three well-defined routes that can be impactful in the near future.

5.5 Experimental

5.5.1 Synthesis and Characterization

Synthesis of PEDOT:PSS-Te NWs and PEDOT:PSS-Te(Cu_x) NWs closely followed previous methods.[24,25] All steps in the procedure are carried out in aqueous solution in the presence of air, with high reproducibility over many separate experiments. As shown in our previous report, during conversion to PEDOT:PSS-Te(Cu_x) NWs, mobile copper ions penetrate the PEDOT:PSS surface layer to react with the Te core and form isolated alloy domains of $Cu_{1.75}Te$.[25] During this process, the nanowires undergo a transition from rigid rods (Figure 5.1a) to curved wires, with alloy domains appearing at 'kinked' portions of the wires (Figure 5.1b). The resulting nanostructures are Te-$Cu_{1.75}Te$ heterowires. The extent of copper loading in each sample was directly measured using Inductively Coupled Plasma Optical Emission Spectroscopy (ICP-OES). After synthesis, x-ray diffraction (XRD), scanning electron microscopy (SEM), and x-ray photoelectron spectroscopy (XPS) were used to confirm the material structure and properties.

5.5.2 MD Simulations

In order to investigate the morphology and configuration of PEDOT:PSS on Te and $Cu_{1.75}Te$ NW surfaces, a 27×20 supercell (12.0x11.8 nm^2) of Te [100] surface with 4947 Te atoms and a 6×28 supercell (10.8×11.1 nm^2) of $Cu_{1.75}Te$ [010] surface with 9073 atoms ($Cu_{5787}Te_{3286}$) are constructed, respectively. Ten and eight layers of atoms were used for the surface thickness which corresponds to 13.36 Å and 12.07 Å for Te and $Cu_{1.75}Te$, respectively. Molar ratio of polymers were determined as 1:2 for PEDOT:PSS in simulations according to experimental results.[174]

Canonical ensemble-molecular dynamics (NVT-MD) are used within the framework of Forcite Plus package of Materials Studio.[175] Ten annealing cycles between 300 K and 1300 K were carried out for equilibrium followed by 5000 steps smart minimization. The total annealing time is at least 5 ns with 0.5 fs time step and Nosé-Hoover Thermostat method is adopted for temperature control. Condensed-phase Optimized Molecular Potentials for Atomistic Simulation Studies (COMPASS)[176] is used to evaluate the atomic forces.[177,178] A summation method of non-bonded electrostatic forces controlled by Ewald[179] and van der Waals forces by "atom-based" is employed in periodic cells. 11 Å atomic cut-off distance was used for vdW interactions. Three different cubic amorphous cells were prepared including five chains of $EDOT_{18}$ and SS_{36} mixture for PEDOT:PSS simulations (Figure 5.1e-f), 20 chains of $EDOT_{18}$ for pristine PEDOT simulations and 10 chains of SS_{36} for pristine PSS simulations on Te and $Cu_{1.75}Te$ surfaces respectively. Each simulation was repeated at least three times with simulated annealing protocol for different amorphous polymers to investigate structural changes.

Six $EDOT_{12}$ and three SS_{24} oligomers were used to calculate interaction energies with the Te and $Cu_{1.75}Te$ NW surfaces. Similarly, six $EDOT_{12}$ oligomers distributed randomly onto the NW surface was used to study directional preference and self-assembly of chains on surfaces.

5.5.3 DFT Calculations

Based on the experimental results, a Te [100] surface[180] is cut with six subtract layers under it and a 20 Å vacuum slab above it to ensure no interlayer interaction. The simulated XRD diffraction pattern of this model agrees exactly with the experimental TEM and SEM images[162,181–183]. A 3×6 (13.2×35.5 $Å^2$) supercell with a PEDOT hexamer aligned along the Te NW growth direction and a 6×3 (26.4×17.7 $Å^2$) supercell with a PEDOT hexamer a perpendicular to the Te NW growth direction are prepared, respectively. Similarly, a $Cu_{1.75}Te$[184] [010] surface cut and a 2×3 (43.4x12.5 $Å^2$) supercell with 20 Å vacuum above are prepared respectively followed the same method. Adsorption energy, density of states (DOS), electrostatic potential surface and electron density differences between surface and PEDOT are calculated based on Density Functional Theory[185] within the framework of plane-wave implemented in the Cambridge Serial Total Package (CASTEP).[186] Tkatchenko-Scheffler (TS)[187] scheme dispersion corrected Perdew–Burke–Ernzerhof functional[188] with van der Waals consideration (PBE-D) are adopted as exchange-correlations, and generated on the fly (OTFG) ultrasoft potentials are used to describe interactions with a cutoff energy, 490 eV for Te for 571 eV for $Cu_{1.75}Te$. Total energy convergence is 1×10^{-6} eV/atom and the force on the atom is 0.03 eV. The maximum stress is 0.05 GPa and the maximal displacement is 0.01 angstrom. BFGS algorithm is used for geometry optimization and surface relaxation. The adsorption energy was calculated according to the equation: $E_{[ads]} = E_{[total]} - (E_{[monomer]} + E_{[NW]})$; here, $E_{[ads]}$, $E_{[total]}$, $E_{[monomer]}$ and $E_{[NW]}$ represent the adsorption energy, the total energy of a single monomer/oligomer adsorbed on the Te surface, the energy of isolated monomer/oligomer and the energy of Te-based nanowires respectively. Molecular properties such as electrostatic potential surfaces and highest occupied molecular orbitals are calculated by using DMOL3 software at the same level of DFT functional[189].

5.6 Acknowledgements

This work was partially performed at the Molecular Foundry, Lawrence Berkeley National Laboratory, and was supported by the Department of Energy, Office of Science, Office of Basic Energy Sciences, Scientific User Facilities Division of the U.S. Department of Energy under Contract No. DE-AC02-05CH11231. This work was also partially performed at the Agency for Science, Technology, and Research, supported by the Science and Energy Research Council under the Pharos grants 1527200018 and 1527200024. EWZ gratefully acknowledges the National Science Foundation for fellowship support under the National Science Foundation Graduate Research Fellowship Program.

Chapter 6. Molecular level insight into enhanced n-type transport in solution-printed hybrid thermoelectrics

Adapted from "Molecular level insight into enhanced n-type transport in solution-printed hybrid thermoelectrics," EW Zaia, MP Gordon, V Niemann, J Choi, R Chatterjee, CH Hsu, J Yano, B Russ, A Sahu, JJ Urban. *Advanced Energy Materials*, 2019, 9.13, 1803469 (DOI: 10.1002/aenm.201803469) with permission of the authors. *Reproduced with permission of Advanced Energy Materials*.

6.1 Abstract

Perylene diimide (PDI) derivatives hold great promise as stable, solution-printable n-type organic thermoelectric materials, but as of yet lack sufficient electrical conductivity to warrant further development. Hybrid PDI-inorganic nanomaterials have the potential to leverage these physical advantages while simultaneously achieving higher thermoelectric performance. However, lack of molecular level insight precludes design of high performing PDI-based hybrid thermoelectrics. Herein, we report the first explicit crystal structure of these materials, providing previously inaccessible insight into the relationship between their structure and thermoelectric properties. Allowing this molecular level insight to drive novel methodologies, we present simple solution-based techniques to prepare PDI hybrid thermoelectric inks with up to 20-fold enhancement in thermoelectric power factor over the pristine molecule (up to 17.5 μW/mK2). This improved transport is associated with reorganization of organic molecules on the surface of inorganic nanostructures. Additionally, outstanding mechanical flexibility is demonstrated by fabricating solution-printed thermoelectric modules with innovative folded geometries. This work provides the first direct evidence that packing/organization of organic molecules on inorganic nanosurfaces is the key to effective thermoelectric transport in nanohybrid systems.

6.2 Introduction

Flexible thermoelectric devices can realize energy generation or solid-state heating/cooling devices with conformal geometries, enabling a new portfolio of applications for thermoelectric technologies.[150] As personal electronic devices become increasingly ubiquitous, interest in flexible thermoelectric devices for portable, renewable energy generation and localized cooling, particularly in wearable technologies, has surged.[8,10,190] Propelled by the emergence of new classes of organic semiconductors, polymers, and organic-inorganic composites over the past few years, several flexible thermoelectric devices capable of power generation have been successfully demonstrated.[138,144,191] These soft thermoelectric materials are rapidly catching up to their inorganic counterparts in terms of thermoelectric efficiency, while leveraging significant advantages from a processing standpoint.[7,19,151] In general, solution-processed soft thermoelectrics open the door to a variety of new thermoelectric applications due to flexible form factors and scalable, roll-to-roll fabrication techniques without the need for costly energy-intensive processing steps.[6]

The performance of a thermoelectric material is often evaluated using the dimensionless figure of merit, $ZT=S^2\sigma T/\kappa$, which encompasses three material properties: the Seebeck coefficient or thermopower (S), electrical conductivity (σ), and thermal conductivity (κ). Fabricating a commercially viable thermoelectric module requires both high performing *p*-type (hole transporting) and *n*-type (electron transporting) materials, which are connected electrically in series and thermally in parallel. Recent work in soft thermoelectrics has seen impressive progress in improving power factors in this class of materials. However, there is a striking scarcity of high performing n-type soft materials due to poor electron transport properties and insufficient stability in ambient conditions.[8,150]

State of the art organic n-type materials include organometallic poly(metal 1,1,2,2-ethenetetrathiolate) derivatives, which have demonstrated power factors up to 66 $\mu W/mK^2$, but these materials rely on solid-state powder processing, making them unfavorable from a processing standpoint.[105] To avoid the challenges and costs of solid-state processing, focus has shifted to solution-processed materials. Within this family of solution-processed thermoelectric materials, doped single-walled carbon nanotubes and halogenated benzodifurandione-based oligo (p-phenylene vinylene) (BDPPV) derivatives have achieved power factors up to 18 and 28 $\mu W/mK^2$, respectively.[53,107] Of particular interest are small molecules such as perylene diimide (PDI) derivatives which exhibit good electronic conductivity, air stability, water solubility, and tunability of both electronic and optical properties.[111,192] PDIs have been used as pigments since the 1950s, and are therefore inexpensive to synthesize at large scale. Self-doped PDIs have been reported to achieve up to 1.4 $\mu W/mK^2$ power factors, a good starting point for materials development but too low to be of practical use at the present.[109,111] Such materials are exceptionally attractive in the effort to realize solution-printed thermoelectrics for wearable and personal electronic application, but even greater power factors are needed.

Hybrid organic-inorganic materials have been identified as a particularly promising path towards next generation n-type soft thermoelectrics due to their ability to realize performances exceeding that of either individual constituent while still leveraging the unique advantages of soft thermoelectrics.[29] For example, a composite formed from 2D TiS_2 nanosheets with C_{60} nanoparticles was shown to achieve a ZT as high as 0.3 at 400K (a power factor of ~375 $\mu W/mK^2$), exceeding the reported ZT values for either individual component.[52,193] While this result highlights the potential of organic-inorganic composites to realize impressive thermoelectric performance, hybrid materials of this sort require multi-step, energy intensive fabrication processes including high-temperature, low-pressure synthesis (640°C for 3 days) and solid-state ball milling. In order to develop commercially relevant materials, there is a strong need to innovate versatile techniques for the production of n-type thermoelectrics using solely low-temperature, solution-based operations compatible with ambient conditions.

Moreover, while it is known that the organic/inorganic interface plays a key role in the high performance of these composites, lack of detailed structural data and insufficient contrast at the organic/inorganic interface has stymied efforts to conclusively elucidate the mechanisms behind such performance enhancements. Current state-of-the-art in this material class has implicated physical phenomena such as interfacial transport, structural/morphologic effects, and modification of the energy dependence of carrier scattering, or energy filtering, in these thermoelectric trends.[24,25,51,73,154] Recent work has suggested that the role of energy filtering has been overstated

in this field, and instead structural/morphological effects and interfacial charge transfer at the organic-inorganic interface are largely responsible for enhanced thermoelectric performance in hybrid materials.[75,82] For example, it was reported that, in composites of tellurium nanowires and poly(3,4-ethylenedioxythiophene):poly(styrene sulfonate) (PEDOT:PSS), the organic component self-assembled into an ordered structure at the surface of the inorganic nanostructure, creating a region of high local ordering and contributing to enhanced carrier transport. However, investigation of this so-called templating effect of the organic component on the inorganic surface has thus far been theoretical, driven by molecular dynamics and density functional theory. Directly probing the hard-soft interface in hybrid materials is challenging, and thus experimental observation of this templating effect remains elusive.

In this Chapter, we present a novel, versatile approach to prepare stable n-type hybrid thermoelectrics using low-temperature, ambient techniques, while simultaneously providing new insight into the mechanism behind high performance in organic-inorganic hybrid thermoelectrics. PDIs were used as the organic component due to their large scale and inexpensive synthesis, electronic conductivity, solution processability, chemical tunability, and air stability.[111,194] Tellurium nanowires (Te NWs) were chosen as the inorganic component. Te NWs are a well-studied prototypical thermoelectric material, capable of being synthesized at large scale and doped either *n*- or *p*-type.[25,195] Recent work has shown that Te NWs are amenable to platform ligand exchange techniques, providing a methodological precedent for forming PDI-Te composites.[154] Additionally, it has been shown that the Te nanowire surface can act as a structural template for conductive polymer ligands, generating locally high conductivity at the hard-soft interface.[75] Both components in this hybrid system can be synthesized at scale using low temperature, solution-based techniques and produce air-stable films. Furthermore, the two components are likely to be energetically compatible, with only a slight offset in their work functions as determined via UPS (as well be discussed later). In this work, we develop a new approach to preparing high performance PDI-Te hybrid thermoelectrics. We first apply the current literature state-of-the-art hybrid preparation methodology (for simplicity, this method will hence be called Method A), and perform detailed investigation of the structural and energetic properties of the composites. Notably, we provide the first explicit solution for the crystal structure of these materials, allowing us to fill a critical gap in the literature and tie molecular level information to the observed trends in thermoelectric performance of these materials. Driven by new physical understanding of the material system, the hybrid preparation methodology is revisited, and a second methodology is developed (we will refer to this as Method B). Utilizing this new approach, we prepare PDI-Te composites that are able to achieve up to 20-fold enhancement in the thermoelectric power factor over pure PDI films. Moreover, the detailed investigation of the structural and energetic properties of the composites provides the opportunity to directly relate molecular level phenomena to macroscopic performance metrics, providing key understanding previously missing in the literature and informing future work on organic-inorganic composite systems for thermoelectric and electronic applications. Finally, we demonstrate that this approach is compatible with next-generation flexible thermoelectric applications by fabricating solution-printed thermoelectric generators with flexible and novel architectures.

6.3 Results and Discussion

6.3.1 Thermoelectric Characterization (Method A)

Following a previously published platform methodology (Method A), PDI capped Te nanowires (PDI-Te NWs) were first prepared via a ligand exchange technique, in which sulfur is used as a linker molecule to mediate binding between the Te and PDI domains (Figure 6.1a). Full synthetic details are provided in the experimental section. Method A represents an intuitive approach extending a current state-of-the-art technique from the literature, shown to be broadly effective in producing a variety of organic-inorganic composites.[154] PDI-Te composites were prepared at a variety of compositions, and their thermoelectric, structural, and electronic properties investigated.

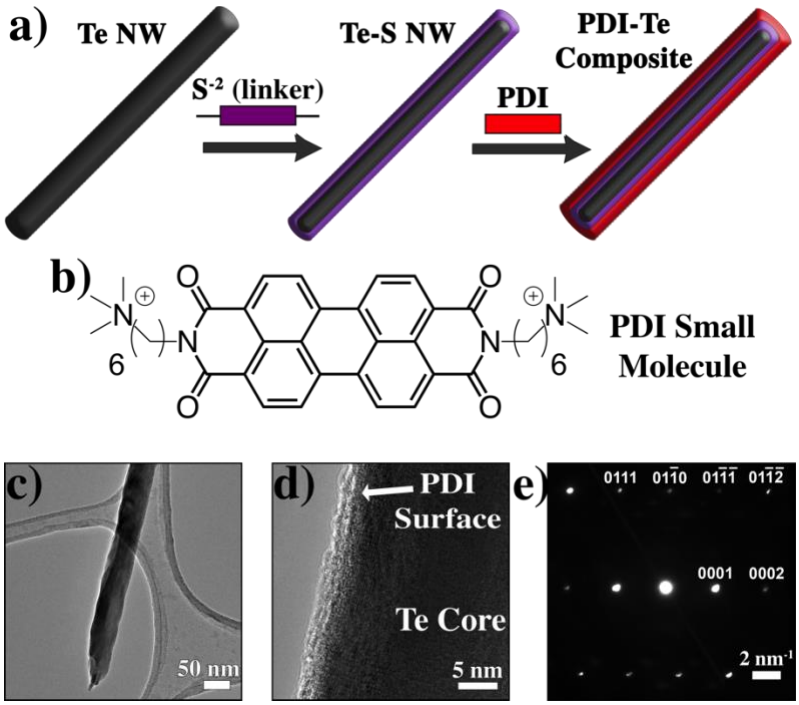

Figure 6.1 (a) Cartoon depiction of platform-based design scheme for *n*-type hybrid nanostructures, Method A. (b) Chemical structure of PDI small molecule with high thermoelectric properties. (c) TEM depicts high quality, single crystal Te nanowires. (d) HRTEM reveals functional organic layer has successfully been strongly adhered to inorganic nanowire core. (e) SAED confirms inorganic core is single-crystalline Te.

We first examine the effect of composition on thermoelectric performance of PDI-Te composites prepared via Method A. Figure 6.2a depicts the electrical conductivity and Seebeck coefficient of PDI-Te composites prepared via Method A with varying PDI content. Significantly, we observe non-monotonic trends in both the Seebeck coefficient and the electrical conductivity. Such a trend necessitates some hybridizing interaction between the organic and inorganic phases in the composite films; otherwise, standard effective medium theory would predict that the composite performance should lie intermediate between that of the pure components.[29] These non-monotonic trends were reproduced over five independent syntheses. It is also important to note that the thermoelectric performance of these hybrid films exceed that of either starting materials, a result with important implications for the design of hybrid thermoelectric devices. In PDI-Te composites

prepared via Method A, the thermoelectric power factor is enhanced greater than six-fold over pure PDI, driven by increased electrical conductivity in the high PDI regime. Clearly, it is critical to understand the nature of this performance enhancement in order to provide insight for next-generation hybrid thermoelectric material design.

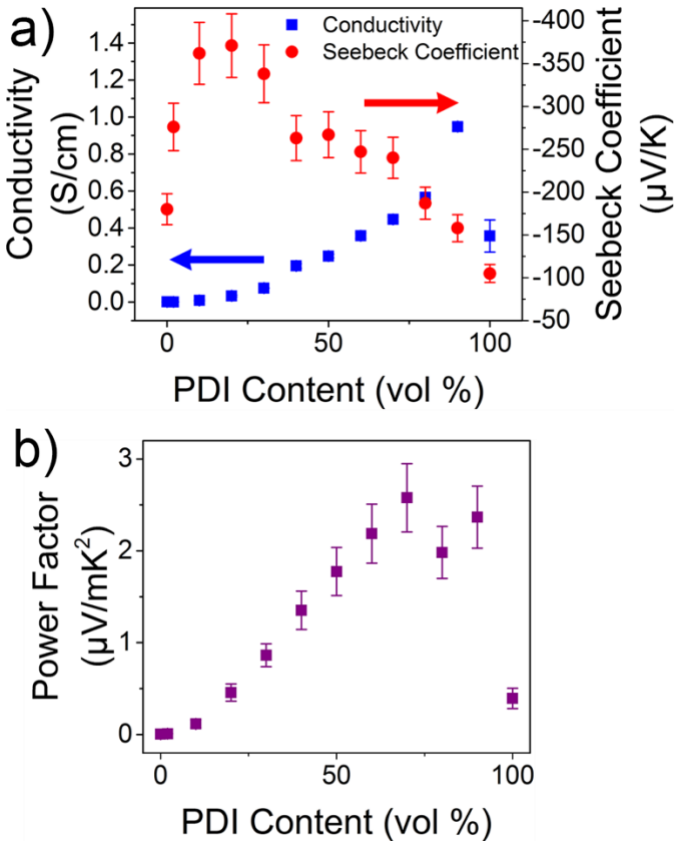

Figure 6.2 PDI-Te composite nanostructures prepared via Method A demonstrate enhanced thermoelectric performance relative to pure components. (a) Significantly, non-monotonic trends are observed in both electrical conductivity and Seebeck coefficient. These phenomena are reproducible over five separate experiments. (b) PDI-Te composites demonstrate up to six-fold improvement in power factors in the high PDI regime.

In order to investigate this phenomenon, we consider the conductivity of a material, which can be written as:

$$\sigma = ne\mu$$

where the electrical conductivity (σ) is a function of the charge carrier density (n) and mobility (μ), where e is the elementary charge. Thus, the improved conductivity of these films must be the result of either doping of additional free carriers into the system or increased carrier mobility. On the other hand, non-monotonic trends in the Seebeck coefficient of composite semiconductors can be the result of many factors, such as doping/dedoping, shifts in the slope of the density of states, and energy-dependent scattering phenomena.[25,78] In order to elucidate the physical origin of the non-monotonic trends in the composite electrical conductivity and Seebeck coefficient and, in turn, the improved thermoelectric performance in hybrid PDI thermoelectrics, each of these factors is investigated.

6.3.2 Quantitation of Carrier Concentration

A parameter key to both electrical conductivity and Seebeck coefficient is the concentration of conductive charge carriers. Several groups have observed self-doping effects in similar PDI systems, and similar doping effects could be responsible for the enhanced electrical conductivity in the hybrid films with high PDI content. In order to test this hypothesis, both ultraviolet-visible-near infrared absorption (UV-vis-NIR) and electron paramagnetic resonance (EPR) were performed on hybrid films of varying PDI content. UV-vis-NIR absorption spectra depict the expected optical transitions in the visible range, with three characteristic peaks representative of PDI polaron charge carriers (~730 nm, 800 nm, 1100 nm), consistent with previous literature (Figure 6.7).[111,196,197] The spectra are quite similar for all films in the high PDI regime, which is not suggestive of significant changes in carrier concentration. Further corroborating this conclusion, the charge carrier densities in the composite films all appear to be of the same order of magnitude in the high PDI regime, as quantified by EPR (Figure 6.3).[198–200] In fact, composites with high PDI content, which exhibit enhanced electrical conductivities relative to pure PDI, actually demonstrate slightly reduced carrier concentrations. Films with low PDI content show significantly lower spin concentrations, suggesting that PDI acts as both stabilizing ligand and active dopant in this system. We also note that the doping levels in these films are quite high, consistent with previous reports.[111,196] Combined, these data indicate that changes in the carrier concentration cannot be solely responsible for the increased electrical conductivity and subsequent improvement in thermoelectric performance observed in the hybrid films. Instead, these phenomena must be the result of changes in the apparent thin film electron mobility. That is, the addition of inorganic nanostructures influences the thermoelectric performance of hybrid films through a mobility channel. To further illustrate this point, the carrier mobilities of the PDI-Te thin films with varying PDI content have been extracted from this EPR data and plotted (Figure 6.8). A peak is clearly observed in the high PDI regime, coincident with the enhanced electrical conductivity and thermoelectric power factor observed in this hybrid system. Moreover, Hall measurements were performed to independently probe the carrier mobilities in the same PDI-Te thin films, demonstrating an identical trend to the EPR approach (Figure 6.8). Both approaches independently corroborate the conclusion that increased carrier mobility in the high PDI regime is responsible for the enhanced thermoelectric performance observed in these hybrid films. Such a mobility gain is likely related to the morphology and structure of the PDI domains in the thin film. In light of this result, it is critical to understand the molecular ordering of PDI in the hybrid films.

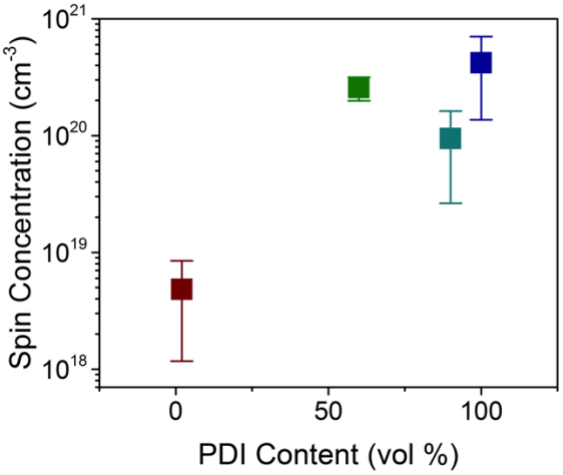

Figure 6.3 EPR measurements allow quantification of unpaired spin concentration in samples with varying PDI content prepared via Method A. While high PDI composites demonstrate enhanced conductivity relative to pure PDI, they surprisingly demonstrate slightly reduced spin concentrations, suggesting that doping is not the key factor in the non-monotonic conductivity trends observed in this regime.

6.3.3 Characterization of Crystal Structure and Molecular-Level Ordering

In order to characterize the structure and packing of PDI molecules in the solid state, grazing-incidence wide angle X-ray scattering (GIWAXS) was performed on thin film samples consisting of (1) pure PDI, (2) pure S-Te NWs, and (3) composite PDI-Te NW films with varying PDI content. For this experiment, samples were prepared via Method A, and a wide range of PDI content (2 – 98 vol%) was investigated. While GIWAXS has been performed on films of these PDI molecules before, the complexity of the resulting spectra has impeded detailed crystallographic indexing until now.[111] Using high quality 2D GIWAXS data obtained using the Lawrence Berkeley National Laboratory (LBNL) Advanced Light Source (ALS) synchrotron, we report an explicit solution for the crystallographic structure of PDI molecules with high thermoelectric performance for the first time. This result enables more thorough understanding of the structural factors contributing to the high conductivity observed in PDI-Te hybrid nanostructures.

Structural studies have been performed on several similar small molecule systems, providing useful context for this work. In 2006, Guillermet et al. described the monoclinic crystal structure of a small molecule consisting of just the planar 3,4,9,10-perylene-tetracarboxylicacid diimide core.[201] Following reports observed similar monoclinic unit cells for crystals formed from planar PDI derivatives, while triclinic structures were observed in PDI molecules with alkyl side chains due to increased mobility and entanglement.[202,203] Klebe et al. observed a distorted triclinic unit cell in crystalline perylene-3,4:9,10-bis(dicarboximide), a molecule similar to the one presented in this report but with hydroxyl terminated side chains rather than amine terminated, indicating that functional side groups distort the unit cell further.[204] Commonalities in these reports include strong 001 and 002 reflections (representing end-to-end stacking of the PDI derivatives), “slipped” π-π

stacking of the conjugated core, and significant (45-55°) angles between the substrate and the π-π stacking direction.

The 2D GIWAXS pattern presented in this work for pure PDI films is shown in Figure 6.4e. The pattern is consistent with previous reports, in which explicit indexing was not reported.[111] Here, we present a solution for the triclinic crystal structure observed in these materials, with the unit cell parameters summarized in Table 6.1. Upon geometric relaxation (using a Forcite package), these PDI molecules are observed to pack in a similar fashion to the analogous materials described previously (Figure 6.4f-g).[205] Additionally, an integrated and indexed 1D GIWAXS spectrum is presented in Figure 6.9 (see Supporting Information for this chapter) with a simulated XRD pattern further corroborating this result.

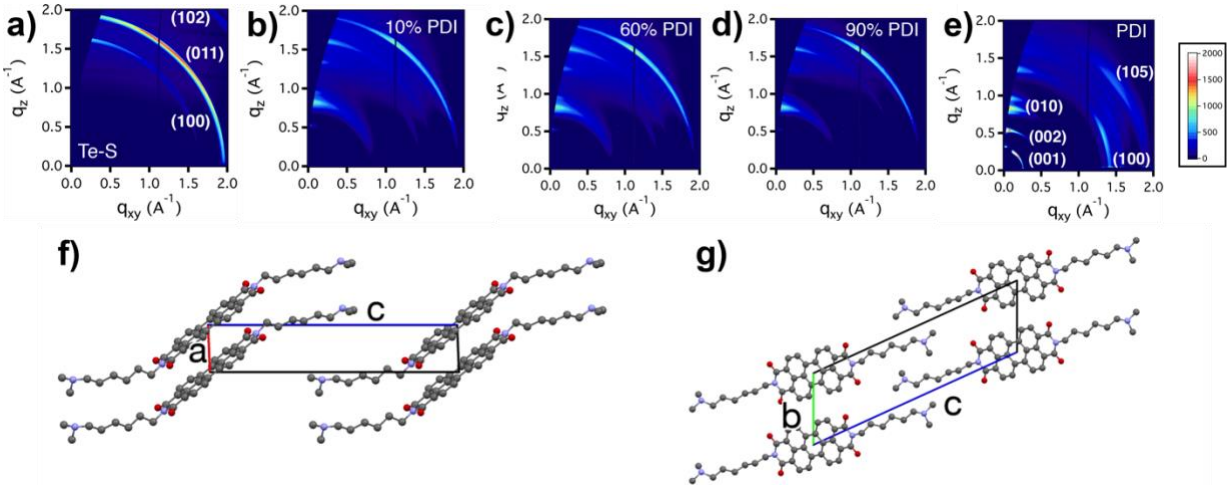

Figure 6.4 Two-dimensional GIWAXS performed on solid films of a) Te-S complex, Te-PDI composites of varying composition prepared via Method A ((b) – (d)), and e) pure PDI. In the low PDI regime, the GIWAXS spectra are dominated by the signal of the hexagonally packed Te crystal lattice. In the high PDI regime, the GIWAXS spectra feature peaks at lower q values corresponding to molecular packing and longer order organization of the PDI small molecules. The 2D GIWAXS data for pure PDI is used to solve the molecular crystal structure. (f, g) Packing of PDI molecules into a unit cell is viewed along (f) the b-axis and (g) the a-axis. For ease of 3D visualization, an animation of the unit cell rotating is included in the Supporting Information of the original published material.[206]

In the 2D GIWAXS spectrum (Figure 6.4e), the highest intensity peak is identified to be the (001) reflection, with a higher order (002) reflection clearly visible. The (001) peak represents the largest-scale molecular ordering in these films, with a periodicity of 26.0 Å, which has been attributed to the end-to-end distance across the long-axis of the PDI molecules (Figure 6.4f). Due to the tendency of the C_6 side chains to protrude from the PDI core at an angle (~48°) and entangle via hydrophobic effects, this length scale is smaller than the end-to-end length of a fully extended PDI molecule (33.1 nm), similar to the observations made by Klebe et al. These peaks are anisotropically observed near the meridian (close to q_z), indicating a tendency to stack through-plane. Additionally, we observe slipped π-π stacking of these molecules, at an angle of 56.5° from the (001) plane. This corresponds to a 47.8° in reciprocal space, which matches the location of the (105) peak (π-π stacking direction) on the 2D GIWAXS detector. The similarities between our solution and those previously reported for molecules in this class of materials, as well as the

agreement between the calculated and observed peak locations (both q values and positions on the 2D detector) provide further evidence for the fitness of our solution.

Table 6.1 Unit cell parameters calculated for PDI crystal structure. The PDI crystallites exhibit triclinic structure with Z = 2 molecules per unit cell.

a (Å)	**b (Å)**	**c (Å)**
4.48	8.33	26.0
α	**β**	**γ**
65.4°	86.6°	86.8°

GIWAXS spectra taken for S-Te NW thin films (Figure 6.4a) depict the expected hexagonal structure previously reported in a similar system (ICDD - PDF-4 #04-016-1605).[25] We note that the (100) peak is observed primarily near the meridian, and thus that the corresponding (100) plane is oriented primarily through-plane. Composite films of varying PDI content were also studied using GIWAXS (Figure 6.4b-d). Note that, in the moderate to low PDI regime, the Te (011) peak is convoluted with the PDI (105) peak. Of greatest import are the GIWAXS patterns observed for hybrid films in the high PDI regime, as this is the regime that demonstrates maximum thermoelectric performance. Interestingly, comparing the GIWAXS pattern for 100% PDI thin films to the 98% and 90% composite PDI-Te films reveals a shift in the peak of highest intensity. In pure PDI films, the (001) reflection is the most intense, whereas in the composite films, the (010) plane is dominant. This indicates a reorganization of PDI crystals on the Te surface relative to a bare substrate, likely tied to the increase in mobility implicated in the composite samples. In such a regime, the PDI π stack would tend to align along the surface of the inorganic nanostructure, likely leading to regions of high conductivity at the organic-inorganic interface. This result suggests that having a smooth, pristine inorganic surface onto which the PDI molecules can be templated during the PDI-Te composite formation is a critical component to producing high conductivity hybrid materials.

Further, it is possible to estimate the correlation length in the PDI crystallites using the Scherrer formula:

$$l = 2\pi K/\Delta q$$

where the Scherrer constant (K) is taken to be ~0.9 and the correlation length (l) is calculated from the observed peak broadening (Δq).[111] In this way, we estimate the correlation length of PDI in thin films of 100%, 98%, and 90% PDI to be 84.5 Å, 183 Å, and 170 Å, respectively. The high conductivity PDI-Te composites demonstrate greater than twofold increase in correlation length. Again, the inorganic surface seems to play a role in templating larger crystalline domains of PDI at the organic-inorganic interface than are achieved in pristine PDI films. This result further corroborates the conclusion that structural reorganization of PDI molecules in the PDI-Te composites is tied to increasing thin film apparent electron mobility and thus thermoelectric performance of the hybrid system.

6.3.4 Composite Electronic Structure

Measurement of the work function (WF) and ionization energy (IE) for PDI-Te composites provides an important probe to understand the source of the high Seebeck coefficient observed in

the hybrid nanostructures in the low PDI regime. For this goal, ultraviolet photoelectron spectroscopy (UPS) was performed on thin films of varying PDI content; the results are summarized in Table 6.2, while the relevant spectra are depicted in Figure 6.10. Additionally, the optical band gaps of Te-S and PDI are calculated from Tauc plots (Figure 6.11) to provide further details on the electronic structure of these materials. The Te-S complex has a WF within the narrow band gap and located near the conduction band, as expected in an *n*-type semimetal. Pure PDI and the 90% PDI composite are shown to have a similar WF, although the band gap is much larger in PDI than Te, as is typical with HOMO-LUMO gaps in organic semiconductors. The 10% PDI complex has the greatest work function, in line with the EPR findings of relatively low carrier concentrations in the low PDI loading regime and corroborated by XPS results (Figure 6.12). This implies that the increase of Seebeck values measured in this low PDI regime are the result of dedoping of the system, likely due to localization of previously mobile carriers during formation of the composite.

Table 6.2 Work function (WF) and ionization energy (IE) for PDI-Te composites with varying PDI content prepared via Method A, as determined by UPS.

	WF (eV)	IE (eV)
S-Te (0% PDI)	3.7	4.1
10% PDI	4.2	4.5
90% PDI	3.7	4.2
100% PDI	3.8	4.3

6.3.5 Design of High-Performing PDI-Te Composites (Method B)

Using sulfur linkers (Method A) in preparing the PDI-Te composites provides an intuitive and flexible approach to the design of hybrid materials. Structural analysis of these materials reveals that the key to the improved thermoelectric performance observed in these materials is a templating effect, where the packing of PDI molecule is altered due to the presence of the inorganic nanostructure, likely due to an interaction between PDI molecules and the Te surface. This leads to a reorganization of PDI molecules in the hybrid films, as well as increased crystalline domain lengths. However, XPS reveals that much of the polyvinylpyrrolidone (PVP) ligand used in the original Te NW synthesis (Method A) is not removed during the S exchange process (Figure 6.13). In order to promote templating of PDI molecules on the Te nanowire surface, it is desirable to have intimate contact between the organic and inorganic phases. Any residual PVP ligand and S linkers on the Te nanowire surface will likely reduce the surface area available for strong interaction between PDI and the Te surface, dampening the templating effects. Additionally, PVP and the S linkers are both electronic insulators, potentially reducing the electrical conductivities that can be achieved in films synthesized using this method. Driven by these conclusions, we demonstrate a second ligand exchange approach (Method B), in which much of the PVP ligands are removed via a stripping method, and PDI is coated directly onto the bare Te surface in a single-step procedure. Hydrazine hydrate was chosen as the stripping agent following literature precedent.[207,208] Hydrazine hydrate is a good candidate for this method because it is known to 1) efficiently strip hydrocarbon ligands from the surface of nanoparticles without altering the nanoparticle size or shape, 2) act as a strong Lewis base to saturate any dangling bonds at the surface of the nanoparticles, 3) act as a reducing agent to repair any oxide defects at the nanoparticle surface,

and 4) act as a Brönsted base to prevent ionized free ligands from reattaching to the nanoparticle surface.[208,209] Additionally, unlike the toxic and explosive anhydrous hydrazine, hydrazine hydrate procedures can be executed with minimal health risks in a standard fume hood. This procedure is used to enhance the templating effect of PDI on the Te surface, minimize the presence of insulating PVP and S moieties in the films, and simplify the composite preparation procedure from multi-step to a single-step process. TGA is used to confirm the removal of the majority of the hydrocarbon ligands from the Te nanowire surface (Figure 6.14).

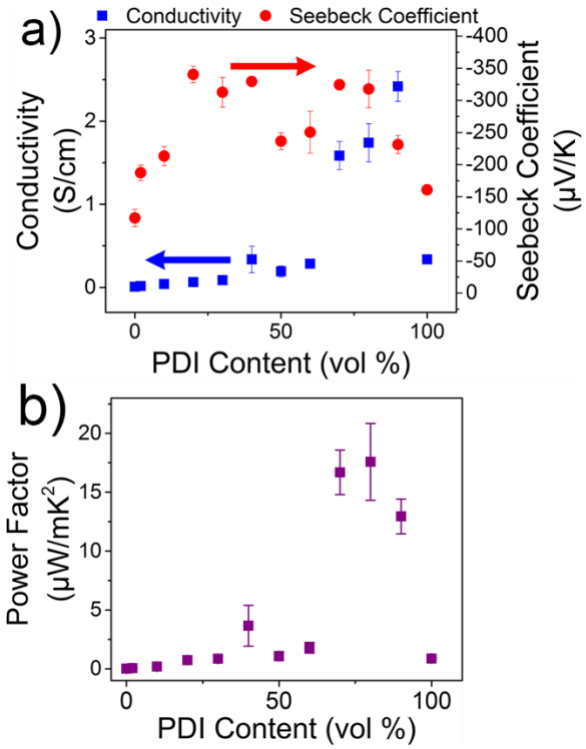

Figure 6.5 Thermoelectric transport properties measured for Te-PDI composites formed via hydrazine stripping, Method B. (a) Similar non-monotonic trends are observed in both Seebeck and electrical conductivity, implying that this technique provides a simplified, one-step route to make Te-PDI nanostructures with similar properties. (b) Power factors achieved in this system are significantly greater than those in Method A, demonstrating up to 20x improvement in performance from pure PDI and three orders of magnitude improvement from the pure inorganic nanostructure.

The composites prepared using Method B exhibit significantly improved electronic conductivity, demonstrating power factors up to 20 times greater than pure PDI and three orders of magnitude greater than the pure inorganic nanostructure (Figure 6.5). We note that the PDI-Te composites in the high PDI regime also achieve greater Seebeck coefficients than those composites prepared via Method A. The Seebeck coefficient is a complex function of several variables, including the carrier concentration, mobility, and density of states. Hydrazine hydrate treatment is known to alter the energetic landscape available to carriers at the organic-inorganic interface via reduction of oxide defects and filling of trap states, which likely contributes to the complex Seebeck coefficient trends observed. XPS spectra suggest stronger electronic coupling between the Te and PDI domains in composites prepared via Method B (Figure 6.15). This result supports the conclusion that the interaction between organic molecules and inorganic nanostructure surfaces play a key role in the

performance of hybrid thermoelectrics. Furthermore, this result showcases the potential of our methods and materials for preparing air stable, flexible *n*-type thermoelectric inks with high thermoelectric performance. Such materials are amenable to a host of solution-based processing techniques, enabling a variety of new thermoelectric device designs, from 2D printed arrays to 3D flexible architectures. We provide proof of principle for this approach by demonstrating power generation in a flexible thermoelectric energy generator (TEG) using only our hybrid thermoelectric inks.

6.3.6 Fabrication of Ink-Based Flexible Thermoelectric Generator

In order to test the viability of our all-solution-based approach, it is imperative to demonstrate realistic thermoelectric power generation in addition to measuring material properties. Here, we present the fabrication and characterization of flexible TEGs using a novel geometric design and facile, low-temperature solution-based techniques (detailed fabrication methodology provided in experimental section). Using a 10-leg device, the maximum power density generated was as large as 57 nW/cm^2 (Figure 6.6d) under a small temperature gradient (50K). This result is comparable to power generated in other flexible, soft material systems using only low temperature/low pressure solution-based techniques.[53,144,191] Mechanically, these devices demonstrated robust stability during flexing. The folded "stacked" geometry requires each leg to be flexed at both contact points. Traditional thermoelectric materials typically suffer from cracking or delamination in such geometries, whereas an all-ink design improves mechanical versatility and resiliency. Additionally, this design is modular in nature, and allows for simple modification of the number of legs connected in series. Thus, our approach enables new thermoelectric architectures for flexible power generation with low processing costs. This result represents a significant and promising proof-of-principle for all-ink, solution-processed flexible thermoelectrics.

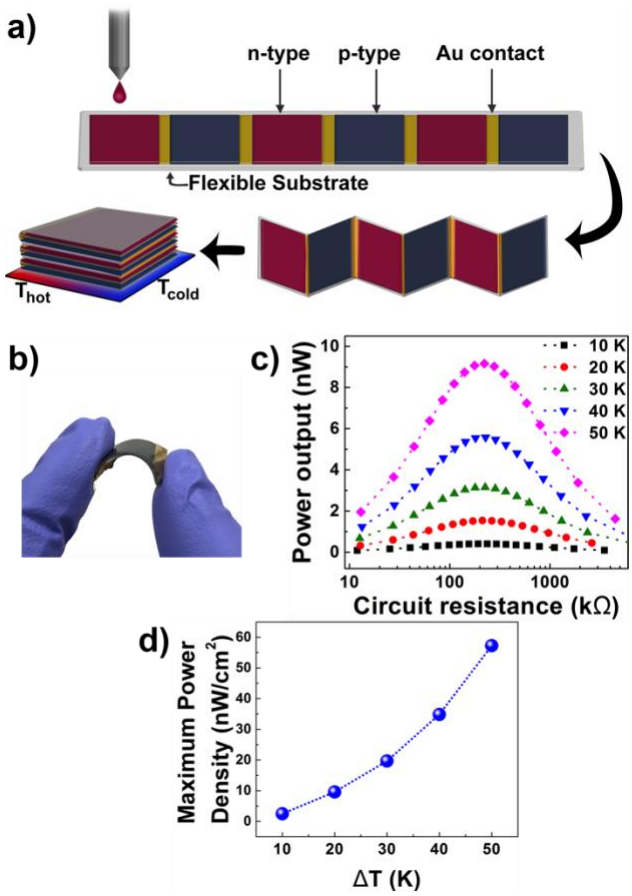

Figure 6.6 Flexible thermoelectric module design and performance. a) Using solution printing, a linear thermoelectric device is patterned onto a flexible substrate, which is then folded into a compact "stacked" structure. b) Photograph of 10-leg stacked TEG module demonstrating flexibility. c) Power density is measured as a function of load resistance at a variety of applied temperature gradients. d) Maximum power density observed is reported as a function of applied temperature gradients.

6.4 Conclusions

To summarize, we have successfully demonstrated the preparation of novel *n*-type soft thermoelectric hybrids with high performance using PDI small molecules. We report the first explicit solution to the crystallographic structure of the PDI molecules in thin films, shedding new light into the relationship between structure and performance within this material class. Leveraging this new molecular-level insight, a second methodology is developed to prepare PDI-Te hybrid materials. Power factors as great as 17.6 $\mu W/mK^2$ are achieved in this system, representing up to twenty-fold improvement in thermoelectric performance over the pure PDI thin films. Detailed study of the energetics in this material system reveals that this phenomenon is the result of enhanced carrier mobilities, associated with the reorganization of the PDI molecules on the surface of the Te nanowires. This work provides strong evidence that ligand templating on inorganic nanostructures plays a crucial role in the electrical and thermoelectric transport of hybrid materials, marking the first experimental observation of this templating effect and corroborating recent theoretical work in the literature. This result adds critical insight into the mechanism of high performance in hybrid thermoelectric materials, a subject still under strong debate. Finally, we

report the fabrication of all-ink thermoelectric generators with impressive flexibility using a novel folded architecture. Since these materials use exclusively low temperature, facile solution processing, this approach represents a significant advantage for next-generation printed electronic devices.

6.5 Experimental

6.5.1 Materials

Tellurium dioxide (99.9995%), polyvinylpyrrolidone (PVP, average molecular weight 55 kDa), sodium hydroxide (ACS reagent, ≥97.0%, pellets), ethylene glycol (ReagentPlus®, ≥99%), hydrazine hydrate (78-82%, iodometric), sodium sulfide, and methanol (reagent grade, 98%) were purchased from Sigma Aldrich. Acetone (J.T.Baker®) and isopropyl alcohol (ACS grade) were purchased from VWR International. Ion exchange resin (Dowex Monosphere 550A hydroxide form, Sigma Aldrich) was used to run a PDI counterion exchange column.

6.5.2 Composite Synthesis

Synthesis of PVP capped Te nanowires (PVP-Te NWs) and surface exchange to sulfur capped Te nanowires (S-Te NWs) followed existing literature procedures with slight modification.[109,111,195,210] Synthesis of PDI molecules and counterion exchange to hydroxyl have been previously reported. PDI capped Te nanowires (PDI-Te NWs) were prepared via two ligand-exchange methods, Method A and Method B (details below). In both methods, PDI-Te NW solutions were then washed 3 times in methanol (9000 rpm, 45 min) to ensure a clean product of PDI capped nanowires. During washing, the supernatant was yellow in hue, indicating removal of unbound PDI moieties. Finally, PDI-Te NWs were redispersed in water at a concentration of 20 mg/mL. The resulting solution is lustrous and silver, with a visible reddish hue indicative of the presence of PDI moieties on the surface of Te nanostructures. TEM was used to visually confirm the presence of an organic PDI layer on the Te core, and to verify that the NWs maintain a high-quality inorganic core of single crystalline Te (Figure 6.1c-e). XPS scans show a shift in the binding energy of the S 2p core levels upon addition of PDI, suggesting that the sulfur linkers interact electronically with the organic phase in the binding process (Figure 6.16). These PDI-Te NWs were then used to prepare thin films. To prepare PDI loading ladders, PDI-Te NWs were mixed with varying amounts of additional PDI solution. It is important to note that capping the Te NW with PDI is crucial to the preparation of high-quality composite films. Simply using a physical mixture of Te NWs and PDI results in phase separation, an indication of weakly interacting organic and inorganic phases. SEM illustrates the film-level organization (Figure 6.17).

Method A: In the first method, sulfur (S) is used as a linker molecule to mediate binding between the Te and PDI domains (Figure 6.1a). In a typical reaction, 500 mg of precipitated S-Te NWs were collected, to which 5 mL of PDI solution (2 mg/mL in water) was added, and the mixture was then briefly vortexed followed by redispersion in 15 mL methanol.

Method B: In this method, hydrazine hydrate was used to partially strip the surface of PVP-Te NWs, destabilizing the nanostructures and allowing PDI to be directly coated onto the bare Te surface. In a typical reaction, 1.5 mmol of hydrazine hydrate were added to 200 mg of PVP-Te (concentration of 5 mg/mL) under vigorous stirring. The ligand stripping reaction was carried out

for 30 minutes. If the reaction is allowed to progress too long (~ 40 min), over-stripping of surface ligands will destabilize the nanostructures and cause the Te to crash out of solution. Afterwards, the mixture was washed to remove hydrazine and unbound PVP (9000 rpm, 20 min). 1 mL of PDI solution (2 mg/mL in water) was added to the precipitate, and the mixture was then briefly vortexed followed by redispersion in 15 mL methanol.

6.5.3 Thin Film Preparation

Thin films were prepared via drop casting on glass substrates (9.5 mm x 9.5 mm, 1 mm thick – Thin Film Devices). Substrates were pre-cleaned via sonication in three successive solvents, Millipore water, acetone, and isopropanol, followed by nitrogen drying and UV-ozone treatment for at least 10 minutes. Clean substrates were placed on a large aluminum block acting as a thermal reservoir at 85°C, and 75 μL of composite nanoparticle solution was drop cast onto the substrates. Films were partially covered to control evaporation and dried in this manner until all solvent had been removed (20-30 min).

Gold contacts for electrical measurements (100 nm thickness) were patterned onto each of the four corners of the dropcast films via thermal evaporation using a shadow mask. Identical experiments were carried out using bottom contacts (100 nm gold), but these samples demonstrated poor electrical contact in hybrid films with high inorganic loading. Cast films were annealed on a hot plate inside a nitrogen glovebox at 120°C for 20 min before measurement and characterization. In previous reports on these PDI materials, annealing was shown to significantly improve the thin film electrical conductivity via a self-doping mechanism.[109] Quaternary ammonium cations are present on the PDI side chains in solution, which are converted to tertiary amines during the annealing process, which then act as powerful *n*-doping motifs coupled to the PDI core. The improved electrical conductivity and power factors after annealing was confirmed by measurement of PDI-Te thin film thermoelectric properties before and after the annealing step (Figure 6.18).

6.5.4 Electrical and Thermoelectric Measurements

Sheet resistance of each film was measured using Keithley 2400 Sourcemeters in 4-wire van-der-Pauw configuration. Film thickness was measured by scratching the film and measuring the step height with a Veeco Dektak 150 profilometer. Electrical conductivity was extracted from the sheet resistance and thickness measurements.

Seebeck coefficient (thermopower) was measured using a homemade probe setup. Two Peltier devices (Ferrotec) were placed ~4mm apart and a single current was passed through them in opposite polarities. This caused one device to heat and the other to cool approximately the same amount relative to room temperature. The sample was placed across these two devices such that a thermal gradient was established (thermal paste was used to ensure thermal contact – Wakefield Thermal S3 Solutions), and the resulting open circuit voltage was measured using an Agilent 34401 multimeter. The temperature gradient was measured using two T-type thermocouples mounted in micromanipulators. The magnitude of the temperature gradient is directly correlated to the amount of current driven through the Peltier devices. Typically, five different gradients were established (allowed to equilibrate for 200 seconds between temperature changes), with 10 voltage measurements taken and averaged at each ΔT. All samples exhibited linear variation of open circuit voltage with ΔT; this trend was used to extract Seebeck coefficient values. Data for both

electrical conductivity and Seebeck coefficient were acquired using homemade Labview programs. For each measurement, at least three different samples were measured and averaged, with error bars representing standard error. Ohmic contacts were confirmed before measurements. Hall mobilities were measured using an Ecopia HMS-5000 Variable Temperature Hall Effect Measurement System. Air stability measurements were also performed on the Ecopia system. PDI-Te hybrid films were prepared via Method A, and Te films were prepared via identical methodologies but without the addition of PDI. Both films were stored in ambient conditions and the conductivities were measured twice a day for 12 days. The air stability of the PDI-Te composite films appears to be significantly improved over films without PDI (Figure 6.19).

6.5.5 Characterization of PDI-Te NWs and Thin Films:

High resolution imaging of nanostructures and selected area electron diffraction (SAED) were acquired on a JEOL 2100-F Field-Emission Analytical Transmission Electron Microscope (TEM) at an accelerating voltage of 200 kV. TEM samples were prepared on grids of 400-mesh Cu or Ni on holey carbon (Ted Pella 01824). Thin film imaging was performed on a Zeiss Gemini Ultra-55 Analytical Field Emission Scanning Electron Microscope (SEM) using a beam energy of 5 kV. Thermogravimetric analysis (TGA) was performed on a TA Instruments Q5500 TGA to quantify organic-inorganic composition of each sample. 7-10 mg of each sample was ramped to 600°C at a scan rate of 5°C/min and held there for 120 min. The weight lost was assumed to be the organic content of the hybrid, and the remaining weight was taken to be the inorganic content.

Spin quantification was performed at room temperature using Electron Paramagnetic Resonance (EPR) on a Varian E109 EPR spectrometer equipped with a Model 102 Microwave bridge. The following spectrometer conditions were used: microwave frequency: 9.22 GHz; field modulation amplitude: 32 G at 100 kHz; microwave power: 20 mW. Quantification was performed according to existing literature standards using the stable free radical 1,1-diphenyl-2-picrylhydrazyl (DPPH) as a standard.[109,198–200] Samples and standard were dropcast onto quartz microscope cover slides and cleaved into pieces roughly 2-4 mm in dimension. Samples were inserted into quartz EPR tubes and sealed with vacuum grease and plastic caps. Triplicates were measured at every PDI loading level analyzed. All samples and standards were measured within 4 hours of preparation. Spin quantities were determined by comparing the EPR signals from PDI-Te samples to those of the DPPH samples with known spin quantities using the following equation:

$$\frac{N_1}{N_2} = \frac{\left(a \times \Delta H_{pp}^2\right)_1}{\left(a \times \Delta H_{pp}^2\right)_2}$$

where a is the peak-to-peak derivative amplitude and ΔH_{pp} is the peak-to-peak line width. Profilometry was used to measure film thickness to calculate per volume spin concentrations.

2D Grazing-incidence wide angle x-ray scattering (GIWAXS) was performed at the LBNL ALS on beamline 7.3.3 with an area detector, a camera length of ~25-30cm, and an incident energy of 10 keV. Films were typically exposed for 60 s at an incidence angle of 0.10°. Acquired images were normalized with a AgB standard.

X-ray and ultraviolet photoelectron spectroscopy (XPS and UPS) were performed on a Thermo K-Alpha Plus instrument with a monochromatic Al X-ray source. For high resolution scans, the pass energy was set to 20 eV and the energy resolution to 0.1 eV. UPS was performed using an He I

source at 21.2 eV. Thin film surfaces were cleaned using an Ar cluster gun (6000 eV/cluster, 150 atoms/cluster, 15 sec) before all UPS experiments.

UV-vis-NIR spectroscopy was performed on a Cary 5000 instrument in absorbance mode with a range of 190-3300 nm.

6.5.6 Thermoelectric Module Design and Performance:

Thermoelectric generators were prepared simply using solution-based techniques and a novel, modular design (Figure 6.20). A flexible PET (polyethylene terephthalate, 0.0005" thickness – McMaster-Carr) substrate was patterned with gold electrodes (100 nm thick) using thermal evaporation. The substrates were then UV-ozone treated to improve hydrophilicity followed by drop casting of the hybrid thermoelectric inks at 75°C. On a single substrate, 3-4 *p*-*n* couples were deposited to form a thermoelectric module, and several modules were connected in series to form a thermoelectric device with the desired number of *p*-*n* legs. The modules were then folded along the gold electrodes to produce a thermoelectric generator (TEG) with a stacked geometry (Figure 6.6, 6.15). For the *n*-type leg, the PDI-Te nanowire composite was used, while for the *p*-type leg, a well-studied PEDOT:PSS-Te nanowire composite was used.[8–10] The *p*-type material was chosen due to its analogous inorganic nanostructure, ease of synthesis, high thermoelectric performance, and air stability. The TEG was then suspended across two hot Peltier devices and connected to a Keithley 2400 Sourcemeter. Each Peltier was operated separately to produce thermal gradients ranging from 10 to 50 K. At a given temperature gradient, the sourcemeter was used to apply varied electrical currents and measure the resulting module resistances. These measurements were used to identify the optimal operating condition at each temperature gradient and to calculate the maximum power generated there. All measurements were performed in air.

6.6 Acknowledgements

This work was performed at the Molecular Foundry and Advanced Light Source, Lawrence Berkeley National Laboratory, and was supported by the Department of Energy, Office of Science, Office of Basic Energy Sciences, Scientific User Facilities Division of the U.S. Department of Energy under Contract No. DE-AC02-05CH11231. EWZ and MPG gratefully acknowledge the National Science Foundation for fellowship support under the National Science Foundation Graduate Research Fellowship Program. The authors would like to acknowledge Professor Craig Hawker and Dr. Brenden McDearmon, supported by NSF DMR 1436263, for the PDI synthesis reported in this paper.

6.7 Supporting Information

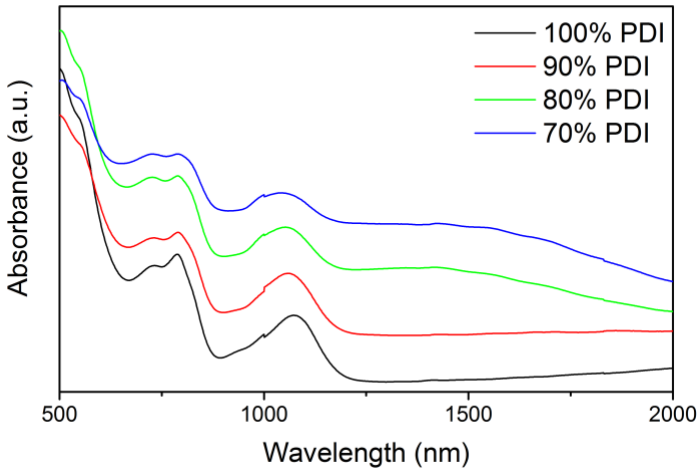

Figure 6.7 UV-vis spectra of thin films of Te-PDI hybrid nanostructures with varying PDI content. All spectra depict characteristic polaron peaks (~730 nm, 800 nm, 1100 nm), consistent with previous literature. Peak broadening is observed as the PDI content is reduced, which is attributed to increased carrier mobility and intermolecular interaction, in line with the evidence provided by GIWAXS and EPR. It is important to note the lack of bipolaron absorption between 1250 and 2000 nm.

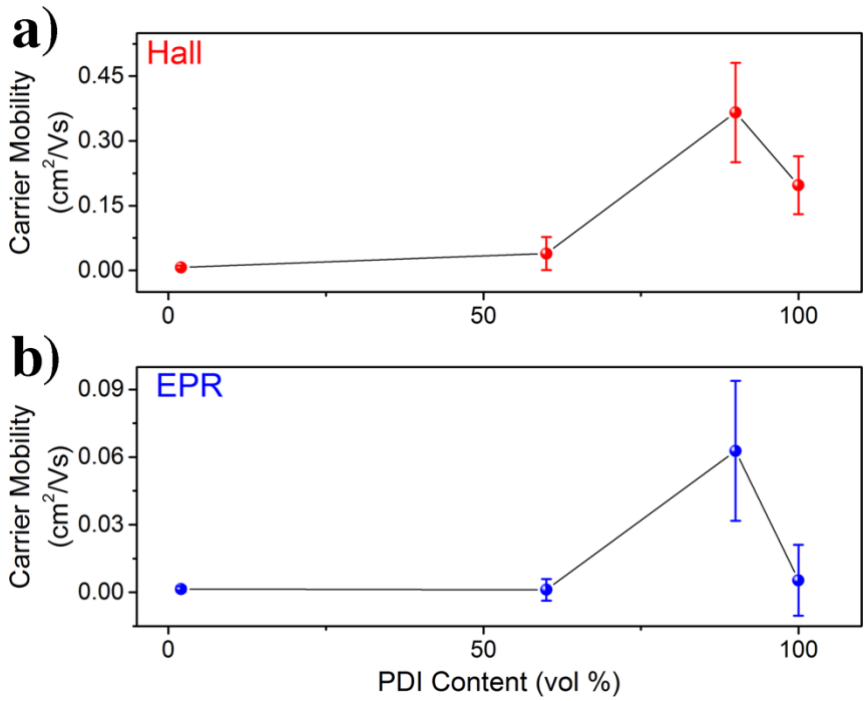

Figure 6.8 Carrier mobilities (a) measured via the Hall effect and (b) extracted from EPR and room temperature conductivity measurements. Both sets of data indicate a peak in the high PDI regime, coincident with the peak in electrical conductivity observed the PDI-Te thin films. While

bipolar transport and energetic disorder is expected to cause the Hall approach to overestimate mobilities in this system, the qualitative agreement of both independent approaches corroborates the conclusion that enhanced mobility in the high PDI regime is responsible for improved thermoelectric performance in these hybrid films.

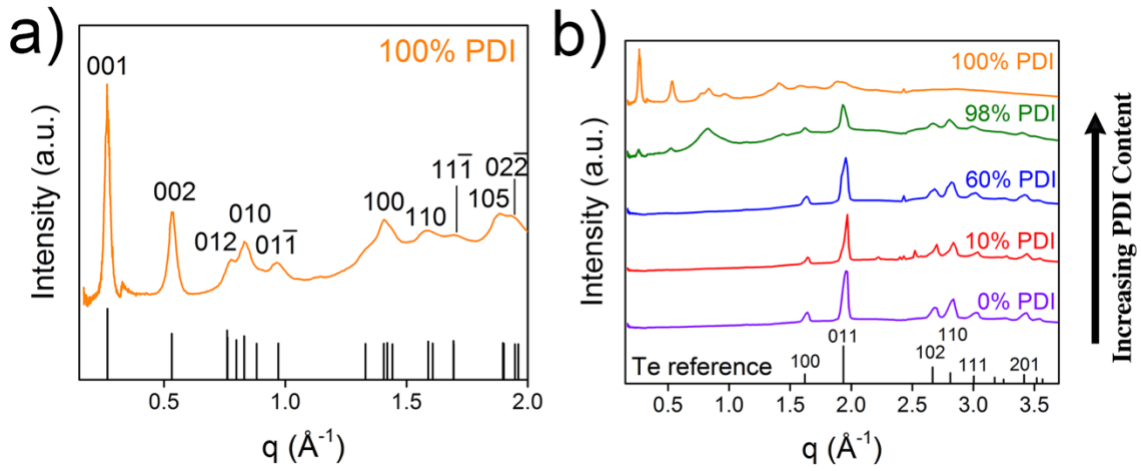

Figure 6.9 GIWAXS data used to characterize morphology of Te-PDI composites. a) Radially integrated GIWAXS profile of 100% PDI film was used to solve for the PDI crystalline structure. A simulated diffraction pattern based on our reported solution is included as black lines at the bottom. b) Radially integrated GIWAXS profiles are shown here for PDI-Te composites of varying composition. At low PDI loading, the high intensity features clearly match the reference spectrum for Te (ICDD - PDF-4 #04-016-1605). In the high PDI regime, the spectra include both Te peaks and peaks stemming from organization of PDI molecules.

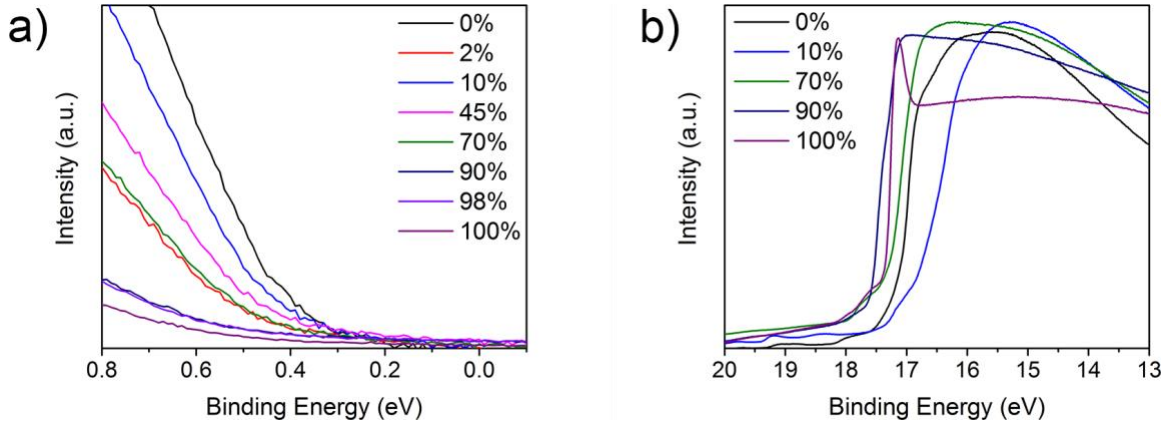

Figure 6.10 Ultraviolet photoelectron spectroscopy was used to probe the energetics of Te-PDI composites. Depicted here are a) The valence band/HOMO onset region and b) the secondary electron cutoff (SECO) region. The UPS spectra were used to identify work functions and IE for Te-S NWs, pure PDI, and Te-PDI composites with varying PDI content. The important results are summarized in Table 6.2.

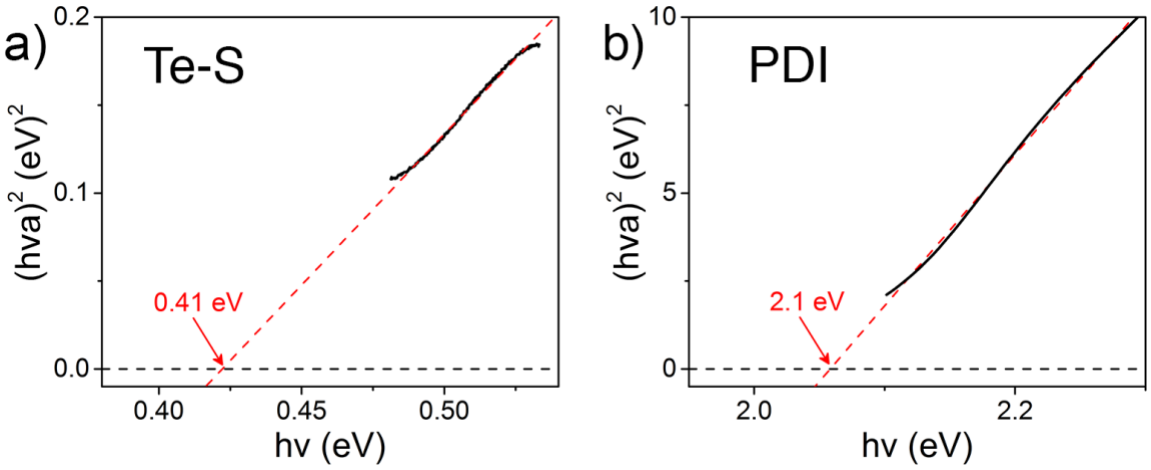

Figure 6.11 Tauc plots used to calculate optical bandgap of both phases: a) pure Te-S and b) PDI. Here, *h* is Planck's constant, ν is the light frequency, and *a* is the absorption coefficient of the material. Te-S shows a narrow and direct bandgap, as expected, and the wider band gap in PDI is consistent with typical HOMO-LUMO gaps in organic semiconductors.

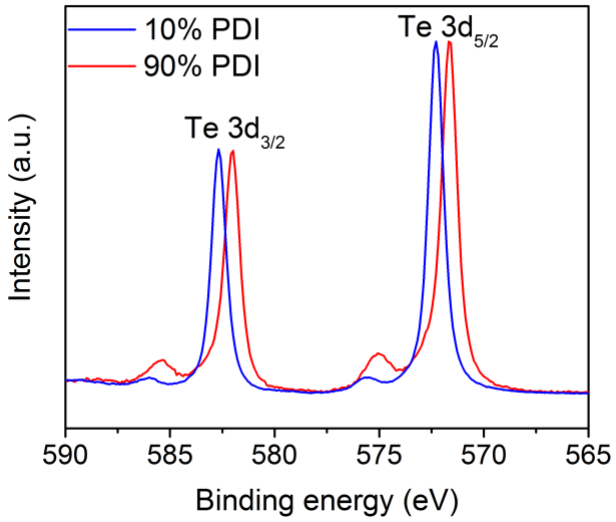

Figure 6.12 Te 3d XPS scans at low PDI content and high PDI content reveal a shift in the peak location. In low PDI films, the Te peak shifts to higher binding energies, implying a decrease in electron density in the inorganic phase. This corroborates the EPR and UPS results showing increased carrier concentration in high PDI composites and implicating a dedoping effect in the low PDI composites.

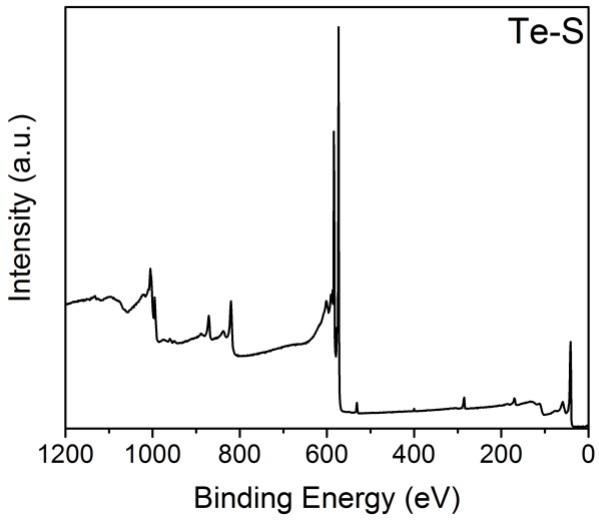

Figure 6.13 XPS survey scan of Te-S nanowire complex before addition of PDI reveals strong C and N signals, indicating that significant PVP ligand remains on the nanowire surface along with the S linkers.

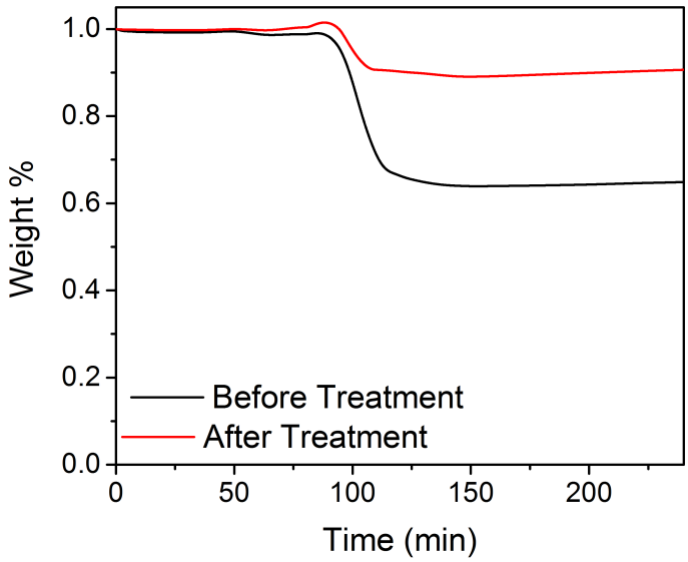

Figure 6.14 TGA is used to quantify the organic-inorganic composition of the Te nanowires before and after hydrazine hydrate treatment. The temperature of the composite is ramped to 600°C and held there, and the weight loss is taken to be the amount of organic material present in the composite. After treatment, the amount of organic material is significantly reduced, indicating that the hydrazine hydrate treatment successfully removes the majority of the surface ligand from the nanostructure.

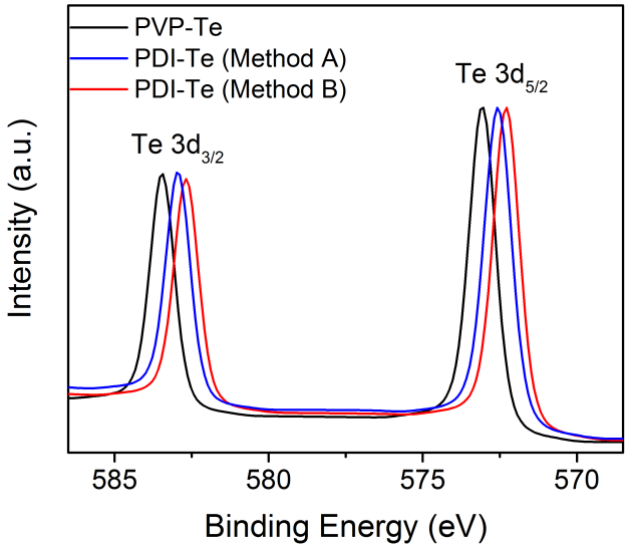

Figure 6.15 XPS was used to investigate and compare the interaction between PDI and Te in the composites prepared via Method A and B. Here, XPS spectra of the Te 3d orbitals of 1) as-synthesized PVP-Te NWs, 2) PDI-Te composites prepared via Method A (with S linkers), and 3) PDI-Te composites prepared via Method B (without S) are depicted. These spectra reveal a shift in the peak location of both PDI-Te composites relative to the PVP-Te control, suggestive of electronic coupling and charge transfer between the Te and PDI domains. Moreover, the magnitude of this shift is greater for the PDI-Te composites prepared via Method B, indicating that the electronic coupling is likely stronger in the composites without S. Note that the PDI-Te composites measured here are both at 10% PDI.

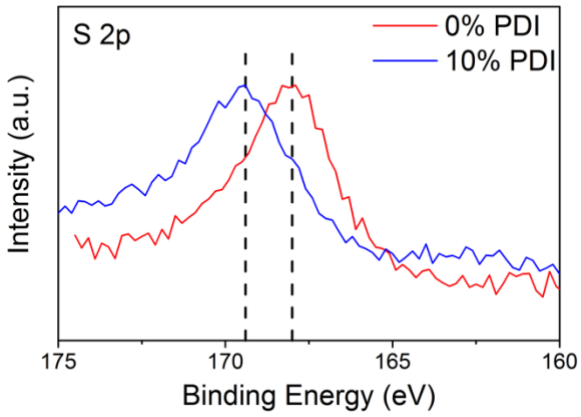

Figure 6.16 XPS experiments implicate sulfur linker in binding and in Te-PDI hybrid nanostructures. High resolution scans of the S 2p core levels reveal a shift to higher binding energy in the 10% PDI sample relative to the 0% Te-S complex. This corresponds to a decrease in electron density around the S linker molecules, indicating that the linker interacts electronically with the organic and inorganic phases.

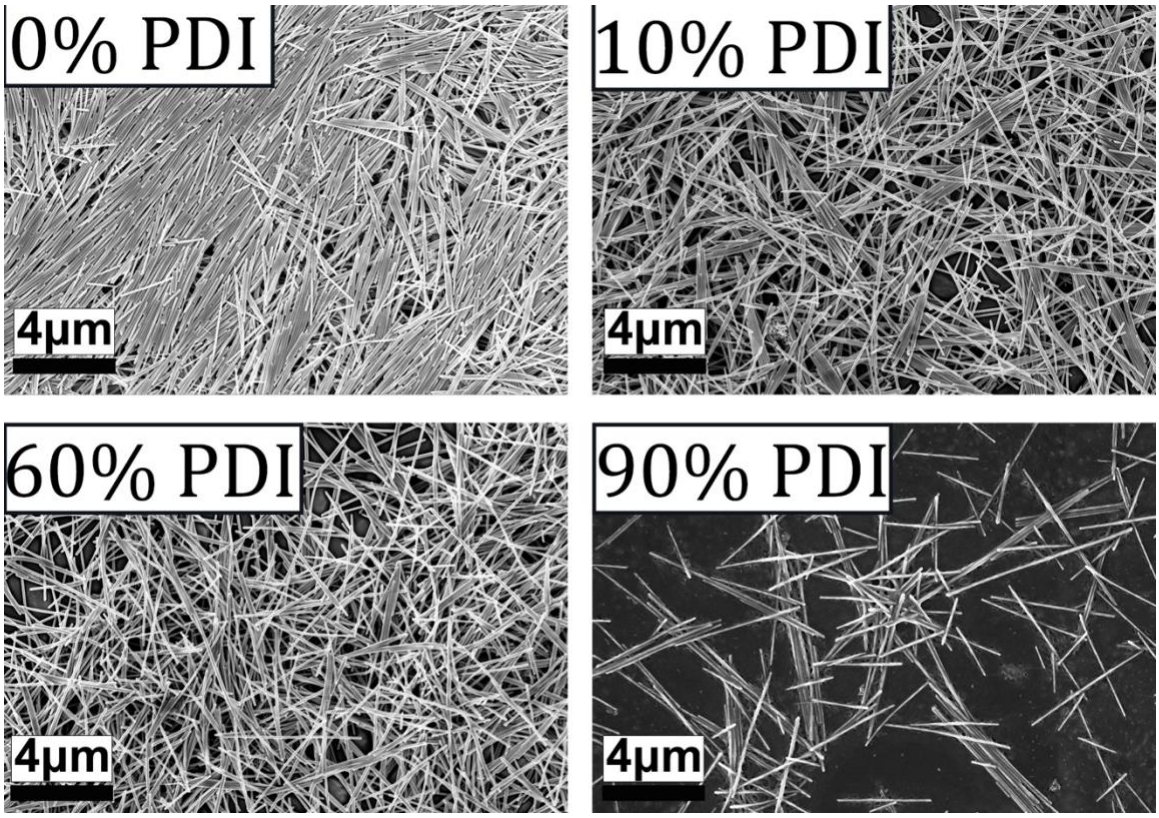

Figure 6.17 SEM images of Te-PDI films with varying PDI content show tellurium nanowires embedded in organic PDI matrix as expected. These micrographs give a sense for film-scale organization of the composite materials, which is important as all thermoelectric properties are all measured at the film level. Nanowires are primarily oriented in-plane with some wire-wire packing resulting in anisotropic transport.

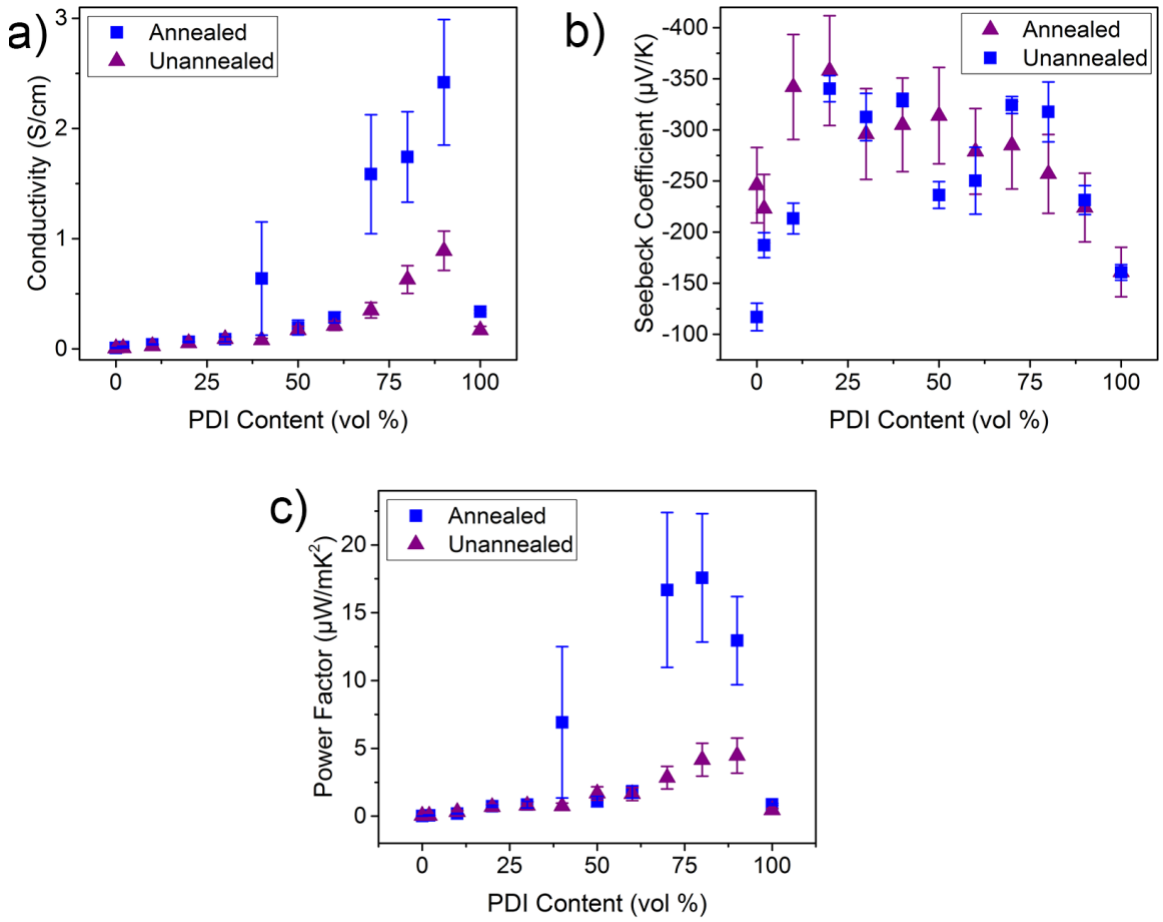

Figure 6.18 Thermoelectric properties were measured for Te-PDI nanostructured prepared via 1-step hydrazine stripping then ligand replacement. Performance of annealed films are compared with that of unannealed films to confirm optimized film processing steps suggested by literature.

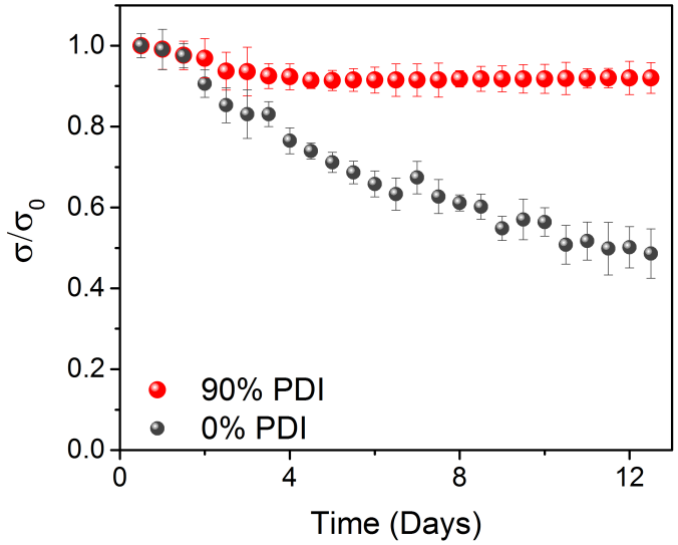

Figure 6.19 The air stability of PDI-Te composites is evaluated by measuring the decay in electrical conductivity over the course of 12 days, during which time the films were stored and

measured in ambient conditions. The film without PDI experiences significant decay in conductivity over the course of the experiment, while the PDI-Te composite (90% PDI) exhibits more stable behavior. It is likely that the Te film, without the presence of the protective PDI layer, is prone to oxidation in air.

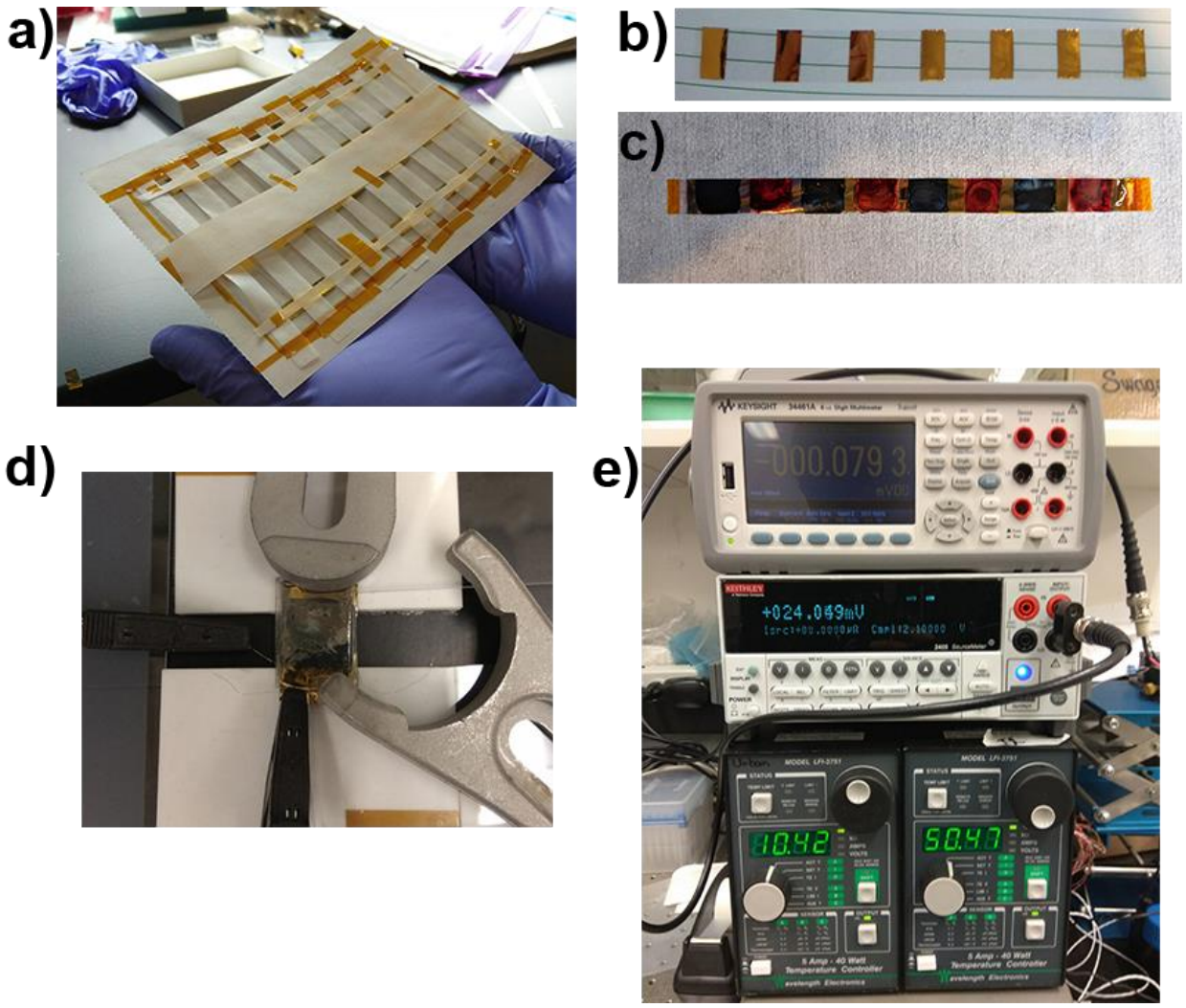

Figure 6.20 Preparation and measurement of flexible thermoelectric generator. a) Mask applied to bare PET substrate in order to deposit gold contacts via thermal evaporation. b) PET substrate with gold contacts before deposition of thermoelectric inks. c) 4-leg thermoelectric module after deposition of thermoelectric inks. Dark blue regions are *p*-type PEDOT:PSS-Te NWs and red regions are *n*-type PDI-Te NWs prepared via Method B. d) The folded thermoelectric generator stack is suspended across two Peltier devices and connected electrically to a power generation/measurement setup. e) Photograph of temperature controllers and sourcemeters used to perform thermoelectric power generation measurements.

Chapter 7. Conclusions and Future Outlook

The field of soft thermoelectrics is one rich with opportunity for a diverse group of scientists – essential challenges remain in the basic chemistry, engineering, modeling, and transport physics. STEs are compatible with diverse new commercial applications, and they are especially relevant in light of the rising interest in IoT and wearable electronics. Even at the very root of this field, there are a number of high-value open questions regarding the physics of carrier transport in organic and organic-inorganic thermoelectric systems. Remarkably, even in many of the most well-studied systems it remains the case that we do not know the specific energy carriers responsible for the measured property values or the local structure or DOS at the abundant interfaces in these STE materials. Similar large gems remain to be discovered on the basic materials chemistry side as well. Most prominent amongst these is the observation that while there is nothing fundamentally "special" about PEDOT:PSS or Bi_2Te_3, the field has struggled to design or discover new materials that beat these systems for *p*- and *n*-type transport, respectively. The field is currently poised to transition from proof-of-principle to realistic STEG device design and scaling, creating space for innovative work on device design rules and fabrication strategies. Throughout this dissertation, we have focused on elucidating the fundamental phenomena implicated in carrier transport in complex STE material systems. By first understanding the specific physics dictating transport in these systems, we develop new organic-inorganic composite materials with improved thermoelectric properties.

In Chapter 4, we developed a prototypical hybrid material platform to enable systematic investigation of the key hypotheses regarding high performance in hybrid materials. To do this, we developed a novel technique for solution-based patterning of hetero-nanowires at scale. We show that formation of $Cu_{1.75}Te$ alloy subphases within Te-PEDOT:PSS nanowires can provide an enhancement of the material Seebeck coefficient, leading to up to 22% improvement in the thermoelectric power factor. In Chapter 5, we leverage this material system in the first systematic study of the dominant carrier physics occurring in such complex hybrid systems. Using a full suite of experimental techniques paired with molecular dynamics and density functional theory calculations, we are able to elucidate the major factors contributing to enhanced thermoelectric performance in these materials. Contrary to prevailing belief in the field, carrier filtering seems to play little to no role in the high performance of these materials; rather, structural effects in the organic phase and interfacial charge transport are identified as the critical factors. This work includes the first computational observation of physical templating of polymeric domains at the organic-inorganic interface. We leverage this phenomenon in Chapter 6, developing a novel solution-based platform for the synthesis of air stable *n*-type soft thermoelectric inks using PDI small molecules. Here, experimental evidence directly links structural organization of organic molecules on the inorganic surface to the enhanced electrical conductivity and thermoelectric efficiency of these hybrid organic-inorganic materials. Allowing this molecular level insight to drive design methodologies, PDI hybrid inks are prepared with up to 20-fold improved thermoelectric power factors over the pristine molecule. Utilizing both the *n*-type PDI composite from Chapter 6 and the *p*-type Te-PEDOT:PSS composite from Chapter 4, we demonstrate the fabrication of a solution-printed thermoelectric module with innovative folded geometry and excellent mechanical flexibility.

Our findings help shape promising hybrid design strategies by leveraging molecular-level effects at the hard-soft interface. Additionally, and more controversially, the results of this dissertation suggest that the role of energy filtering has been overestimated in the field of soft thermoelectrics. Both experimental and theoretical evidence points to the importance of structural effects, especially in the organic phase, as well as interfacial charge transfer phenomena in dictating the thermoelectric properties of complex composites. Coupling this molecular-level insight with novel hybrid design strategies brings the field closer to the realization of practical all-ink flexible thermoelectric modules and their integration into applications such as implantable medical devices, wearable technologies, and the Internet of Things.

References

(1) Vineis, C. J.; Shakouri, A.; Majumdar, A.; Kanatzidis, M. G. Nanostructured Thermoelectrics: Big Efficiency Gains from Small Features. *Adv. Mater.* **2010**, *22* (36), 3970–3980. https://doi.org/10.1002/adma.201000839.

(2) Wright, D. A. Thermoelectric Properties of Bismuth Telluride and Its Alloys. *Nature* **1958**, *181* (4612), 834. https://doi.org/10.1038/181834a0.

(3) Yang, J.; Yip, H.-L.; Jen, A. K.-Y. Rational Design of Advanced Thermoelectric Materials. *Adv. Energy Mater.* **2013**, *3* (5), 549–565. https://doi.org/10.1002/aenm.201200514.

(4) Shakouri, A. Recent Developments in Semiconductor Thermoelectric Physics and Materials. *Annu. Rev. Mater. Res.* **2011**, *41* (1), 399–431. https://doi.org/10.1146/annurev-matsci-062910-100445.

(5) Russ, B.; Glaudell, A.; Urban, J. J.; Chabinyc, M. L.; Segalman, R. A. Organic Thermoelectric Materials for Energy Harvesting and Temperature Control. *Nat. Rev. Mater.* **2016**, *1*, 16050. https://doi.org/10.1038/natrevmats.2016.50.

(6) Bubnova, O.; Crispin, X. Towards Polymer-Based Organic Thermoelectric Generators. *Energy Environ. Sci.* **2012**, *5* (11), 9345. https://doi.org/10.1039/c2ee22777k.

(7) Poehler, T. O.; Katz, H. E. Prospects for Polymer-Based Thermoelectrics: State of the Art and Theoretical Analysis. *Energy Environ. Sci.* **2012**, *5* (8), 8110. https://doi.org/10.1039/c2ee22124a.

(8) Bahk, J.-H.; Fang, H.; Yazawa, K.; Shakouri, A. Flexible Thermoelectric Materials and Device Optimization for Wearable Energy Harvesting. *J. Mater. Chem. C* **2015**, *3* (40), 10362–10374. https://doi.org/10.1039/C5TC01644D.

(9) Dong, X.; Xiong, S.; Luo, B.; Ge, R.; Li, Z.; Li, J.; Zhou, Y. Flexible and Transparent Organic–Inorganic Hybrid Thermoelectric Modules. *ACS Appl. Mater. Interfaces* **2018**, *10* (31), 26687–26693. https://doi.org/10.1021/acsami.8b08696.

(10) Chen, Y.; Zhao, Y.; Liang, Z. Solution Processed Organic Thermoelectrics: Towards Flexible Thermoelectric Modules. *Energy Environ. Sci.* **2015**, *8* (2), 401–422. https://doi.org/10.1039/C4EE03297G.

(11) Zhang, Z.; Qiu, J.; Wang, S. Roll-to-Roll Printing of Flexible Thin-Film Organic Thermoelectric Devices. *Manuf. Lett.* **2016**, *8*, 6–10. https://doi.org/10.1016/j.mfglet.2016.04.002.

(12) We, J. H.; Kim, S. J.; Cho, B. J. Hybrid Composite of Screen-Printed Inorganic Thermoelectric Film and Organic Conducting Polymer for Flexible Thermoelectric Power Generator. *Energy* **2014**, *73*, 506–512. https://doi.org/10.1016/j.energy.2014.06.047.

(13) Kim, S. J.; Choi, H.; Kim, Y.; We, J. H.; Shin, J. S.; Lee, H. E.; Oh, M.-W.; Lee, K. J.; Cho, B. J. Post Ionized Defect Engineering of the Screen-Printed Bi2Te2.7Se0.3 Thick Film for High Performance Flexible Thermoelectric Generator. *Nano Energy* **2017**, *31*, 258–263. https://doi.org/10.1016/j.nanoen.2016.11.034.

(14) Søndergaard, R. R.; Hösel, M.; Espinosa, N.; Jørgensen, M.; Krebs, F. C. Practical Evaluation of Organic Polymer Thermoelectrics by Large-Area R2R Processing on Flexible Substrates. *Energy Sci. Eng.* **2013**, *1* (2), 81–88. https://doi.org/10.1002/ese3.8.

(15) Gordiz, K.; Menon, A. K.; Yee, S. K. Interconnect Patterns for Printed Organic Thermoelectric Devices with Large Fill Factors. *J. Appl. Phys.* **2017**, *122* (12), 124507. https://doi.org/10.1063/1.4989589.

(16) Yau, C.-W.; Kwok, T. T.-O.; Lei, C.-U.; Kwok, Y.-K. Energy Harvesting in Internet of Things. In *Internet of Everything: Algorithms, Methodologies, Technologies and Perspectives*; Di Martino, B., Li, K.-C., Yang, L. T., Esposito, A., Eds.; Internet of Things; Springer Singapore: Singapore, 2018; pp 35–79. https://doi.org/10.1007/978-981-10-5861-5_3.

(17) Siddique, A. R. M.; Mahmud, S.; Heyst, B. V. A Review of the State of the Science on Wearable Thermoelectric Power Generators (TEGs) and Their Existing Challenges. *Renew. Sustain. Energy Rev.* **2017**, *73*, 730–744. https://doi.org/10.1016/j.rser.2017.01.177.

(18) Rozgić, D.; Marković, D. A Miniaturized 0.78-MW/Cm2 Autonomous Thermoelectric Energy-Harvesting Platform for Biomedical Sensors. *IEEE Trans. Biomed. Circuits Syst.* **2017**, *11* (4), 773–783. https://doi.org/10.1109/TBCAS.2017.2684818.

(19) Bubnova, O.; Khan, Z. U.; Malti, A.; Braun, S.; Fahlman, M.; Berggren, M.; Crispin, X. Optimization of the Thermoelectric Figure of Merit in the Conducting Polymer Poly(3,4-Ethylenedioxythiophene). *Nat. Mater.* **2011**, *10* (6), 429–433. https://doi.org/10.1038/nmat3012.

(20) Bubnova, O.; Khan, Z. U.; Wang, H.; Braun, S.; Evans, D. R.; Fabretto, M.; Hojati-Talemi, P.; Dagnelund, D.; Arlin, J.-B.; Geerts, Y. H.; et al. Semi-Metallic Polymers. *Nat. Mater.* **2014**, *13* (2), 190. https://doi.org/10.1038/nmat3824.

(21) Park, T.; Park, C.; Kim, B.; Shin, H.; Kim, E. Flexible PEDOT Electrodes with Large Thermoelectric Power Factors to Generate Electricity by the Touch of Fingertips. *Energy Environ. Sci.* **2013**, *6* (3), 788–792. https://doi.org/10.1039/C3EE23729J.

(22) Zhang, Q.; Sun, Y.; Xu, W.; Zhu, D. Organic Thermoelectric Materials: Emerging Green Energy Materials Converting Heat to Electricity Directly and Efficiently. *Adv. Mater.* **2014**, *26* (40), 6829–6851. https://doi.org/10.1002/adma.201305371.

(23) Bergman, D. J.; Levy, O. Thermoelectric Properties of a Composite Medium. *J. Appl. Phys.* **1991**, *70* (11), 6821–6833. https://doi.org/10.1063/1.349830.

(24) See, K. C.; Feser, J. P.; Chen, C. E.; Majumdar, A.; Urban, J. J.; Segalman, R. A. Water-Processable Polymer−Nanocrystal Hybrids for Thermoelectrics. *Nano Lett.* **2010**, *10* (11), 4664–4667. https://doi.org/10.1021/nl102880k.

(25) Zaia, E. W.; Sahu, A.; Zhou, P.; Gordon, M. P.; Forster, J. D.; Aloni, S.; Liu, Y.-S.; Guo, J.; Urban, J. J. Carrier Scattering at Alloy Nanointerfaces Enhances Power Factor in PEDOT:PSS Hybrid Thermoelectrics. *Nano Lett.* **2016**, *16* (5), 3352–3359. https://doi.org/10.1021/acs.nanolett.6b01009.

(26) He, M.; Ge, J.; Lin, Z.; Feng, X.; Wang, X.; Lu, H.; Yang, Y.; Qiu, F. Thermopower Enhancement in Conducting Polymer Nanocomposites via Carrier Energy Scattering at the Organic–Inorganic Semiconductor Interface. *Energy Environ. Sci.* **2012**, *5* (8), 8351–8358. https://doi.org/10.1039/C2EE21803H.

(27) Yao, H.; Fan, Z.; Cheng, H.; Guan, X.; Wang, C.; Sun, K.; Ouyang, J. Recent Development of Thermoelectric Polymers and Composites. *Macromol. Rapid Commun.* **2018**, *39* (6), 1700727. https://doi.org/10.1002/marc.201700727.

(28) Li, Q. *Functional Organic and Hybrid Nanostructured Materials: Fabrication, Properties, and Applications*; John Wiley & Sons, 2018.

(29) Cho, E. S.; Coates, N. E.; Forster, J. D.; Ruminski, A. M.; Russ, B.; Sahu, A.; Su, N. C.; Yang, F.; Urban, J. J. Engineering Synergy: Energy and Mass Transport in Hybrid Nanomaterials. *Adv. Mater.* **2015**, *27* (38), 5744–5752. https://doi.org/10.1002/adma.201500130.

(30) Hokazono, M.; Anno, H.; Toshima, N. Thermoelectric Properties and Thermal Stability of PEDOT:PSS Films on a Polyimide Substrate and Application in Flexible Energy Conversion Devices. *J. Electron. Mater.* **2014**, *43* (6), 2196–2201. https://doi.org/10.1007/s11664-014-3003-y.

(31) Stepien, L.; Roch, A.; Tkachov, R.; Leupolt, B.; Han, L.; van Ngo, N.; Leyens, C. Thermal Operating Window for PEDOT:PSS Films and Its Related Thermoelectric Properties. *Synth. Met.* **2017**, *225*, 49–54. https://doi.org/10.1016/j.synthmet.2016.11.017.

(32) Koplow, M.; Chen, A.; Steingart, D.; Wright, P. K.; Evans, J. W. Thick Film Thermoelectric Energy Harvesting Systems for Biomedical Applications. In *2008 5th International Summer School and Symposium on Medical Devices and Biosensors*; 2008; pp 322–325. https://doi.org/10.1109/ISSMDBS.2008.4575084.

(33) Rein, M.; Favrod, V. D.; Hou, C.; Khudiyev, T.; Stolyarov, A.; Cox, J.; Chung, C.-C.; Chhav, C.; Ellis, M.; Joannopoulos, J.; et al. Diode Fibres for Fabric-Based Optical Communications. *Nature* **2018**, *560* (7717), 214. https://doi.org/10.1038/s41586-018-0390-x.

(34) Hannan, M. A.; Mutashar, S.; Samad, S. A.; Hussain, A. Energy Harvesting for the Implantable Biomedical Devices: Issues and Challenges. *Biomed. Eng. OnLine* **2014**, *13* (1), 79. https://doi.org/10.1186/1475-925X-13-79.

(35) Yang, Y.; Wei, X.-J.; Liu, J. Suitability of a Thermoelectric Power Generator for Implantable Medical Electronic Devices. *J. Phys. Appl. Phys.* **2007**, *40* (18), 5790. https://doi.org/10.1088/0022-3727/40/18/042.

(36) Yang, J.; Caillat, T. Thermoelectric Materials for Space and Automotive Power Generation. *MRS Bull.* **2006**, *31* (3), 224–229. https://doi.org/10.1557/mrs2006.49.

(37) Bhatia, D.; Bairagi, S.; Goel, S.; Jangra, M. Pacemakers Charging Using Body Energy. *J. Pharm. Bioallied Sci.* **2010**, *2* (1), 51–54. https://doi.org/10.4103/0975-7406.62713.

(38) Leonov, V. Thermoelectric Energy Harvesting of Human Body Heat for Wearable Sensors. *IEEE Sens. J.* **2013**, *13* (6), 2284–2291. https://doi.org/10.1109/JSEN.2013.2252526.

(39) Choi, J.; Zaia, E. W.; Gordon, M. P.; Urban, J. J. Weaving a New World: Wearable Thermoelectric Textiles. *Curr. Trends Fash. Technol. Text. Eng.* **2017**, *2* (2). https://doi.org/10.19080/CTFTTE.2018.02.555583.

(40) Bals, A.; Barnes, N.; Bravo, R.; Garcia, N.; O'Bryan, J.; Santana, D. Powering a Biosensor Using Wearable Thermoelectric Technology. *Interdiscip. Des. Sr. Theses* **2018**.

(41) Carlson, E. J.; Strunz, K.; Otis, B. P. A 20 MV Input Boost Converter With Efficient Digital Control for Thermoelectric Energy Harvesting. *IEEE J. Solid-State Circuits* **2010**, *45* (4), 741–750. https://doi.org/10.1109/JSSC.2010.2042251.

(42) Alioto, M.; Sánchez-Sinencio, E.; Sangiovanni-Vincentelli, A. Guest Editorial Special Issue on Circuits and Systems for the Internet of Things—From Sensing to Sensemaking. *IEEE Trans. Circuits Syst. Regul. Pap.* **2017**, *64* (9), 2221–2225. https://doi.org/10.1109/TCSI.2017.2730678.

(43) Miorandi, D.; Sicari, S.; De Pellegrini, F.; Chlamtac, I. Internet of Things: Vision, Applications and Research Challenges. *Ad Hoc Netw.* **2012**, *10* (7), 1497–1516. https://doi.org/10.1016/j.adhoc.2012.02.016.

(44) Wan, Q.; Teh, Y.; Gao, Y.; Mok, P. K. T. Analysis and Design of a Thermoelectric Energy Harvesting System With Reconfigurable Array of Thermoelectric Generators for IoT Applications. *IEEE Trans. Circuits Syst. Regul. Pap.* **2017**, *64* (9), 2346–2358. https://doi.org/10.1109/TCSI.2017.2708763.

(45) Gaudin, S. Get Ready to Live in a Trillion-Device World. *ComputerWorld, Tech. Rep.* September 2015.

(46) Rana, M. M.; Xiang, W.; Wang, E.; Li, X.; Choi, B. J. Internet of Things Infrastructure for Wireless Power Transfer Systems. *IEEE Access* **2018**, *6*, 19295–19303. https://doi.org/10.1109/ACCESS.2018.2795803.

(47) Kurs, A.; Karalis, A.; Moffatt, R.; Joannopoulos, J. D.; Fisher, P.; Soljačić, M. Wireless Power Transfer via Strongly Coupled Magnetic Resonances. *Science* **2007**, *317* (5834), 83–86. https://doi.org/10.1126/science.1143254.

(48) Mohamed, N. F. A.; Agbinya, J. I. Magnetic Power Tuning Architectures in Wireless Power Transfer Systems. In *2018 IEEE PELS Workshop on Emerging Technologies: Wireless Power Transfer (Wow)*; 2018; pp 1–4. https://doi.org/10.1109/WoW.2018.8450885.

(49) Merrett, G. V.; White, N. M.; Harris, N. R.; Al-Hashimi, B. M. Energy-Aware Simulation for Wireless Sensor Networks. In *2009 6th Annual IEEE Communications Society Conference on Sensor, Mesh and Ad Hoc Communications and Networks*; IEEE: Rome, Italy, 2009; pp 1–8. https://doi.org/10.1109/SAHCN.2009.5168932.

(50) Liu, X.; Qian, F. Measuring and Optimizing Android Smartwatch Energy Consumption: Poster. In *Proceedings of the 22Nd Annual International Conference on Mobile Computing and Networking*; MobiCom '16; ACM: New York, NY, USA, 2016; pp 421–423. https://doi.org/10.1145/2973750.2985259.

(51) Bae, E. J.; Kang, Y. H.; Jang, K.-S.; Cho, S. Y. Enhancement of Thermoelectric Properties of PEDOT:PSS and Tellurium-PEDOT:PSS Hybrid Composites by Simple Chemical Treatment. *Sci. Rep.* **2016**, *6*, 18805. https://doi.org/10.1038/srep18805.

(52) Wang, L.; Zhang, Z.; Geng, L.; Yuan, T.; Liu, Y.; Guo, J.; Fang, L.; Qiu, J.; Wang, S. Solution-Printable Fullerene/TiS 2 Organic/Inorganic Hybrids for High-Performance Flexible n-Type Thermoelectrics. *Energy Environ. Sci.* **2018**, *11* (5), 1307–1317. https://doi.org/10.1039/C7EE03617E.

(53) Mai, C.-K.; Russ, B.; L. Fronk, S.; Hu, N.; B. Chan-Park, M.; J. Urban, J.; A. Segalman, R.; L. Chabinyc, M.; C. Bazan, G. Varying the Ionic Functionalities of Conjugated Polyelectrolytes Leads to Both P- and n-Type Carbon Nanotube Composites for Flexible Thermoelectrics. *Energy Environ. Sci.* **2015**, *8* (8), 2341–2346. https://doi.org/10.1039/C5EE00938C.

(54) Choi, H.; Kim, S. J.; Kim, Y.; We, J. H.; Oh, M.-W.; Cho, B. J. Enhanced Thermoelectric Properties of Screen-Printed Bi0.5Sb1.5Te3 and Bi2Te2.7Se0.3 Thick Films Using a Post Annealing Process with Mechanical Pressure. *J. Mater. Chem. C* **2017**, *5* (33), 8559–8565. https://doi.org/10.1039/C7TC01797A.

(55) Carreon-Bautista, S.; Eladawy, A.; Mohieldin, A. N.; Sánchez-Sinencio, E. Boost Converter With Dynamic Input Impedance Matching for Energy Harvesting With Multi-Array Thermoelectric Generators. *IEEE Trans. Ind. Electron.* **2014**, *61* (10), 5345–5353. https://doi.org/10.1109/TIE.2014.2300035.

(56) Shin, S.; Roh, J. W.; Kim, H.-S.; Chen, R. Role of Surfactant on Thermoelectric Behaviors of Organic-Inorganic Composites. *J. Appl. Phys.* **2018**, *123* (20), 205106. https://doi.org/10.1063/1.5033920.

(57) Yu, C.; Choi, K.; Yin, L.; Grunlan, J. C. Light-Weight Flexible Carbon Nanotube Based Organic Composites with Large Thermoelectric Power Factors. *ACS Nano* **2011**, *5* (10), 7885–7892. https://doi.org/10.1021/nn202868a.

(58) Chen, Y.; He, M.; Liu, B.; Bazan, G. C.; Zhou, J.; Liang, Z. Bendable N-Type Metallic Nanocomposites with Large Thermoelectric Power Factor. *Adv. Mater.* **2017**, *29* (4), 1604752. https://doi.org/10.1002/adma.201604752.

(59) Du, Y.; Cai, K. F.; Chen, S.; Cizek, P.; Lin, T. Facile Preparation and Thermoelectric Properties of Bi2Te3 Based Alloy Nanosheet/PEDOT:PSS Composite Films. *ACS Appl. Mater. Interfaces* **2014**, *6* (8), 5735–5743. https://doi.org/10.1021/am5002772.

(60) Bounioux, C.; Díaz-Chao, P.; Campoy-Quiles, M.; S. Martín-González, M.; R. Goñi, A.; Yerushalmi-Rozen, R.; Müller, C. Thermoelectric Composites of Poly(3-Hexylthiophene) and Carbon Nanotubes with a Large Power Factor. *Energy Environ. Sci.* **2013**, *6* (3), 918–925. https://doi.org/10.1039/C2EE23406H.

(61) Cho, C.; Wallace, K. L.; Tzeng, P.; Hsu, J.-H.; Yu, C.; Grunlan, J. C. Outstanding Low Temperature Thermoelectric Power Factor from Completely Organic Thin Films Enabled by Multidimensional Conjugated Nanomaterials. *Adv. Energy Mater.* *6* (7), 1502168. https://doi.org/10.1002/aenm.201502168.

(62) Ziman, J. M. *Electrons and Phonons: The Theory of Transport Phenomena in Solids*; OUP Oxford, 2001.

(63) Kang, S. D.; Snyder, G. J. Charge-Transport Model for Conducting Polymers. *Nat. Mater.* **2017**, *16* (2), 252–257. https://doi.org/10.1038/nmat4784.

(64) Urban, J. J. Organic Electronics: One Model to Rule Them All. *Nat. Mater.* **2017**, *16* (2), 157–159. https://doi.org/10.1038/nmat4790.

(65) Cho, B.; Park, K. S.; Baek, J.; Oh, H. S.; Koo Lee, Y.-E.; Sung, M. M. Single-Crystal Poly(3,4-Ethylenedioxythiophene) Nanowires with Ultrahigh Conductivity. *Nano Lett.* **2014**, *14* (6), 3321–3327. https://doi.org/10.1021/nl500748y.

(66) MacDiarmid, A. G. "Synthetic Metals": A Novel Role for Organic Polymers (Nobel Lecture). *Angew. Chem. Int. Ed.* **2001**, *40* (14), 2581–2590. https://doi.org/10.1002/1521-3773(20010716)40:14<2581::AID-ANIE2581>3.0.CO;2-2.

(67) Thomas, E. M.; Brady, M. A.; Nakayama, H.; Popere, B. C.; Segalman, R. A.; Chabinyc, M. L. X-Ray Scattering Reveals Ion-Induced Microstructural Changes During

Electrochemical Gating of Poly(3-Hexylthiophene). *Adv. Funct. Mater. 0* (0), 1803687. https://doi.org/10.1002/adfm.201803687.

(68) Singh, V.; Bougher, T. L.; Weathers, A.; Cai, Y.; Bi, K.; Pettes, M. T.; McMenamin, S. A.; Lv, W.; Resler, D. P.; Gattuso, T. R.; et al. High Thermal Conductivity of Chain-Oriented Amorphous Polythiophene. *Nat. Nanotechnol.* **2014**, *9* (5), 384–390. https://doi.org/10.1038/nnano.2014.44.

(69) Zhong, Z.; Wingert, M. C.; Strzalka, J.; Wang, H.-H.; Sun, T.; Wang, J.; Chen, R.; Jiang, Z. Structure-Induced Enhancement of Thermal Conductivities in Electrospun Polymer Nanofibers. *Nanoscale* **2014**, *6* (14), 8283–8291. https://doi.org/10.1039/C4NR00547C.

(70) Lu, N.; Li, L.; Liu, M. A Review of Carrier Thermoelectric-Transport Theory in Organic Semiconductors. *Phys. Chem. Chem. Phys.* **2016**, *18* (29), 19503–19525. https://doi.org/10.1039/C6CP02830F.

(71) Dhanker, R.; Gray, C. L.; Mukhopadhyay, S.; Nunez, S.; Cheng, C.-Y.; Sokolov, A. N.; Giebink, N. C. Large Bipolaron Density at Organic Semiconductor/Electrode Interfaces. *Nat. Commun.* **2017**, *8* (1), 2252. https://doi.org/10.1038/s41467-017-02459-3.

(72) Malen, J. A.; Yee, S. K.; Majumdar, A.; Segalman, R. A. Fundamentals of Energy Transport, Energy Conversion, and Thermal Properties in Organic–Inorganic Heterojunctions. *Chem. Phys. Lett.* **2010**, *491* (4–6), 109–122. https://doi.org/10.1016/j.cplett.2010.03.028.

(73) Wang, L.; Zhang, Z.; Liu, Y.; Wang, B.; Fang, L.; Qiu, J.; Zhang, K.; Wang, S. Exceptional Thermoelectric Properties of Flexible Organic−inorganic Hybrids with Monodispersed and Periodic Nanophase. *Nat. Commun.* **2018**, *9* (1), 3817. https://doi.org/10.1038/s41467-018-06251-9.

(74) Wei, K.; Stedman, T.; Ge, Z.-H.; Woods, L. M.; Nolas, G. S. A Synthetic Approach for Enhanced Thermoelectric Properties of PEDOT:PSS Bulk Composites. *Appl. Phys. Lett.* **2015**, *107* (15), 153301. https://doi.org/10.1063/1.4933254.

(75) Kumar, P.; Zaia, E. W.; Yildirim, E.; Repaka, D. V. M.; Yang, S.-W.; Urban, J. J.; Hippalgaonkar, K. Polymer Morphology and Interfacial Charge Transfer Dominate over Energy-Dependent Scattering in Organic-Inorganic Thermoelectrics. *Nat. Commun.* **2018**, *9* (1), 5347. https://doi.org/10.1038/s41467-018-07435-z.

(76) Heyman, J. N.; Alebachew, B. A.; Kaminski, Z. S.; Nguyen, M. D.; Coates, N. E.; Urban, J. J. Terahertz and Infrared Transmission of an Organic/Inorganic Hybrid Thermoelectric Material. *Appl. Phys. Lett.* **2014**, *104* (14), 141912. https://doi.org/10.1063/1.4871316.

(77) Hicks, L. D.; Dresselhaus, M. S. Effect of Quantum-Well Structures on the Thermoelectric Figure of Merit. *Phys. Rev. B* **1993**, *47* (19), 12727–12731. https://doi.org/10.1103/PhysRevB.47.12727.

(78) Heremans, J. P.; Jovovic, V.; Toberer, E. S.; Saramat, A.; Kurosaki, K.; Charoenphakdee, A.; Yamanaka, S.; Snyder, G. J. Enhancement of Thermoelectric Efficiency in PbTe by Distortion of the Electronic Density of States. *Science* **2008**, *321* (5888), 554–557. https://doi.org/10.1126/science.1159725.

(79) Park, H.; Hwan Lee, S.; Sunjoo Kim, F.; Hee Choi, H.; Woo Cheong, I.; Hyun Kim, J. Enhanced Thermoelectric Properties of PEDOT:PSS Nanofilms by a Chemical Dedoping Process. *J. Mater. Chem. A* **2014**, *2* (18), 6532–6539. https://doi.org/10.1039/C3TA14960A.

(80) Kim, G.-H.; Shao, L.; Zhang, K.; Pipe, K. P. Engineered Doping of Organic Semiconductors for Enhanced Thermoelectric Efficiency. *Nat. Mater.* **2013**, *12* (8), 719–723. https://doi.org/10.1038/nmat3635.

(81) Bubnova, O.; Berggren, M.; Crispin, X. Tuning the Thermoelectric Properties of Conducting Polymers in an Electrochemical Transistor. *J. Am. Chem. Soc.* **2012**, *134* (40), 16456–16459. https://doi.org/10.1021/ja305188r.

(82) Liang, Z.; J. Boland, M.; Butrouna, K.; R. Strachan, D.; R. Graham, K. Increased Power Factors of Organic–Inorganic Nanocomposite Thermoelectric Materials and the Role of Energy Filtering. *J. Mater. Chem. A* **2017**, *5* (30), 15891–15900. https://doi.org/10.1039/C7TA02307C.

(83) Cahill, D. G.; Ford, W. K.; Goodson, K. E.; Mahan, G. D.; Majumdar, A.; Maris, H. J.; Merlin, R.; Phillpot, S. R. Nanoscale Thermal Transport. *J. Appl. Phys.* **2002**, *93* (2), 793–818. https://doi.org/10.1063/1.1524305.

(84) Snyder, G. J.; Toberer, E. S. Complex Thermoelectric Materials. *Nat. Mater.* **2008**, *7* (2), 105–114. https://doi.org/10.1038/nmat2090.

(85) Zhu, Y.; Liu, Y.; Tan, X.; Ren, G.; Yu, M.; Hu, T.; Marcelli, A.; Xu, W. Enhanced Thermoelectric Performance through Grain Boundary Engineering in Quaternary Chalcogenide Cu2ZnSnSe4. *AIP Adv.* **2018**, *8* (4), 045218. https://doi.org/10.1063/1.5025482.

(86) Benyahia, M.; Ohorodniichuk, V.; Leroy, E.; Dauscher, A.; Lenoir, B.; Alleno, E. High Thermoelectric Figure of Merit in Mesostructured In0. 25Co4Sb12 n-Type Skutterudite. *J. Alloys Compd.* **2018**, *735*, 1096–1104.

(87) Maeno, S.; Cannon, J. J.; Shiga, T.; Shiomi, J. Molecular Dynamics Study on Heat Conduction in Poly (3, 4-Ethylenedioxythiophene). *Jpn. J. Appl. Phys.* **2018**, *57* (10), 101601.

(88) Shi, W.; Wu, G.; Yong, X.; Deng, T.; Wang, J.-S.; Zheng, J.-C.; Xu, J.; Sullivan, M. B.; Yang, S.-W. Orbital-Engineering Based Screening of π-Conjugated D8 Transition-Metal

Coordination Polymers for High-Performance n-Type Thermoelectric Applications. *ACS Appl. Mater. Interfaces* **2018**.

(89) He, Y.; Cubuk, E. D.; Allendorf, M. D.; Reed, E. J. Metallic Metal–Organic Frameworks Predicted by the Combination of Machine Learning Methods and Ab Initio Calculations. *J. Phys. Chem. Lett.* **2018**, *9* (16), 4562–4569.

(90) Iwasaki, Y.; Takeuchi, I.; Stanev, V.; Kusne, A. G.; Ishida, M.; Kirihara, A.; Ihara, K.; Sawada, R.; Terashima, K.; Someya, H. Machine-Learning Guided Discovery of a High-Performance Spin-Driven Thermoelectric Material. *ArXiv Prepr. ArXiv180502303* **2018**.

(91) Yang, G.; Pan, J.; Fu, X.; Hu, Z.; Wang, Y.; Wu, Z.; Mu, E.; Yan, X.-J.; Lu, M.-H. A Comparative Experimental Study on the Cross-Plane Thermal Conductivities of Nano-Constructed Sb 2 Te 3/(Cu, Ag, Au, Pt) Thermoelectric Multilayer Thin Films. *Nano Converg.* **2018**, *5* (1), 22.

(92) Chen, L.-C.; Cao, Z.-Y.; Yu, H.; Jiang, B.-B.; Su, L.; Shi, X.; Chen, L.-D.; Chen, X.-J. Phonon Anharmonicity in Thermoelectric Palladium Sulfide by Raman Spectroscopy. *Appl. Phys. Lett.* **2018**, *113* (2), 022105.

(93) Sassi, S.; Candolfi, C.; Dauscher, A.; Lenoir, B.; Koza, M. M. Inelastic Neutron Scattering Study of the Lattice Dynamics of the Homologous Compounds (PbSe) 5 (Bi 2 Se 3) 3m (M= 1, 2 and 3). *Phys. Chem. Chem. Phys.* **2018**, *20* (21), 14597–14607.

(94) Liu, J.; Wang, X.; Li, D.; Coates, N. E.; Segalman, R. A.; Cahill, D. G. Thermal Conductivity and Elastic Constants of PEDOT:PSS with High Electrical Conductivity. *Macromolecules* **2015**, *48* (3), 585–591. https://doi.org/10.1021/ma502099t.

(95) Weathers, A.; Khan, Z. U.; Brooke, R.; Evans, D.; Pettes, M. T.; Andreasen, J. W.; Crispin, X.; Shi, L. Significant Electronic Thermal Transport in the Conducting Polymer Poly(3,4-Ethylenedioxythiophene). *Adv. Mater.* **2015**, *27* (12), 2101–2106. https://doi.org/10.1002/adma.201404738.

(96) Wang, H.; Hsu, J.-H.; Yi, S.-I.; Kim, S. L.; Choi, K.; Yang, G.; Yu, C. Thermally Driven Large N-Type Voltage Responses from Hybrids of Carbon Nanotubes and Poly(3,4-Ethylenedioxythiophene) with Tetrakis(Dimethylamino)Ethylene. *Adv. Mater.* **2015**, *27* (43), 6855–6861. https://doi.org/10.1002/adma.201502950.

(97) Tian, R.; Wan, C.; Wang, Y.; Wei, Q.; Ishida, T.; Yamamoto, A.; Tsuruta, A.; Shin, W.; Li, S.; Koumoto, K. A Solution-Processed TiS2/Organic Hybrid Superlattice Film towards Flexible Thermoelectric Devices. *J. Mater. Chem. A* **2017**, *5* (2), 564–570.

(98) Polvani, D. A.; Meng, J. F.; Chandra Shekar, N. V.; Sharp, J.; Badding, J. V. Large Improvement in Thermoelectric Properties in Pressure-Tuned p-Type Sb1.5Bi0.5Te3. *Chem. Mater.* **2001**, *13* (6), 2068–2071. https://doi.org/10.1021/cm000888q.

(99) Meng, J. F.; Shekar, N. V. C.; Badding, J. V.; Chung, D.-Y.; Kanatzidis, M. G. Multifold Enhancement of the Thermoelectric Figure of Merit in P-Type BaBiTe3 by Pressure Tuning. *J. Appl. Phys.* **2001**, *90* (6), 2836–2839. https://doi.org/10.1063/1.1394905.

(100) Nan, K.; Kang, S. D.; Li, K.; Yu, K. J.; Zhu, F.; Wang, J.; Dunn, A. C.; Zhou, C.; Xie, Z.; Agne, M. T.; et al. Compliant and Stretchable Thermoelectric Coils for Energy Harvesting in Miniature Flexible Devices. *Sci. Adv.* **2018**, *4* (11), eaau5849. https://doi.org/10.1126/sciadv.aau5849.

(101) Kim, Y. H.; Sachse, C.; Machala, M. L.; May, C.; Müller-Meskamp, L.; Leo, K. Highly Conductive PEDOT:PSS Electrode with Optimized Solvent and Thermal Post-Treatment for ITO-Free Organic Solar Cells. *Adv. Funct. Mater.* **2011**, *21* (6), 1076–1081. https://doi.org/10.1002/adfm.201002290.

(102) Xie, R.; Colby, R. H.; Gomez, E. D. Connecting the Mechanical and Conductive Properties of Conjugated Polymers. *Adv. Electron. Mater.* **2018**, *4* (10), 1700356. https://doi.org/10.1002/aelm.201700356.

(103) Yue, R.; Xu, J. Poly(3,4-Ethylenedioxythiophene) as Promising Organic Thermoelectric Materials: A Mini-Review. *Synth. Met.* **2012**, *162* (11–12), 912–917. https://doi.org/10.1016/j.synthmet.2012.04.005.

(104) Anthopoulos, T. D.; Anyfantis, G. C.; Papavassiliou, G. C.; Leeuw, D. M. de. Air-Stable Ambipolar Organic Transistors. *Appl. Phys. Lett.* **2007**, *90* (12), 122105. https://doi.org/10.1063/1.2715028.

(105) Sun, Y.; Sheng, P.; Di, C.; Jiao, F.; Xu, W.; Qiu, D.; Zhu, D. Organic Thermoelectric Materials and Devices Based on P- and n-Type Poly(Metal 1,1,2,2-Ethenetetrathiolate)s. *Adv. Mater.* **2012**, *24* (7), 932–937. https://doi.org/10.1002/adma.201104305.

(106) Ma, W.; Shi, K.; Wu, Y.; Lu, Z.-Y.; Liu, H.-Y.; Wang, J.-Y.; Pei, J. Enhanced Molecular Packing of a Conjugated Polymer with High Organic Thermoelectric Power Factor. *ACS Appl. Mater. Interfaces* **2016**, *8* (37), 24737–24743. https://doi.org/10.1021/acsami.6b06899.

(107) Shi, K.; Zhang, F.; Di, C.-A.; Yan, T.-W.; Zou, Y.; Zhou, X.; Zhu, D.; Wang, J.-Y.; Pei, J. Toward High Performance N-Type Thermoelectric Materials by Rational Modification of BDPPV Backbones. *J. Am. Chem. Soc.* **2015**, *137* (22), 6979–6982. https://doi.org/10.1021/jacs.5b00945.

(108) Zhao, X.; Madan, D.; Cheng, Y.; Zhou, J.; Li, H.; Thon, S. M.; Bragg, A. E.; DeCoster, M. E.; Hopkins, P. E.; Katz, H. E. High Conductivity and Electron-Transfer Validation in an n-Type Fluoride-Anion-Doped Polymer for Thermoelectrics in Air. *Adv. Mater.* **2017**, *29* (34), n/a-n/a. https://doi.org/10.1002/adma.201606928.

(109) Russ, B.; Robb, M. J.; Popere, B. C.; Perry, E. E.; Mai, C.-K.; Fronk, S. L.; Patel, S. N.; Mates, T. E.; Bazan, G. C.; Urban, J. J.; et al. Tethered Tertiary Amines as Solid-State n-Type Dopants for Solution-Processable Organic Semiconductors. *Chem Sci* **2016**, *7* (3), 1914–1919. https://doi.org/10.1039/C5SC04217H.

(110) Duda, J. C.; Hopkins, P. E.; Shen, Y.; Gupta, M. C. Exceptionally Low Thermal Conductivities of Films of the Fullerene Derivative PCBM. *Phys. Rev. Lett.* **2013**, *110* (1), 015902. https://doi.org/10.1103/PhysRevLett.110.015902.

(111) Russ, B.; Robb, M. J.; Brunetti, F. G.; Miller, P. L.; Perry, E. E.; Patel, S. N.; Ho, V.; Chang, W. B.; Urban, J. J.; Chabinyc, M. L.; et al. Power Factor Enhancement in Solution-Processed Organic n-Type Thermoelectrics Through Molecular Design. *Adv. Mater.* **2014**, *26* (21), 3473–3477. https://doi.org/10.1002/adma.201306116.

(112) Inabe, T.; Ogata, H.; Maruyama, Y.; Achiba, Y.; Suzuki, S.; Kikuchi, K.; Ikemoto, I. Electronic Structure of Alkali Metal Doped ${\mathrm{C}}_{60}$ Derived from Thermoelectric Power Measurements. *Phys. Rev. Lett.* **1992**, *69* (26), 3797–3799. https://doi.org/10.1103/PhysRevLett.69.3797.

(113) Sumino, M.; Harada, K.; Ikeda, M.; Tanaka, S.; Miyazaki, K.; Adachi, C. Thermoelectric Properties of N-Type C60 Thin Films and Their Application in Organic Thermovoltaic Devices. *Appl. Phys. Lett.* **2011**, *99* (9), 093308. https://doi.org/10.1063/1.3631633.

(114) Wang, Z. H.; Ichimura, K.; Dresselhaus, M. S.; Dresselhaus, G.; Lee, W.-T.; Wang, K. A.; Eklund, P. C. Electronic Transport Properties of KxC70 Thin Films. *Phys. Rev. B* **1993**, *48* (14), 10657–10660. https://doi.org/10.1103/PhysRevB.48.10657.

(115) Coates, N. E.; Yee, S. K.; McCulloch, B.; See, K. C.; Majumdar, A.; Segalman, R. A.; Urban, J. J. Effect of Interfacial Properties on Polymer-Nanocrystal Thermoelectric Transport. *Adv. Mater.* **2013**, *25* (11), 1629–1633. https://doi.org/10.1002/adma.201203915.

(116) An, H.; Karas, D.; Kim, B.-W.; Trabia, S.; Moon, J. Flexible N-Type Thermoelectric Composite Films with Enhanced Performance through Interface Engineering and Post-Treatment. *Nanotechnology* **2018**, *29* (27), 275403. https://doi.org/10.1088/1361-6528/aabeb6.

(117) Sahu, A.; Russ, B.; Su, N. C.; Forster, J. D.; Zhou, P.; Cho, E. S.; Ercius, P.; Coates, N. E.; Segalman, R. A.; Urban, J. J. Bottom-up Design of de Novo Thermoelectric Hybrid Materials Using Chalcogenide Resurfacing. *J. Mater. Chem. A* **2017**, *5* (7), 3346–3357. https://doi.org/10.1039/C6TA09781B.

(118) Shah, N. H.; Tenenbaum, J. D. The Coming Age of Data-Driven Medicine: Translational Bioinformatics' next Frontier. *J. Am. Med. Inform. Assoc. JAMIA* **2012**, *19* (e1), e2–e4. https://doi.org/10.1136/amiajnl-2012-000969.

(119) Bereau, T.; Andrienko, D.; Kremer, K. Research Update: Computational Materials Discovery in Soft Matter. *APL Mater.* **2016**, *4* (5), 053101. https://doi.org/10.1063/1.4943287.

(120) Jain, A.; Persson, K. A.; Ceder, G. Research Update: The Materials Genome Initiative: Data Sharing and the Impact of Collaborative Ab Initio Databases. *APL Mater.* **2016**, *4* (5), 053102. https://doi.org/10.1063/1.4944683.

(121) Evans, J. D.; Coudert, F.-X. Predicting the Mechanical Properties of Zeolite Frameworks by Machine Learning. *Chem. Mater.* **2017**, *29* (18), 7833–7839. https://doi.org/10.1021/acs.chemmater.7b02532.

(122) Kim, E.; Huang, K.; Saunders, A.; McCallum, A.; Ceder, G.; Olivetti, E. Materials Synthesis Insights from Scientific Literature via Text Extraction and Machine Learning. *Chem. Mater.* **2017**, *29* (21), 9436–9444. https://doi.org/10.1021/acs.chemmater.7b03500.

(123) Jain, A.; Ong, S. P.; Hautier, G.; Chen, W.; Richards, W. D.; Dacek, S.; Cholia, S.; Gunter, D.; Skinner, D.; Ceder, G.; et al. Commentary: The Materials Project: A Materials Genome Approach to Accelerating Materials Innovation. *APL Mater.* **2013**, *1* (1), 011002. https://doi.org/10.1063/1.4812323.

(124) Phillips, C. L.; Littlewood, P. Preface: Special Topic on Materials Genome. *APL Mater.* **2016**, *4* (5), 053001. https://doi.org/10.1063/1.4952608.

(125) Choi, K.; Yu, C. Highly Doped Carbon Nanotubes with Gold Nanoparticles and Their Influence on Electrical Conductivity and Thermopower of Nanocomposites. *PLOS ONE* **2012**, *7* (9), e44977. https://doi.org/10.1371/journal.pone.0044977.

(126) Ju, H.; Kim, J. Chemically Exfoliated SnSe Nanosheets and Their SnSe/Poly(3,4-Ethylenedioxythiophene):Poly(Styrenesulfonate) Composite Films for Polymer Based Thermoelectric Applications. *ACS Nano* **2016**, *10* (6), 5730–5739. https://doi.org/10.1021/acsnano.5b07355.

(127) Zhang, B.; Sun, J.; Katz, H. E.; Fang, F.; Opila, R. L. Promising Thermoelectric Properties of Commercial PEDOT:PSS Materials and Their Bi2Te3 Powder Composites. *ACS Appl. Mater. Interfaces* **2010**, *2* (11), 3170–3178. https://doi.org/10.1021/am100654p.

(128) Yee, S. K.; Coates, N. E.; Majumdar, A.; Urban, J. J.; Segalman, R. A. Thermoelectric Power Factor Optimization in PEDOT:PSS Tellurium Nanowire Hybrid Composites. *Phys. Chem. Chem. Phys.* **2013**, *15* (11), 4024. https://doi.org/10.1039/c3cp44558e.

(129) Dun, C.; Hewitt, C. A.; Huang, H.; Xu, J.; Montgomery, D. S.; Nie, W.; Jiang, Q.; Carroll, D. L. Layered Bi2Se3 Nanoplate/Polyvinylidene Fluoride Composite Based n-Type Thermoelectric Fabrics. *ACS Appl. Mater. Interfaces* **2015**, *7* (13), 7054–7059. https://doi.org/10.1021/acsami.5b00514.

(130) Sinha, J.; Ireland, R. M.; Lee, S. J.; Katz, H. E. Synergistic Thermoelectric Power Factor Increase in Films Incorporating Tellurium and Thiophene-Based Semiconductors. *MRS Commun.* **2013**, *3* (2), 97–100. https://doi.org/10.1557/mrc.2013.14.

(131) Chatterjee, K.; Mitra, M.; Kargupta, K.; Ganguly, S.; Banerjee, D. Synthesis, Characterization and Enhanced Thermoelectric Performance of Structurally Ordered Cable-like Novel Polyaniline–Bismuth Telluride Nanocomposite. *Nanotechnology* **2013**, *24* (21), 215703. https://doi.org/10.1088/0957-4484/24/21/215703.

(132) Jiang, F.; Xiong, J.; Zhou, W.; Liu, C.; Wang, L.; Zhao, F.; Liu, H.; Xu, J. Use of Organic Solvent-Assisted Exfoliated MoS 2 for Optimizing the Thermoelectric Performance of Flexible PEDOT:PSS Thin Films. *J. Mater. Chem. A* **2016**, *4* (14), 5265–5273. https://doi.org/10.1039/C6TA00305B.

(133) Wang, Y.; M. Zhang, S.; Deng, Y. Flexible Low-Grade Energy Utilization Devices Based on High-Performance Thermoelectric Polyaniline/Tellurium Nanorod Hybrid Films. *J. Mater. Chem. A* **2016**, *4* (9), 3554–3559. https://doi.org/10.1039/C6TA01140C.

(134) Ou, C.; Sangle, A. L.; Datta, A.; Jing, Q.; Busolo, T.; Chalklen, T.; Narayan, V.; Kar-Narayan, S. Fully Printed Organic–Inorganic Nanocomposites for Flexible Thermoelectric Applications. *ACS Appl. Mater. Interfaces* **2018**, *10* (23), 19580–19587. https://doi.org/10.1021/acsami.8b01456.

(135) Goldsmid, H. J. The Electrical Conductivity and Thermoelectric Power of Bismuth Telluride. *Proc. Phys. Soc.* **1958**, *71* (4), 633. https://doi.org/10.1088/0370-1328/71/4/312.

(136) Poudel, B.; Hao, Q.; Ma, Y.; Lan, Y.; Minnich, A.; Yu, B.; Yan, X.; Wang, D.; Muto, A.; Vashaee, D.; et al. High-Thermoelectric Performance of Nanostructured Bismuth Antimony Telluride Bulk Alloys. *Science* **2008**, *320* (5876), 634–638. https://doi.org/10.1126/science.1156446.

(137) Geng, L.; Scheifers, J. P.; Fu, C.; Zhang, J.; Fokwa, B. P. T.; Guo, J. Titanium Sulfides as Intercalation-Type Cathode Materials for Rechargeable Aluminum Batteries. *ACS Appl. Mater. Interfaces* **2017**, *9* (25), 21251–21257. https://doi.org/10.1021/acsami.7b04161.

(138) Fan, P.; Zheng, Z.; Li, Y.; Lin, Q.; Luo, J.; Liang, G.; Cai, X.; Zhang, D.; Ye, F. Low-Cost Flexible Thin Film Thermoelectric Generator on Zinc Based Thermoelectric Materials. *Appl. Phys. Lett.* **2015**, *106* (7), 073901. https://doi.org/10.1063/1.4909531.

(139) Li, C.; Jiang, F.; Liu, C.; Wang, W.; Li, X.; Wang, T.; Xu, J. A Simple Thermoelectric Device Based on Inorganic/Organic Composite Thin Film for Energy Harvesting. *Chem. Eng. J.* **2017**, *320*, 201–210. https://doi.org/10.1016/j.cej.2017.03.023.

(140) Du, Y.; Cai, K.; Chen, S.; Wang, H.; Shen, S. Z.; Donelson, R.; Lin, T. Thermoelectric Fabrics: Toward Power Generating Clothing. *Sci. Rep.* **2015**, *5*, 6411. https://doi.org/10.1038/srep06411.

(141) Kim, S. J.; Lee, H. E.; Choi, H.; Kim, Y.; We, J. H.; Shin, J. S.; Lee, K. J.; Cho, B. J. High-Performance Flexible Thermoelectric Power Generator Using Laser Multiscanning Lift-Off Process. *ACS Nano* **2016**, *10* (12), 10851–10857. https://doi.org/10.1021/acsnano.6b05004.

(142) Kim, S. J.; Hyung We, J.; Jin Cho, B. A Wearable Thermoelectric Generator Fabricated on a Glass Fabric. *Energy Environ. Sci.* **2014**, *7* (6), 1959–1965. https://doi.org/10.1039/C4EE00242C.

(143) Sun, T.; Peavey, J. L.; David Shelby, M.; Ferguson, S.; O'Connor, B. T. Heat Shrink Formation of a Corrugated Thin Film Thermoelectric Generator. *Energy Convers. Manag.* **2015**, *103*, 674–680. https://doi.org/10.1016/j.enconman.2015.07.016.

(144) Hewitt, C. A.; Kaiser, A. B.; Roth, S.; Craps, M.; Czerw, R.; Carroll, D. L. Multilayered Carbon Nanotube/Polymer Composite Based Thermoelectric Fabrics. *Nano Lett.* **2012**, *12* (3), 1307–1310. https://doi.org/10.1021/nl203806q.

(145) Yu, C.; Murali, A.; Choi, K.; Ryu, Y. Air-Stable Fabric Thermoelectric Modules Made of N- and P-Type Carbon Nanotubes. *Energy Environ. Sci.* **2012**, *5* (11), 9481–9486. https://doi.org/10.1039/C2EE22838F.

(146) Kim, S. L.; Choi, K.; Tazebay, A.; Yu, C. Flexible Power Fabrics Made of Carbon Nanotubes for Harvesting Thermoelectricity. *ACS Nano* **2014**, *8* (3), 2377–2386. https://doi.org/10.1021/nn405893t.

(147) Hsu, J.-H.; Choi, W.; Yang, G.; Yu, C. Origin of Unusual Thermoelectric Transport Behaviors in Carbon Nanotube Filled Polymer Composites after Solvent/Acid Treatments. *Org. Electron.* **2017**, *45*, 182–189. https://doi.org/10.1016/j.orgel.2017.03.007.

(148) Holder, E.; Tessler, N.; Rogach, A. L. Hybrid Nanocomposite Materials with Organic and Inorganic Components for Opto-Electronic Devices. *J. Mater. Chem.* **2008**, *18* (10), 1064–1078. https://doi.org/10.1039/B712176H.

(149) Brenner, T. M.; Egger, D. A.; Kronik, L.; Hodes, G.; Cahen, D. Hybrid Organic—Inorganic Perovskites: Low-Cost Semiconductors with Intriguing Charge-Transport Properties. *Nat. Rev. Mater.* **2016**, *1* (1), 15007. https://doi.org/10.1038/natrevmats.2015.7.

(150) Russ, B.; Glaudell, A.; Urban, J. J.; Chabinyc, M. L.; Segalman, R. A. Organic Thermoelectric Materials for Energy Harvesting and Temperature Control. *Nat. Rev. Mater.* **2016**, *1* (10), 16050. https://doi.org/10.1038/natrevmats.2016.50.

(151) Badre, C.; Marquant, L.; Alsayed, A. M.; Hough, L. A. Highly Conductive Poly(3,4-Ethylenedioxythiophene):Poly (Styrenesulfonate) Films Using 1-Ethyl-3-Methylimidazolium Tetracyanoborate Ionic Liquid. *Adv. Funct. Mater.* **2012**, *22* (13), 2723–2727. https://doi.org/10.1002/adfm.201200225.

(152) Xia, Y.; Sun, K.; Ouyang, J. Solution-Processed Metallic Conducting Polymer Films as Transparent Electrode of Optoelectronic Devices. *Adv. Mater.* **2012**, *24* (18), 2436–2440. https://doi.org/10.1002/adma.201104795.

(153) Gueye, M. N.; Carella, A.; Massonnet, N.; Yvenou, E.; Brenet, S.; Faure-Vincent, J.; Pouget, S.; Rieutord, F.; Okuno, H.; Benayad, A.; et al. Structure and Dopant Engineering in PEDOT Thin Films: Practical Tools for a Dramatic Conductivity Enhancement. *Chem. Mater.* **2016**, *28* (10), 3462–3468. https://doi.org/10.1021/acs.chemmater.6b01035.

(154) Sahu, A.; Russ, B.; Su, N. C.; Forster, J. D.; Zhou, P.; Cho, E. S.; Ercius, P.; Coates, N. E.; Segalman, R. A.; Urban, J. J. Bottom-up Design of de Novo Thermoelectric Hybrid Materials Using Chalcogenide Resurfacing. *J. Mater. Chem. A* **2017**, *5* (7), 3346–3357. https://doi.org/10.1039/C6TA09781B.

(155) Yao, Q.; Chen, L.; Zhang, W.; Liufu, S.; Chen, X. Enhanced Thermoelectric Performance of Single-Walled Carbon Nanotubes/Polyaniline Hybrid Nanocomposites. *ACS Nano* **2010**, *4* (4), 2445–2451. https://doi.org/10.1021/nn1002562.

(156) Choi, J.; Lee, J. Y.; Lee, S. S.; Park, C. R.; Kim, H. High-Performance Thermoelectric Paper Based on Double Carrier-Filtering Processes at Nanowire Heterojunctions. *Adv. Energy Mater.* **2016**, *6* (9), 1502181. https://doi.org/10.1002/aenm.201502181.

(157) Zide, J. M. O.; Vashaee, D.; Bian, Z. X.; Zeng, G.; Bowers, J. E.; Shakouri, A.; Gossard, A. C. Demonstration of Electron Filtering to Increase the Seebeck Coefficient in In0.53Ga0.47As/In0.53Ga0.28Al0.19As Superlattices. *Phys. Rev. B* **2006**, *74*, 205335. https://doi.org/10.1103/PhysRevB.74.205335.

(158) Jarvis, S. P.; Taylor, S.; Baran, J. D.; Thompson, D.; Saywell, A.; Mangham, B.; Champness, N. R.; Larsson, J. A.; Moriarty, P. Physisorption Controls the Conformation and Density of States of an Adsorbed Porphyrin. *J. Phys. Chem. C* **2015**, *119* (50), 27982–27994. https://doi.org/10.1021/acs.jpcc.5b08350.

(159) Rusu, P. C.; Giovannetti, G.; Weijtens, C.; Coehoorn, R.; Brocks, G. First-Principles Study of the Dipole Layer Formation at Metal-Organic Interfaces. *Phys. Rev. B* **2010**, *81* (12), 125403. https://doi.org/10.1103/PhysRevB.81.125403.

(160) Crispin, X.; Geskin, V.; Crispin, A.; Cornil, J.; Lazzaroni, R.; Salaneck, W. R.; Brédas, J.-L. Characterization of the Interface Dipole at Organic/ Metal Interfaces. *J. Am. Chem. Soc.* **2002**, *124* (27), 8131–8141. https://doi.org/10.1021/ja025673r.

(161) Wang, Y.; Wang, H.; Xu, J.; He, B.; Li, W.; Wang, Q.; Yang, S.; Zou, B. PEDOT:PSS Modification by Blending Graphene Oxide to Improve the Efficiency of Organic Solar Cells. *Polym. Compos.* **2017**, *39* (9), 3066–3072. https://doi.org/10.1002/pc.24311.

(162) Zhou, C.; Dun, C.; Wang, Q.; Wang, K.; Shi, Z.; Carroll, D. L.; Liu, G.; Qiao, G. Nanowires as Building Blocks to Fabricate Flexible Thermoelectric Fabric: The Case of

Copper Telluride Nanowires. *ACS Appl. Mater. Interfaces* **2015**, *7* (38), 21015–21020. https://doi.org/10.1021/acsami.5b07144.

(163) Kim, B.; Shin, H.; Park, T.; Lim, H.; Kim, E. NIR-Sensitive Poly(3,4-Ethylenedioxyselenophene) Derivatives for Transparent Photo-Thermo-Electric Converters. *Adv. Mater.* **2013**, *25* (38), 5483–5489. https://doi.org/10.1002/adma.201301834.

(164) Glaudell, A. M.; Cochran, J. E.; Patel, S. N.; Chabinyc, M. L. Impact of the Doping Method on Conductivity and Thermopower in Semiconducting Polythiophenes. *Adv. Energy Mater.* **2015**, *5* (4), 1401072. https://doi.org/10.1002/aenm.201401072.

(165) Zhang, Q.; Sun, Y.; Xu, W.; Zhu, D. What To Expect from Conducting Polymers on the Playground of Thermoelectricity: Lessons Learned from Four High-Mobility Polymeric Semiconductors. *Macromolecules* **2014**, *47* (2), 609–615. https://doi.org/10.1021/ma4020406.

(166) Qu, S.; Yao, Q.; Wang, L.; Chen, Z.; Xu, K.; Zeng, H.; Shi, W.; Zhang, T.; Uher, C.; Chen, L. Highly Anisotropic P3HT Films with Enhanced Thermoelectric Performance via Organic Small Molecule Epitaxy. *NPG Asia Mater.* **2016**, *8* (7), e292. https://doi.org/10.1038/am.2016.97.

(167) Taek Hong, C.; Hun Kang, Y.; Ryu, J.; Yun Cho, S.; Jang, K.-S. Spray-Printed CNT/P3HT Organic Thermoelectric Films and Power Generators. *J. Mater. Chem. A* **2015**, *3* (43), 21428–21433. https://doi.org/10.1039/C5TA06096F.

(168) Dörling, B.; Ryan, J. D.; Craddock, J. D.; Sorrentino, A.; Basaty, A. E.; Gomez, A.; Garriga, M.; Pereiro, E.; Anthony, J. E.; Weisenberger, M. C.; et al. Photoinduced P- to n-Type Switching in Thermoelectric Polymer-Carbon Nanotube Composites. *Adv. Mater.* **2016**, *28* (14), 2782–2789. https://doi.org/10.1002/adma.201505521.

(169) Dörling, B.; Sandoval, S.; Kankla, P.; Fuertes, A.; Tobias, G.; Campoy-Quiles, M. Exploring Different Doping Mechanisms in Thermoelectric Polymer/Carbon Nanotube Composites. *Synth. Met.* **2017**, *225*, 70–75. https://doi.org/10.1016/j.synthmet.2017.01.002.

(170) He, M.; Ge, J.; Lin, Z.; Feng, X.; Wang, X.; Lu, H.; Yang, Y.; Qiu, F. Thermopower Enhancement in Conducting Polymer Nanocomposites via Carrier Energy Scattering at the Organic–Inorganic Semiconductor Interface. *Energy Environ. Sci.* **2012**, *5* (8), 8351. https://doi.org/10.1039/c2ee21803h.

(171) Geng, J.; Kong, B.-S.; Yang, S. B.; Youn, S. C.; Park, S.; Joo, T.; Jung, H.-T. Effect of SWNT Defects on the Electron Transfer Properties in P3HT/SWNT Hybrid Materials. *Adv. Funct. Mater.* **2008**, *18* (18), 2659–2665. https://doi.org/10.1002/adfm.200800496.

(172) Kline, R. J.; McGehee, M. D. Morphology and Charge Transport in Conjugated Polymers. *J. Macromol. Sci. Part C* **2006**, *46* (1), 27–45. https://doi.org/10.1080/15321790500471194.

(173) Sirringhaus, H.; Brown, P. J.; Friend, R. H.; Nielsen, M. M.; Bechgaard, K.; Langeveld-Voss, B. M. W.; Spiering, A. J. H.; Janssen, R. a. J.; Meijer, E. W.; Herwig, P.; et al. Two-Dimensional Charge Transport in Self-Organized, High-Mobility Conjugated Polymers. *Nature* **1999**, *401* (6754), 685. https://doi.org/10.1038/44359.

(174) Aasmundtveit, K. E.; Samuelsen, E. J.; Pettersson, L. A. A.; Inganäs, O.; Johansson, T.; Feidenhans'l, R. Structure of Thin Films of Poly(3,4-Ethylenedioxythiophene). *Synth. Met.* **1999**, *101* (1), 561–564. https://doi.org/10.1016/S0379-6779(98)00315-4.

(175) *Materials Studio 2017.1, DS BIOVIA. Dassault Systèmes BIOVIA, San Diego, CA.*

(176) Sun, H. COMPASS: An Ab Initio Force-Field Optimized for Condensed-Phase ApplicationsOverview with Details on Alkane and Benzene Compounds. *J. Phys. Chem. B* **1998**, *102* (38), 7338–7364. https://doi.org/10.1021/jp980939v.

(177) Asche, T. S.; Behrens, P.; Schneider, A. M. Validation of the COMPASS Force Field for Complex Inorganic–Organic Hybrid Polymers. *J. Sol-Gel Sci. Technol.* **2017**, *81* (1), 195–204. https://doi.org/10.1007/s10971-016-4185-y.

(178) Ran, N. A.; Roland, S.; Love, J. A.; Savikhin, V.; Takacs, C. J.; Fu, Y.-T.; Li, H.; Coropceanu, V.; Liu, X.; Brédas, J.-L.; et al. Impact of Interfacial Molecular Orientation on Radiative Recombination and Charge Generation Efficiency. *Nat. Commun.* **2017**, *8* (1), 79. https://doi.org/10.1038/s41467-017-00107-4.

(179) Leeuw, S. W. de; Perram, J. W.; Smith, E. R. Simulation of Electrostatic Systems in Periodic Boundary Conditions. I. Lattice Sums and Dielectric Constants. *Proc R Soc Lond A* **1980**, *373* (1752), 27–56. https://doi.org/10.1098/rspa.1980.0135.

(180) Gražulis, S.; Daškevič, A.; Merkys, A.; Chateigner, D.; Lutterotti, L.; Quirós, M.; Serebryanaya, N. R.; Moeck, P.; Downs, R. T.; Le Bail, A. Crystallography Open Database (COD): An Open-Access Collection of Crystal Structures and Platform for World-Wide Collaboration. *Nucleic Acids Res.* **2012**, *40* (D1), D420–D427. https://doi.org/10.1093/nar/gkr900.

(181) Park, H.; Son, W.; Hwan Lee, S.; Kim, S.; Joon Lee, J.; Cho, W.; Hee Choi, H.; Hyun Kim, J. Aqueous Chemical Synthesis of Tellurium Nanowires Using a Polymeric Template for Thermoelectric Materials. *CrystEngComm* **2015**, *17* (5), 1092–1097. https://doi.org/10.1039/C4CE02222J.

(182) Safdar, M.; Zhan, X.; Niu, M.; Mirza, M.; Zhao, Q.; Wang, Z.; Zhang, J.; Lianfeng Sun; He, J. Site-Specific Nucleation and Controlled Growth of a Vertical Tellurium Nanowire

Array for High Performance Field Emitters. *Nanotechnology* **2013**, *24* (18), 185705. https://doi.org/10.1088/0957-4484/24/18/185705.

(183) Li, Z.; Zheng, S.; Zhang, Y.; Teng, R.; Huang, T.; Chen, C.; Lu, G. Controlled Synthesis of Tellurium Nanowires and Nanotubes via a Facile, Efficient, and Relatively Green Solution Phase Method. *J. Mater. Chem. A* **2013**, *1* (47), 15046–15052. https://doi.org/10.1039/C3TA13035E.

(184) Villars, P.; Cenzual, K. Structure Types. Part 4: Space Groups (189) P-62m- (174) P-6. *Landolt Börnstein* **2006**, *43A4*. https://doi.org/10.1007/b11236.

(185) Yao, X.; Wang, J.; Wu, G.; S. Goh, S.; Zhu, H.; Yang, S.-W. Theoretical Study on the Self-Assembly of 1,3,5-Triethynylbenzene on Si(100)2 × 1 and in Situ Polymerization via Reaction with CO to Fabricate a Single Surface-Grafted Polymer. *J. Mater. Chem. C* **2017**, *5* (14), 3585–3591. https://doi.org/10.1039/C7TC00678K.

(186) Segall, M. D.; Lindan, P. J. D.; Probert, M. J.; Pickard, C. J.; Hasnip, P. J.; Clark, S. J.; Payne, M. C. First-Principles Simulation: Ideas, Illustrations and the CASTEP Code. *J. Phys. Condens. Matter* **2002**, *14* (11), 2717. https://doi.org/10.1088/0953-8984/14/11/301.

(187) Tkatchenko, A.; Scheffler, M. Accurate Molecular Van Der Waals Interactions from Ground-State Electron Density and Free-Atom Reference Data. *Phys. Rev. Lett.* **2009**, *102* (7), 073005. https://doi.org/10.1103/PhysRevLett.102.073005.

(188) Perdew, J. P.; Burke, K.; Ernzerhof, M. Generalized Gradient Approximation Made Simple. *Phys. Rev. Lett.* **1996**, *77* (18), 3865–3868. https://doi.org/10.1103/PhysRevLett.77.3865.

(189) Delley, B. From Molecules to Solids with the DMol3 Approach. *J. Chem. Phys.* **2000**, *113* (18), 7756–7764. https://doi.org/10.1063/1.1316015.

(190) Urban, J. J. Prospects for Thermoelectricity in Quantum Dot Hybrid Arrays. *Nat. Nanotechnol.* **2015**, *10* (12), 997–1001. https://doi.org/10.1038/nnano.2015.289.

(191) Varghese, T.; Hollar, C.; Richardson, J.; Kempf, N.; Han, C.; Gamarachchi, P.; Estrada, D.; Mehta, R. J.; Zhang, Y. High-Performance and Flexible Thermoelectric Films by Screen Printing Solution-Processed Nanoplate Crystals. *Sci. Rep.* **2016**, *6*, 33135. https://doi.org/10.1038/srep33135.

(192) Chesterfield, R. J.; McKeen, J. C.; Newman, C. R.; Ewbank, P. C.; da Silva Filho, D. A.; Brédas, J.-L.; Miller, L. L.; Mann, K. R.; Frisbie, C. D. Organic Thin Film Transistors Based on N-Alkyl Perylene Diimides: Charge Transport Kinetics as a Function of Gate Voltage and Temperature. *J. Phys. Chem. B* **2004**, *108* (50), 19281–19292. https://doi.org/10.1021/jp046246y.

(193) Imai, H.; Shimakawa, Y.; Kubo, Y. Large Thermoelectric Power Factor in TiS2 Crystal with Nearly Stoichiometric Composition. *Phys. Rev. B* **2001**, *64* (24), 241104. https://doi.org/10.1103/PhysRevB.64.241104.

(194) Vura-Weis, J.; Ratner, M. A.; Wasielewski, M. R. Geometry and Electronic Coupling in Perylenediimide Stacks: Mapping Structure−Charge Transport Relationships. *J. Am. Chem. Soc.* **2010**, *132* (6), 1738–1739. https://doi.org/10.1021/ja907761e.

(195) Zhang, G.; Kirk, B.; Jauregui, L. A.; Yang, H.; Xu, X.; Chen, Y. P.; Wu, Y. Rational Synthesis of Ultrathin N-Type Bi2Te3 Nanowires with Enhanced Thermoelectric Properties. *Nano Lett.* **2012**, *12* (1), 56–60. https://doi.org/10.1021/nl202935k.

(196) Reilly, T. H. I.; Hains, A. W.; Chen, H. Y.; Gregg, B. A. Self-Doping, O2-Stable, N-Type Interfacial Layer for Organic Electronics. *Adv. Energy Mater.* **2012**, *2* (4). https://doi.org/10.1002/aenm.201100446.

(197) Gregg, B. A.; Cormier, R. A. Liquid Crystal Perylene Diimide Films Characterized by Electrochemical, Spectroelectrochemical, and Conductivity versus Potential Measurements. *J. Phys. Chem. B* **1998**, *102* (49), 9952–9957. https://doi.org/10.1021/jp982842e.

(198) Burns, D. T.; Flockhart, B. D. Application of Quantitative EPR [and Discussion]. *Philos. Trans. Phys. Sci. Eng.* **1990**, *333* (1628), 37–48.

(199) Hochkirch, U.; Herrmann, W.; Stößer, R.; Moll, K.-P.; Llerena, J. G.; Linscheid, M.; Borchert, H.-H. Determination of Spin Concentrations in ESR Tomography as Applied for the Spatial Distribution of Spin Labels in Human Skin. *Appl. Magn. Reson.* **2008**, *35* (1), 173–184. https://doi.org/10.1007/s00723-008-0142-4.

(200) Yordanov, N. D. Is Our Knowledge about the Chemical and Physical Properties of DPPH Enough to Consider It as a Primary Standard for Quantitative EPR Spectrometry. *Appl. Magn. Reson.* **1996**, *10* (1–3), 339–350. https://doi.org/10.1007/BF03163117.

(201) Guillermet, O.; Mossoyan-Déneux, M.; Giorgi, M.; Glachant, A.; Mossoyan, J. C. Structural Study of Vapour Phase Deposited 3,4,9,10-Perylene Tetracarboxylicacid Diimide: Comparison between Single Crystal and Ultra Thin Films Grown on Pt(100). *Thin Solid Films* **2006**, *514* (1–2), 25–32. https://doi.org/10.1016/j.tsf.2006.02.024.

(202) Briseno, A. L.; Mannsfeld, S. C. B.; Reese, C.; Hancock, J. M.; Xiong, Y.; Jenekhe, S. A.; Bao, Z.; Xia, Y. Perylenediimide Nanowires and Their Use in Fabricating Field-Effect Transistors and Complementary Inverters. *Nano Lett.* **2007**, *7* (9), 2847–2853. https://doi.org/10.1021/nl071495u.

(203) Tatemichi, S.; Ichikawa, M.; Koyama, T.; Taniguchi, Y. High Mobility N-Type Thin-Film Transistors Based on N,N′-Ditridecyl Perylene Diimide with Thermal Treatments. *Appl. Phys. Lett.* **2006**, *89* (11), 112108. https://doi.org/10.1063/1.2349290.

(204) Klebe, G.; Graser, F.; Hädicke, E.; Berndt, J. Crystallochromy as a Solid-State Effect: Correlation of Molecular Conformation, Crystal Packing and Colour in Perylene-3,4:9,10-Bis(Dicarboximide) Pigments. *Acta Crystallogr. B* **1989**, *45* (1), 69–77. https://doi.org/10.1107/S0108768188010407.

(205) Iwamoto, N.; Yuen, M. M. F.; Fan, H. *Molecular Modeling and Multiscaling Issues for Electronic Material Applications*; Springer Science & Business Media, 2012.

(206) Zaia, E. W.; Gordon, M. P.; Niemann, V.; Choi, J.; Chatterjee, R.; Hsu, C.-H.; Yano, J.; Russ, B.; Sahu, A.; Urban, J. J. Molecular Level Insight into Enhanced N-Type Transport in Solution-Printed Hybrid Thermoelectrics. *Adv. Energy Mater.* **2019**, 1803469. https://doi.org/10.1002/aenm.201803469.

(207) Scheele, M.; Oeschler, N.; Meier, K.; Kornowski, A.; Klinke, C.; Weller, H. Synthesis and Thermoelectric Characterization of Bi2Te3 Nanoparticles. *Adv. Funct. Mater.* **2009**, *19* (21), 3476–3483. https://doi.org/10.1002/adfm.200901261.

(208) Kovalenko, M. V.; Scheele, M.; Talapin, D. V. Colloidal Nanocrystals with Molecular Metal Chalcogenide Surface Ligands. *Science* **2009**, *324* (5933), 1417–1420. https://doi.org/10.1126/science.1170524.

(209) Talapin, D. V.; Murray, C. B. PbSe Nanocrystal Solids for N- and p-Channel Thin Film Field-Effect Transistors. *Science* **2005**, *310* (5745), 86–89. https://doi.org/10.1126/science.1116703.

(210) Sahu, A.; Russ, B.; Su, N.; Forster, J.; Zhou, P.; Cho, E. S.; Ercius, P.; Coates, N. E.; Segalman, R. A.; Urban, J. J. Bottom-up Design of de Novo Thermoelectric Hybrid Materials Using Chalcogenide Resurfacing. *J. Mater. Chem. A* **2017**. https://doi.org/10.1039/C6TA09781B.